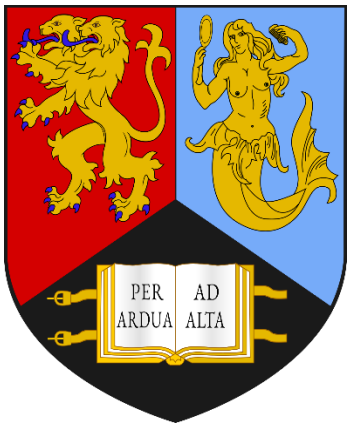


A Study of Precipitates in Mg-Sn Alloys

by

Yang Lyu

A thesis submitted to the University of Birmingham for the degree of

DOCTOR OF PHILOSOPHY

School of Metallurgy and Materials

College of Engineering and Physical Sciences

University of Birmingham

September 2021

UNIVERSITY OF
BIRMINGHAM

University of Birmingham Research Archive

e-theses repository

This unpublished thesis/dissertation is copyright of the author and/or third parties. The intellectual property rights of the author or third parties in respect of this work are as defined by The Copyright Designs and Patents Act 1988 or as modified by any successor legislation.

Any use made of information contained in this thesis/dissertation must be in accordance with that legislation and must be properly acknowledged. Further distribution or reproduction in any format is prohibited without the permission of the copyright holder.

Preface

This research was carried out by Yang Lyu in School of Metallurgy and Materials, University of Birmingham (from November 2016 to September 2021), under the supervision of Dr. Yu-Lung Chiu and Prof. Ian Jones.

The present work is original and no part of the work has been submitted for another degree at any other university. Wherever other researcher's work has been drawn or cited, it is acknowledged in the text and the references cited.

Acknowledgements

I am grateful to my supervisors, Dr. Yu-Lung Chiu and Prof. Ian Jones for their constant supervision, guidance, encourage and support. Dr. Yu-Lung Chiu has supported me with great patience and enlightening suggestions, which is greatly appreciated. A big thank you also goes to Prof. Ian Jones for his immense knowledge and inspiring passion towards science.

Many thanks to Mr. Paul Stanley and Mrs. Theresa Morris for their support over some of the equipment related in this project.

I would like to thank Dr. William Griffiths and Mr. Adrian Caden for their help on casting the material used in this project, and Mr. Jag Sangha for the work related with the workshop.

Many thanks to Dr. Rengen Ding and Dr. Feng Wang for the valuable discussions and guidance.

I would also like to thank my colleagues and friends for their nice company: Minshi Wang, Xinyu Lu, Jing Wu, Shanshan Si, Jinsen Tian, Yu Lu, Gareth Douglas, Daniel Higgins, Rayan Ameen, Subash Rai, Siben Jiang, Zhaoran Liu, Yukiko Ikebe, Wanqi Chen, Gnanavel Thirunavukkarasu, Bo Pang, Zhaoxuan Wu, Mark Elliot, Ubaid Ur Rehman Ghori, Uthman Mahmud, Alexandra Dickinson-Lomas, Peng Lin, Iulia Ipatova, Ludwig Schneider, Manmath Dash, and Qi Wei.

My appreciation also goes to the financial support from the School of Metallurgy and Materials and China Scholarship Council (CSC).

To whoever supported me during my PhD study.

Abstract

The precipitates in Mg-6Sn, Mg-6Sn-3Al and Mg-6Sn-3Zn (wt.%) alloys has been studied to determine the effect of different precipitate species on basal slip. The precipitates in peak-aged alloys were qualitatively and quantitatively analysed using electron microscopy for their chemistry, morphology, and crystallography. Two types of Mg_2Sn precipitates were identified in the Mg-6Sn binary alloy, four types of Mg_2Sn precipitates in the Mg-6Sn-3Al alloy and two types of Mg_2Sn and two types of $MgZn_2$ precipitates in the Mg-6Sn-3Zn alloy.

Pillar compression on specimens orientated for basal slip has been performed on the three Mg-Sn alloys to analyse the effect of different precipitate types on the deformation behaviour. The Mg-6Sn alloy exhibits the lowest resistance towards basal slip, Mg-6Sn-3Al the next highest and Mg-6Sn-3Zn exhibits the most strengthening as well as work hardening. TEM observation of as-compressed pillars indicate that basal slip was activated and was the only activated slip system.

The exact strengthening contributions of different precipitate types have been analysed quantitatively using the Orowan strengthening model. An approach to quantifying the strengthening effects of a multiple precipitate system has been proposed and applied. The as-estimated strengthening contributions from Orowan strengthening, solid solution strengthening and precipitate shearing strengthening have been analysed. The results agree adequately with the experimentally measured strength.

Keywords: Mg-Sn alloys, precipitation, deformation behaviour, multiple precipitate type, Orowan strengthening

Contents

1 Introduction 1
2 Literature review 3
2.1 Magnesium 3
2.1.1 History 3
2.1.2 Atomic properties 3
2.1.3 Lattice parameters 4
2.1.4 Mechanical properties 4
2.2 Deformation behaviour of pure magnesium 5
2.2.1 Slip 7
2.2.2 Twinning 8
2.3 Magnesium alloys 9
2.3.1 The Mg-Al alloy system 11
2.3.2 The Mg-RE alloy systems 14
2.3.3 The Mg-Sn alloy system 16
2.4 Strengthening mechanisms in the Mg-Sn alloys 17
2.4.1 Grain size strengthening 17
2.4.2 Solid solution strengthening 17
2.4.3 Orowan strengthening 18
2.5 Microstructure evolution of Mg-Sn alloys during heat treatment 20
2.6 Precipitation in the Mg-Sn alloys 25
2.7 Mg-Sn alloys strengthened by various types of precipitates 31
3 Aim and objectives 34
4 Experimental methodology 35
4.1 Raw materials 35
4.2 Sand casting 35
4.3 Heat treatment 36
4.4 Microstructure characterization 36
4.4.1 Optical microscopy (OM) 36
4.4.2 Scanning electron microscopy (SEM) 37
4.4.3 X-ray diffraction analysis (XRD) 39
4.4.4 Transmission electron microscopy (TEM) 39
4.5 Hardness 41
5 Characterization of precipitates in Mg-Sn alloys 42
5.1 Introduction 42
5.2 Characterisation of the as-cast alloys 42
5.2.1 Optical microscopy 43
5.2.2 SEM 44
5.3 Age hardening response of the as-aged Mg-6Sn alloys 46

5.4 Studying the precipitates in Mg-Sn alloys 47
5.4.1 Morphology and crystallography of precipitates in Mg-6Sn 52
5.4.2 Morphology and crystallography of precipitates in Mg-6Sn-3Al ternary alloy 56
5.4.3 Morphology and crystallography of precipitates in Mg-6Sn-3Zn ternary alloy 69
5.5 Summary 81
6 Analysis of basal slip using micro-pillar compression 83
6.1 Introduction 83
6.2 The calculation of Schmid factors in determining the loading direction .. 83
6.3 Basal slip behaviour of the peak aged Mg-6Sn binary alloy 87
6.3.1 Micro-pillar compression of the peak aged Mg-6Sn binary alloy . 87
6.3.2 Dislocation analysis of the Mg-6Sn pillars compressed along $[01\bar{1}1]_{Mg}$ 90
6.4 Basal slip behaviour of the peak aged Mg-6Sn-3Al ternary alloy 93
6.4.1 Micro-pillar compression of the peak aged Mg-6Sn-Al ternary alloy 93
6.4.2 Dislocation analysis for the Mg-6Sn-3Al pillars compressed along $[\bar{1}8\bar{7}\bar{9}]_{Mg}$ 97
6.5 Basal slip behaviour of the peak aged Mg-6Sn-3Zn alloy 100
6.5.1 Micro-pillar compression of the peak aged Mg-6Sn-3Zn alloy ... 100
6.5.2 Dislocation analysis of the Mg-6Sn-3Zn pillars compressed along $[25\bar{7}6]_{Mg}$ 104
6.6 Summary 108
7 Orowan strengthening in Mg-Sn alloys 109
7.1 Introduction 109
7.2 Derivation of suitable parameters for Orowan strengthening 109
7.2.1 Orowan equations for different precipitate types 109
7.2.2 Fitting precipitate dimensions to Orowan equations 113
7.2.3 Determination of volume fraction 126
7.2.4 Calculation of Orowan strengthening 128
7.2.5 Total strengthening effect in Mg-Sn alloys 132
7.3 Summary 136
8 Discussion 138
8.1 List of results 138
8.2 Precipitation in Mg-Sn alloys 139
8.3 Precipitate shearing in Mg-6Sn-3Zn alloys 141
8.4 Explaining the work-hardening in the Mg-6Sn-3Zn alloy 148
8.5 Promoting non-basal precipitates in Mg-Sn alloys 151
9 Conclusions and Future work 153
9.1 Conclusions 153
9.2 Suggestions for future work 154
10 References 156

1 Introduction

The U.S Energy Information Administration states that the world crude oil price has kept rising over the past 20 years [1]. Therefore, it is of vital importance for the transport industry to find alternative materials to reduce fuel consumption as well as environmental impact. Previous research has discovered that a decrease of 100kg in the net weight of a vehicle will lead to a reduction of 0.5L/km fuel consumption and 200kg of CO_2 emission in its mean life [2]. Due to its light weight and outstanding alloying capability, magnesium and its alloys have found application in a number of areas such as aerospace and automotive.

As the mechanical properties of pure magnesium are not adequate, mainly due to inadequate strengthening mechanisms, it must be alloyed with other elements. Common magnesium alloy systems include the AZ series (Mg-Al-Zn), AM series (Mg-Al-Mn), AE series (Mg-Al-RE) and the ZK series (Mg-Zn-Zr), etc. [3]. The most widely used Mg alloy system is the AZ system, which has relatively poor mechanical properties at elevated temperature [4]. As an alternative approach, the Mg-Sn alloy system has attracted great attention due to its outstanding mechanical properties at elevated temperature as well as relatively low price, making it a potential material for high-temperature application as an alternative to Mg-RE alloys.

The precipitation hardening response of the Mg-Sn alloy system lies in the formation of

a Mg_2Sn phase with a melting point of 778℃, providing satisfactory creep resistance. However, this phase forms on different planes with different morphologies, and only those which are not on basal planes can block (the dominating) basal slip effectively [5]. It is suggested that different heat treatment parameters and micro-alloying elements affect the habit planes of the precipitates [6]–[8]. Currently, existing research has only demonstrated an improvement on hardness only, caused by non-basal precipitates. The exact effect on the slip behaviour of Mg-Sn alloys has barely been studied.

This project focuses on the morphology and orientation relationships of the Mg_2Sn precipitates in a Mg-6Sn (wt.%) alloy system and the effect of precipitates on slip behaviour.

2 Literature review

2.1 Magnesium

2.1.1 History

Magnesium was first identified as an element in 1755 by Joseph Black. Isolation of pure Mg was accomplished by Sir Humphry Davy in 1808 when he electrolysed a mixture of magnesia (MgO) and mercuric oxide (HgO). Magnesium was first used in flashlights and for other pyrotechnical purposes. Industrial production of magnesium declined with the end of World War II during which it was investigated by the aircraft industry as an alternative to aluminium but failed [9].

The magnesium industry has experienced a renaissance in recent years as an attempt to decrease fuel consumption and environmental impact, especially in the automotive and aerospace industries. With an improvement in mechanical properties, anti-corrosion properties and high-temperature creep resistance, magnesium has again become a potential viable light material.

2.1.2 Atomic properties

Magnesium is the twelfth element in the periodic table. It is the sixth most abundant element in the earth crust at 2.7%. Magnesium has 3 isotopes, respectively 24, 25 and 26 which exist naturally in the ratios 7:1:1. Therefore, the molar mass of magnesium is 24.33. Its

twelve electrons occupy the orbits of a free atom as $1s^2 2s^2 2p^6 3s^2$. The two x-ray emission lines of magnesium, K_α and K_β, are respectively at 9.889Å and 9.558Å. [10]

2.1.3 Lattice parameters

The freezing point for liquid magnesium is 650℃. The solid has a hexagonal close packed structure, increasing its density over that of the liquid by approximately 4%. The lattice constants at room temperature and ambient pressure are a=320.94pm and c=521.08pm with c/a at 1.624, which is close to the theoretical value for close packing of 1.633. Hence, magnesium can be considered as perfectly close packed [10]. The crystal structure and principal planes of magnesium are shown below in Figure 1.

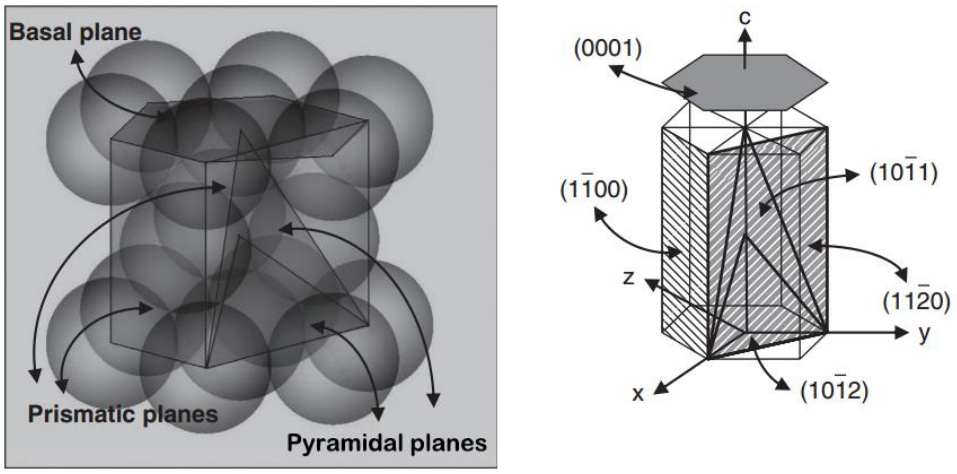


Figure 1 Crystal structure of Mg[11]

2.1.4 Mechanical properties

The mechanical properties of pure magnesium are listed below in Table 1[12]. As shown in the table, the mechanical properties of pure magnesium are far from satisfactory. Major

alloying elements include aluminium, zinc, tin, silicon, calcium and rare earth elements[12].

Table 1 Mechanical properties of pure Mg[12]

Pure Magnesium	**Annealed Sheet**	**Hand-rolled Sheet**	**Sand Cast**	**Extruded**
0.2% Compressive yield strength (MPa)	69-83	105-115	21	34-55
0.2% Tensile yield strength (MPa)	90-105	115-140	21	69-105
Ultimate tensile strength (MPa)	160-195	180-220	90	165-205
Hardness (HB)	40-41	45-47	30	35

2.2 Deformation behaviour of pure magnesium

Von Mises stated that at least 5 independent slip systems must be activated for polycrystalline materials to deform uniformly without causing grain boundary failure [13]. The available basal slip systems for magnesium are fewer than the minimum requirements for uniform deformation, as listed below in Table 2 [14]. Therefore, non-basal slip systems or twinning must be activated for deformation in magnesium alloys. The slip along the basal a directions only gives a a-axis slip component and doesn't accommodate any strain along the c-axis. Therefore, a c-axis slip component is very important for the uniform deformation of HCP polycrystalline materials. Second order pyramidal slip with a slip direction of $\langle 11\bar{2}3\rangle_{Mg}$

will provide five independent deformation modes[15]. Therefore, any materials exhibiting pyramidal c + a slip will fulfil the von Mises criterion for general homogeneous plastic deformation regardless of the other slip systems present. Kang *et al.* [16] studied the activation of the c + a slip system in magnesium and suggested that the dominant slip system of magnesium at temperatures below 100℃ is basal slip. The fraction of c + a slip began to increase at temperatures above 100℃ and keeps increasing as the temperature rises, as shown in Figure 2 where *h* is the fraction of slip systems and ρ the density of dislocations. At room temperature, the CRSS value of second order pyramidal slip is normally ~100 times higher than that of basal slip. However, this value h decreases with increasing temperature. When the temperature exceeds 200℃, second order prismatic slip is favoured over twinning.

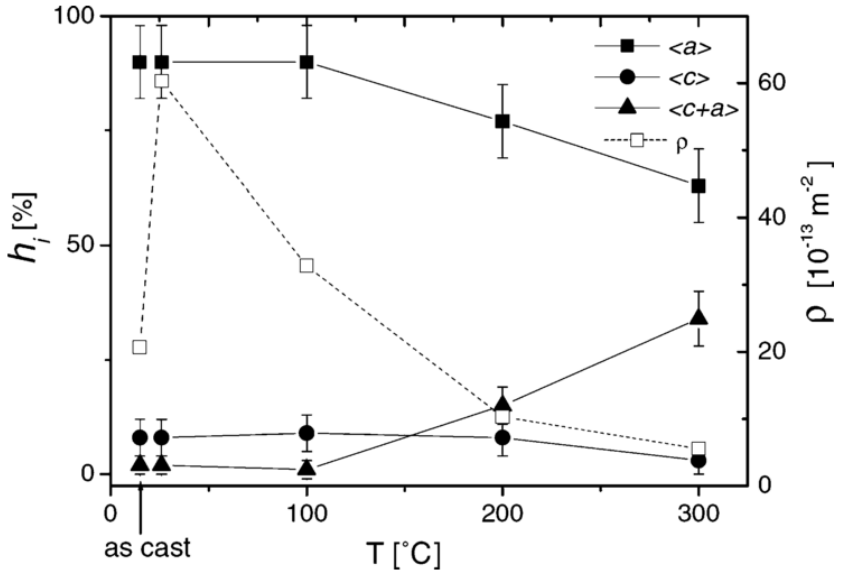


Figure 2 Competition between slip systems in Mg at different temperatures [16]

Table 2 Slip systems in magnesium[14]

Direction	**Plane**	**Crystallographic Elements**	**Number of Independent Modes**

a	Basal slip	$(0002) < 11\bar{2}0 >$	2
	Prismatic slip	$\{1\bar{1}00\} < 11\bar{2}0 >$	2
	Pyramidal slip	$\{1\bar{1}01\} < 11\bar{2}0 >$	4
c		$\{h\bar{k}i0\}[0001]$	No slip
c+a	Pyramidal slip	$\{h\bar{k}i/\} < 11\bar{2}\bar{3} >$	5

2.2.1 Slip

Slip in crystals can be defined as the irreversible shear of one part of the crystal relative to another under a shear stress without changing the orientation of the crystal (twinning) or breaking a large number of atomic bonds (cracking) [10].

The energy of a dislocation is determined by the shear modulus G and the magnitude of Burgers vector b:

$$E_{dis} \approx G \cdot b^2 \qquad \text{Equation 2-1}$$

The easiest slip system to activate will always have the smallest Burgers vector. In an ideal HCP crystal with the c/a of 1.633, the shortest slip vector preserving the ABAB close packed plane is $\frac{a}{3}\langle 11\bar{2}0\rangle$. The strain energy associated with this Burgers vector can be decreased by the dissociation of the basal dislocations into two separate partial dislocations with slip vectors of $\frac{a}{3}\langle 10\bar{1}0\rangle$ connected by a stacking fault, whose energy γ varies with the material [10].

In the HCP metals and their alloys, first order prismatic slip ($\frac{a}{3}\langle 11\bar{2}0\rangle\{10\bar{1}0\}$) and first order pyramidal slip ($\frac{a}{3}\langle 11\bar{2}0\rangle\{10\bar{1}1\}$) are the most important types of slip aside from basal

slip ($\frac{a}{3}\langle 11\bar{2}0\rangle\{0001\}$). In addition, the activation of the c + a slip systems, via first order pyramidal slip ($\frac{1}{3}\langle 11\bar{2}3\rangle\{10\bar{1}1\}$) or second order pyramidal slip ($\frac{1}{3}\langle 11\bar{2}3\rangle\{10\bar{2}2\}$), can also promote the plasticity of the magnesium alloys.

The term critical resolved shear stress (CRSS) indicates the ease of slip system activation in a certain crystal. For a magnesium single crystal, the CRSSs of each slip system are summarised below.

Table 3 CRSS values of different slip systems in Mg with reference

Slip type	**Slip plane**	**Slip direction**	**CRSS (MPa)**	**Ref.**
< a >	Basal {0001}	$\langle 11\bar{2}0\rangle$	2	[17]
< a >	Prismatic $\{1\bar{1}00\}$	$\langle 11\bar{2}0\rangle$	45	[18]
< c + a >	2nd order pyramidal $\{11\bar{2}2\}$	$\langle 11\bar{2}3\rangle$	50	[19]

2.2.2 Twinning

Twinning is also an important means of deformation in magnesium and its alloys as the number of slip systems in magnesium is limited. The most common twinning system in magnesium is the $\{10\bar{1}2\}$ twins known as “tension” twins, as suggested by Barnett [20]. This twinning system only operates when the deformation provides an extension along the c-axis. The other common twinning system is a $\{10\bar{1}1\} - \{10\bar{1}2\}$ double twinning system, also known as “contraction” twins, which is basically the formation of secondary twins in the primary twinning areas [21].

2.3 Magnesium alloys

According to the American Society of Testing and Materials (ASTM), classification of magnesium alloys is performed according to the following method: the alloy designation system consists of two letters indicating the two major alloying elements, two numbers indicating the wt.% of alloying element and one letter indicating a certain alloy type in the above mentioned composition [3] (Table 4). Take AZ91-T6 as an example: the letters A and Z represent the two major elements in the alloy, aluminium and zinc, and their respective contents at 9wt.% and 1wt.%. T6 indicates that the alloy has been solution treated and aged. Abbreviations for the elements are listed in the table below. Heat treatment methods can also be included by adding symbols at the end of the alloy designation.

Table 4 ASTM abbreviations for magnesium alloys[3]

Alloying element	**Abbreviation letter**
Aluminium	A
Bismuth	B
Copper	C
Cadmium	D
Rare earth metals	E
Iron	F
Thorium	H
Strontium	J
Zirconium	K

Lithium	L
Manganese	M
Nickel	N
Lead	P
Silver	Q
Chromium	R
Silicon	S
Tin	T
Yttrium	W
Antimony	Y
Zinc	Z

Magnesium alloys can also be divided into cast and wrought alloys in terms of manufacturing method. Wrought alloys are normally cast into ingots or bars and then mechanically worked into the desired shape (by extrusion, forging or rolling) while cast alloys are directly cast into certain moulds. Common cast alloys include M1A, AZ91D, AM60D, AS41A, etc., while common wrought alloys include M1A, AZ31B, AZ80A, ZK60A, TA54A etc. Most of the Mg alloys are heat treatable while M1A is a notable exception.

The difference in properties between cast and wrought magnesium alloys lies in the texture given in the wrought process. Additional textures in the alloy (especially the texture parallel to the main rolling direction) will lead to additional precipitate nucleation and therefore excellent strength. In addition, the working process also has the capability of decreasing porosity [22].

2.3.1 The Mg-Al alloy system

Currently, the Mg-Al alloy system is the most widely applied Mg alloy system in industry. The Mg-Al system is normally micro-alloyed with a small portion of Zn, which promotes the precipitate yields in the AZ series alloys. Common AZ series alloys include AZ91, AZ80, AZ61 and AZ31. The effect of Zn in the AZ series alloys is to lower the solubility of Al in Mg and produces a higher driving force for precipitate nucleation[23]. The AZ series alloys are precipitation strengthened by a continuous $Mg_{17}Al_{12}$ β-phase after artificial ageing. This phase has a complex BCC structure (space group $I\bar{4}3m$, a=1.056nm), with 34 Mg atoms and 24 Al atoms. Apart from the Mg matrix and the β-phase precipitates, additional phases will not appear when the ratio of Mg to Zn is lower than 3:1[24]. Due to the similar atom sizes and electro-negativity of Al and Zn (125pm and 135pm, 1.61 and 1.65), Zn normally forms a ternary $Mg_{17}(Al, Zn)_{12}$ phase together with Mg and Al.

During equilibrium cooling of AZ series alloys, both continuous precipitation (CP) and discontinuous precipitation (DP) will occur [25]. Figure 3 shows a TEM image with both CP and DP present. Although they result in the same $Mg_{17}Al_{12}$ phase, the precipitates vary in size and morphology. Generally, continuous precipitation takes place within grains, preferably at pre-existing defects like dislocations and vacancies. Previous research has reported that the continuous precipitates can be either lath-shaped or rod-shaped[25], [26]. The dominating lath-shaped precipitates tends to grow on the $(0001)_{Mg}$ plane following the OR $(0001)_{Mg} \parallel (110)_{Mg17Al12}, [11\bar{2}0]_{Mg} \parallel [1\bar{1}1]_{Mg17Al12}$, which is the Burgers OR[26]. Given the three-

fold substitution of $[11\bar{2}0]_{Mg}$, $[1\bar{2}10]_{Mg}$, $[\bar{2}110]_{Mg}$ and the two-fold substitution of $[1\bar{1}1]_{Mg17Al12}$ and $[1\bar{1}\bar{1}]_{Mg17Al12}$, the Burgers OR will have six variants, as reported by Celotto [26]. The rod-shaped precipitates, which are less dominant, tend to grow along the $[0001]_{Mg}$ direction, or deviated by a certain angle. The precipitates growing along the $[0001]_{Mg}$ direction follow the OR $(1\bar{1}00)_{Mg} \parallel (1\bar{1}1)_{Mg17Al12}, [0001]_{Mg} \parallel [111]_{Mg17Al12}$, which is the Crawley OR [27]. Some other ORs have also been reported. The ORs in the Mg-Al alloy system are summarized in Table 5.

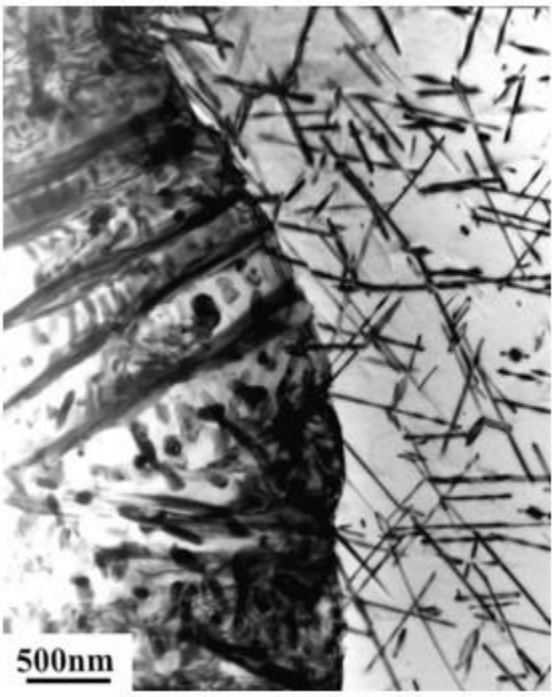


Figure 3 TEM image showing continuous precipitates (on the right) and discontinuous precipitates (on the left) in an as-aged AZ91 alloy[3]

Table 5 Reported ORs between $Mg_{17}Al_{12}$ precipitates and the matrix in the Mg-Al alloy system

Name	**OR**	**Morphology**	**Reference**
Burgers	$(0001)_{Mg} \parallel (110)_{Mg17Al12}, [11\bar{2}0]_{Mg} \parallel [1\bar{1}1]_{Mg17Al12}$	Basal laths	[26]
Potter	$(\bar{1}\bar{1}21)_{Mg} \parallel (011)_{Mg17Al12}, [1\bar{1}00]_{Mg} \parallel [0\bar{1}1]_{Mg17Al12}$	Basal rods	[28]
Crawley	$(1\bar{1}00)_{Mg} \parallel (1\bar{1}1)_{Mg17Al12}, [0001]_{Mg} \parallel [111]_{Mg17Al12}$	C-axis rods	[27]
Gjønnes-Østmoe	$(0001)_{Mg} \parallel (011)_{Mg17Al12}, [11\bar{2}0]_{Mg} \parallel [2\bar{1}1]_{Mg17Al12}$	Basal laths	[29]
Potter	$(0001)_{Mg}$~2°$(011)_{Mg17Al12}, (01\bar{1}1)_{Mg} \parallel (110)_{Mg17Al12}, [11\bar{2}0]_{Mg} \parallel [1\bar{1}1]_{Mg17Al12}$	Basal rods	[30]

Discontinuous precipitation, on the other hand, takes place preferentially on the grain boundaries. The growth of discontinuous precipitation is generally the growth of $Mg_{17}Al_{12}$ precipitates formed on high angle grain boundaries, as the diffusion on the grain boundary is much faster than that in the matrix [31]. When the grain boundary migrates, the $Mg_{17}Al_{12}$ also grows, trailing the moving boundary, which is also called a reaction front. All the discontinuous precipitates follow the Burgers OR $(0001)_{Mg} \parallel (110)_{Mg17Al12}, [11\bar{2}0]_{Mg} \parallel [1\bar{1}1]_{Mg17Al12}$ which probably corresponds to an interfacial energy minimum [30]. Normally, discontinuous precipitation takes place during low temperature ageing, or slow cooling after casting.

The competition of continuous and discontinuous precipitation depends on the content of Al in the alloy, ageing temperature and micro-alloying elements. Hutchinson *et al.* suggested a relationship between alloy composition, ageing temperature and precipitate distribution, as shown in Figure 4:

For AZ91, the respective temperature ranges for different precipitate distributions are:

When 100℃<T<T_{d1}, both CP and DP will occur. Volume fraction occupied by DP will increase with T;

When T_{d1}<T<T_{d2}, only DP will occur;

When T_{d2}<T<T_{c2}, both CP and DP will again be observed;

When T_{c2}<T<T_s (solvus temperature), only CP will occur [32].

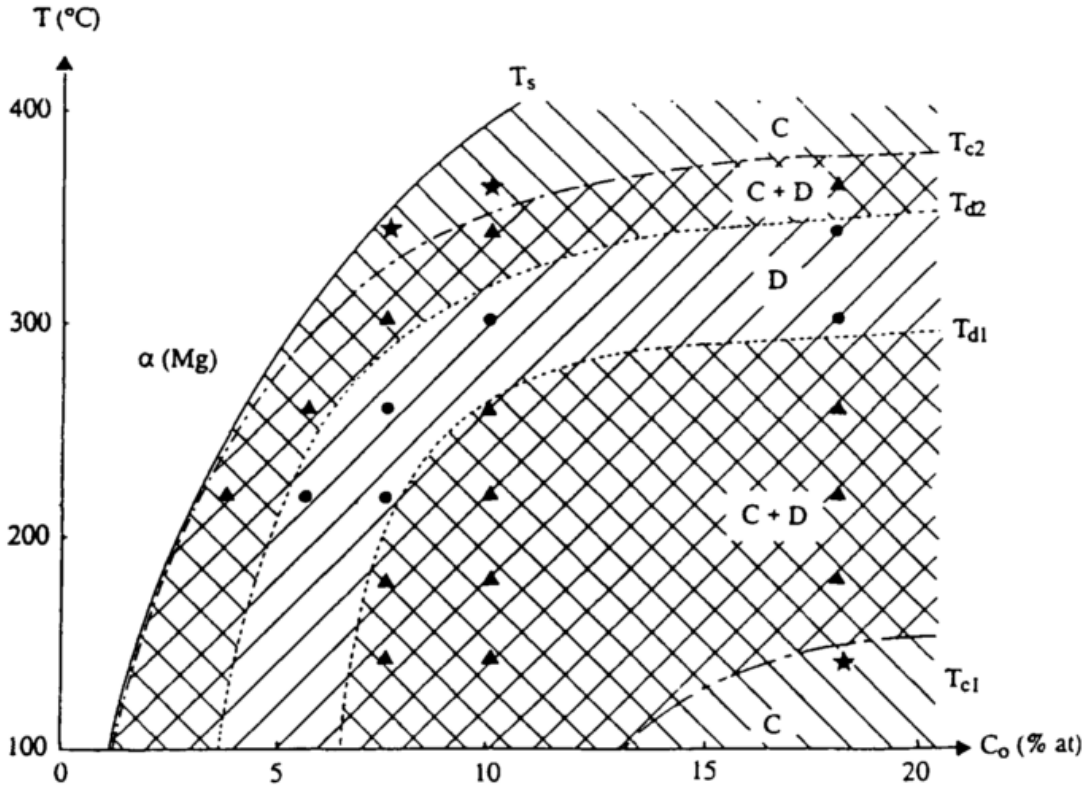


Figure 4 Diagram showing the competition between continuous and discontinuous precipitation in Mg-Al alloys as a function of alloy composition and ageing temperature[32]

2.3.2 The Mg-RE alloy systems

As applications in a powertrain system, transmission housing and crankcases require high performance at elevated temperature (normally >150℃), a stable microstructure is of

vital importance. Common magnesium alloys such as the AZ series will no longer be adequate as the thermal instability of the microstructure leads to poor creep resistance as well as a decrease in strength. Therefore, alloys strengthened by precipitation strengthening with a thermally stable precipitate distribution are considered to be necessary for these applications [33]. Enhanced creep resistance has been found with some Mg alloys with rare earth elements such as Mg-8Al-xRE[34], WE43[33], Mg-3.3Gd-4.3Y[35], Mg-18Gd[36]. A list of Mg alloys containing RE elements and their relevant creep properties appears in Table 6 below.

Table 6 Creep properties of Mg alloys containing RE elements

Alloy (wt.%)	**Temperature**	**Applied stress**	**Creep rate**	**Reference**
AZ91(Ref)	200℃	50MPa	$1.56*10^{-7}$/s	[37]
WE43 (Mg–4.38Y–2.72Nd–1.10Gd–0.56Zr)	250℃	75MPa	$2.7*10^{-9}$/s	[33]
Mg-8Al-1RE (La, Ce, Pr, Nd)	200℃	40MPa	$1.43*10^{-6}$/s	[34]
Mg-8Al-3RE (La, Ce, Pr, Nd)	200℃	40MPa	$6.77*10^{-7}$/s	[34]
Mg-4Al-5Y-2.5 (La, Ce, Pr)	200℃	117.1MPa	$7.90*10^{-10}$/s	[38]
Mg-3.3Gd-4.3Y	300℃	100MPa	$2.50*10^{-6}$/s	[35]
Mg-18Gd	250℃	120MPa	$1.18*10^{-7}$/s	[36]
Mg-18Gd	250℃	180MPa	$6.92*10^{-7}$/s	[36]

2.3.3 The Mg-Sn alloy system

The Mg-Sn alloy system has the potential for elevated temperature applications. It is age-hardened and strengthened by an Mg_2Sn second phase. The solubility of Sn in Mg is as high as 3.35 at. % (equivalent to 14.48 wt.%) at 561℃ and 0.035 at.% (0.17 wt.%) at room temperature [10]. Therefore, a considerable number of precipitates is expected in Mg-Sn alloys. Mg_2Sn has a CaF_2 structure (space group $Fm\bar{3}m$) with a lattice constant of a = 6.759Å. The volume of the unit cell is 308.84$Å^3$ [39]. The melting point of Mg_2Sn is 770℃, which leads to satisfactory mechanical properties at elevated temperature. The crystal structure of Mg_2Sn is shown below in Figure 5.

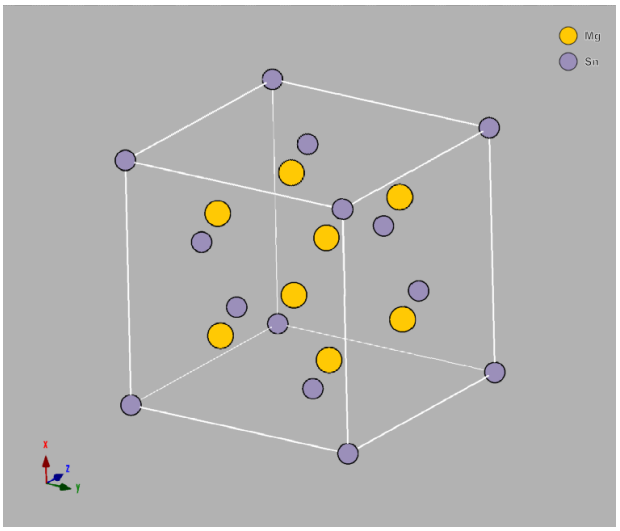


Figure 5 Fluorite crystal structure of the Mg_2Sn phase viewed in CrystalMaker

The Mg-Sn alloy system is promising for elevated temperature applications, as an alternative to the Mg-RE series. The advantage of the creep behaviour of the Mg-Sn alloys over the AZ series can be found by comparing a Mg-8Sn (wt.%) alloy with AZ91. At 150℃ under a stress of 150MPa, the creep rate of the Mg-8Sn alloy is $1.35*10^{-9}$/s [40], compared

with $2.41*10^{-7}$/s for AZ91 [37], 178 times lower. In certain applications such as automotive crankcases and transmission housing casings, the Mg-Sn alloy system may replace the Mg-RE system due to its relatively low cost.

Currently, the Mg-Sn alloy system has not been widely applied in industry. As the age hardening response, deformation behaviour and fabrication are still not yet fully developed, intense research is needed to promote the industrial application of the Mg-Sn alloy system.

2.4 Strengthening mechanisms in the Mg alloys

2.4.1 Grain size strengthening

The effect of grain size on mechanical properties can be described by the well-known Hall-Petch relation, which dictates that the strength of a metal (σ_s) equals the frictional stress (σ_0) plus a factor (k) times the inverse square root of the grain size (D):

$$\sigma_s = \sigma_0 + \frac{k}{\sqrt{D}} \qquad \text{Equation 2-2}$$

Cáceres *et al.* suggested that the σ_0 of pure magnesium was 11MPa and that k was $0.22\text{MPam}^{1/2}$ for pure magnesium [41]. However, specific parameters for the Mg-Sn system have not yet been determined.

2.4.2 Solid solution strengthening

As studied by Shi *et al.* [42], solid solution behaviour in the Mg-Sn alloys is similar to that in the AZ series alloys suggested by Cáceres and Rovera [43]. Therefore, the contribution

of solid solution strengthening can be described by:

$$\sigma_{sss} = \mathrm{m}B_n c^n \qquad \text{Equation 2-3}$$

where: m is the Taylor factor connecting the tensile flow stress of the polycrystals to the CRSS of the relevant slip systems, normally being set at ~5.5 for magnesium alloys. B_n is the solid solution strengthening rate depending on the alloy system and c the Sn atomic concentration, n being ½ or 2/3. $\mathrm{m}B_n c^n$ is sometimes written in the form of CX^n, where C is the solid solution strengthening rate while X is the atomic concentration of solute [43].

2.4.3 Orowan strengthening

As suggested by Orowan in 1947 [44], the interaction between dislocations and precipitates is determined by a critical precipitate size. Dislocations can shear through particles smaller than this size and will bend around particles larger than this size. The transition and competition between precipitate shearing and Orowan looping has already been described in textbooks and is shown in Figure 6.

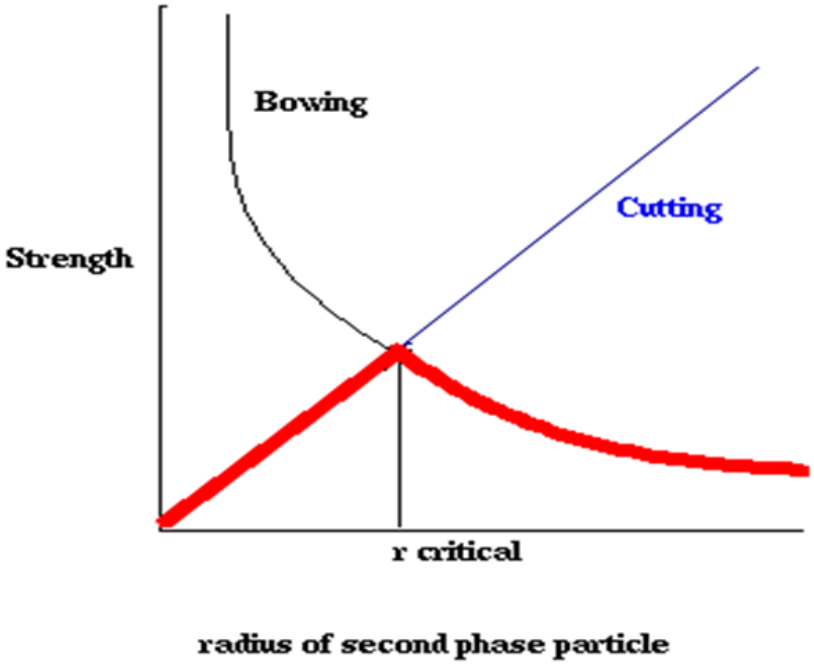


Figure 6 The transition and competition between precipitate shearing and Orowan looping with respect to the critical particle size[45]

However, there are no theoretical or experimental results indicating the critical size in Mg-Sn alloys. Hutchinson *et al.* [32] estimated the critical size in AZ91 alloys as ~3nm using the following equation:

$$\frac{G_m b}{R} = \frac{G_p}{15} \qquad \text{Equation 2-4}$$

where G_m is the shear modulus of Mg, G_p the shear modulus of the precipitate, b the Burgers vector and R the radius of the dislocation curvature around the precipitate. Dislocations in Mg alloys will tend to bow around the precipitate particles and form "Orowan loops". The increase of Orowan stress of a spherical particle can be described as:

$$\sigma_{Orowan} = \frac{MGb}{2\pi\sqrt{1-\nu}} \frac{1}{\lambda} \ln\left(\frac{d_p}{r_0}\right) \qquad \text{Equation 2-5}$$

where M is the Taylor factor, G the shear modulus of Mg, b the Burgers vector of the dislocation, ν Poisson's ratio, λ and d_p are respectively the mean spacing and diameter of the particles in the slip plane and r_0 is the cut-off radius of the dislocation core and is taken equal to b [46].

However, this model will have difficulties in being applied to the Mg-Sn alloy system. For the Mg-Al system, the precipitates normally exist as basal precipitates with the Burgers OR thus there's only one type of precipitate. In the Mg-Sn alloy system, as described later, several precipitate morphologies will exist, including basal laths, pyramidal laths, c-axis rods, etc. In this case, one mean particle spacing and particle diameter are not adequate for an accurate estimation of the Orowan strengthening effect. In addition, the interaction with different precipitate types needs to be considered as well. This will be explained in a later section.

2.5 Microstructure evolution of Mg-Sn alloys during heat treatment

As indicated in the Mg-Sn phase diagram [47], Sn is fully soluble in molten Mg. The molten alloy will first form the α-Mg matrix, which grows dendritically during solidification. A divorced eutectic reaction will then take place (e.g., ~563°C for Mg-14wt.% Sn), forming eutectic α-Mg and Mg_2Sn due to non-equilibrium cooling[4]. A typical microstructure of an as-cast Mg-Sn alloy is shown below in Figure 7.

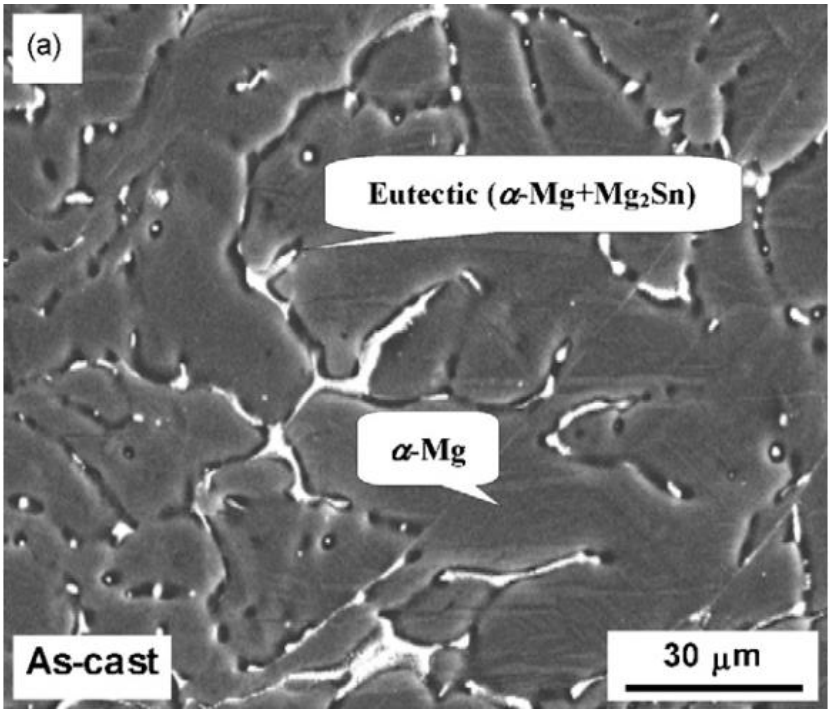


Figure 7 A typical as-cast structure of binary Mg-Sn [4]

In order to improve the mechanical properties, Mg-Sn alloys are commonly subjected to solution treatment and artificial ageing. Due to a relatively high solubility (~14.5 wt.%) of Sn in Mg, the eutectic Mg_2Sn in most Mg-Sn alloys can be fully dissolved during the solution treatment.

Previously, most studies on Mg-Sn alloys focused on the peak aged state of each alloy and did not evaluate the ageing sequence. In 2018, Nie *et al.* reported a detailed ageing sequence for binary Mg-Sn alloys. Through high resolution STEM-HAADF analysis, a G. P. zone and a Mg_3Sn metastable phase (space group $Pm\bar{3}m$, a=0.453nm) were found prior to the formation of the Mg_2Sn phase[48]. During the ageing process, the super-saturated Mg-Sn solid solution forms G. P. zones, with a plate like morphology and a thickness of around 1.5nm (Figure 8).

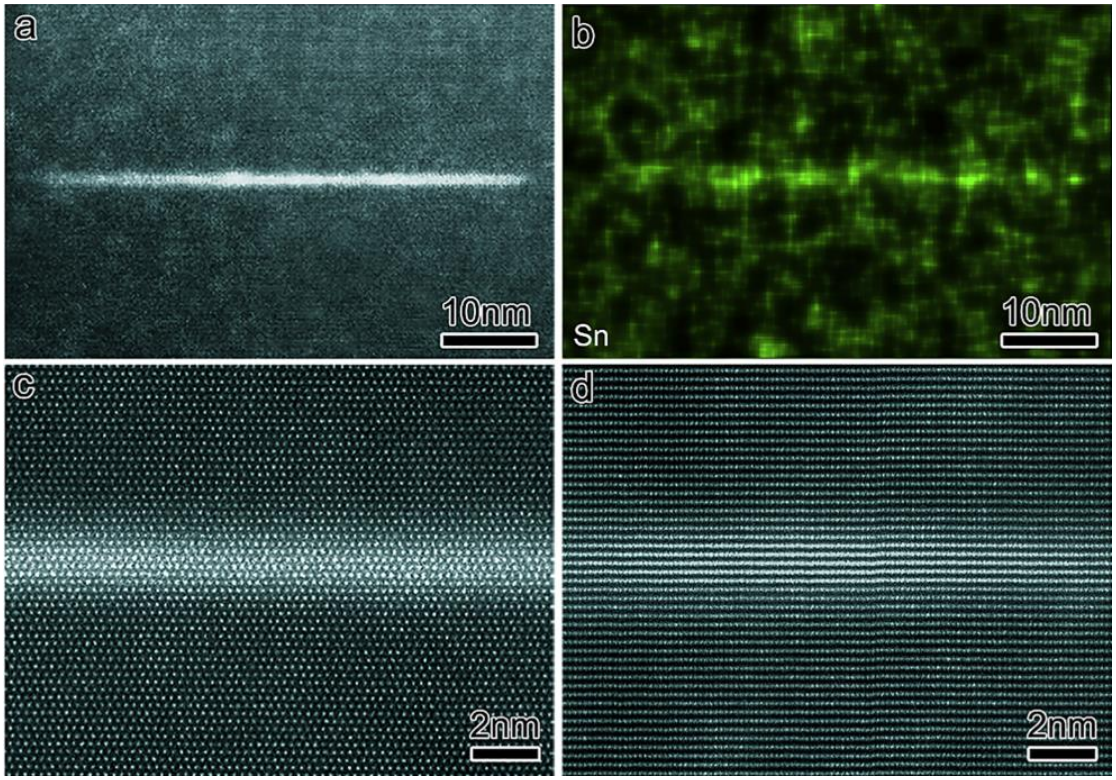


Figure 8 (a)STEM-HAADF image showing a GP zone in a Mg-9.8Sn (wt.%) sample aged at 100℃ for 2056h, (b) the corresponding EDS map for Sn, (c, d) atomic resolution STEM-HAADF images of a GP zone viewed along (c) $[2\bar{1}\bar{1}0]_{Mg}$ and (d) $[01\bar{1}0]_{Mg}$.[48]

During further ageing, a metastable Mg_3Sn phase, which they named β' formed from the G. P. zones. Figure 9 shows STEM-HAADF images viewed along $[2\bar{1}\bar{1}0]_{Mg}$ and $[01\bar{1}0]_{Mg}$ directions and the crystal structure and orientation of the Mg_3Sn phase.

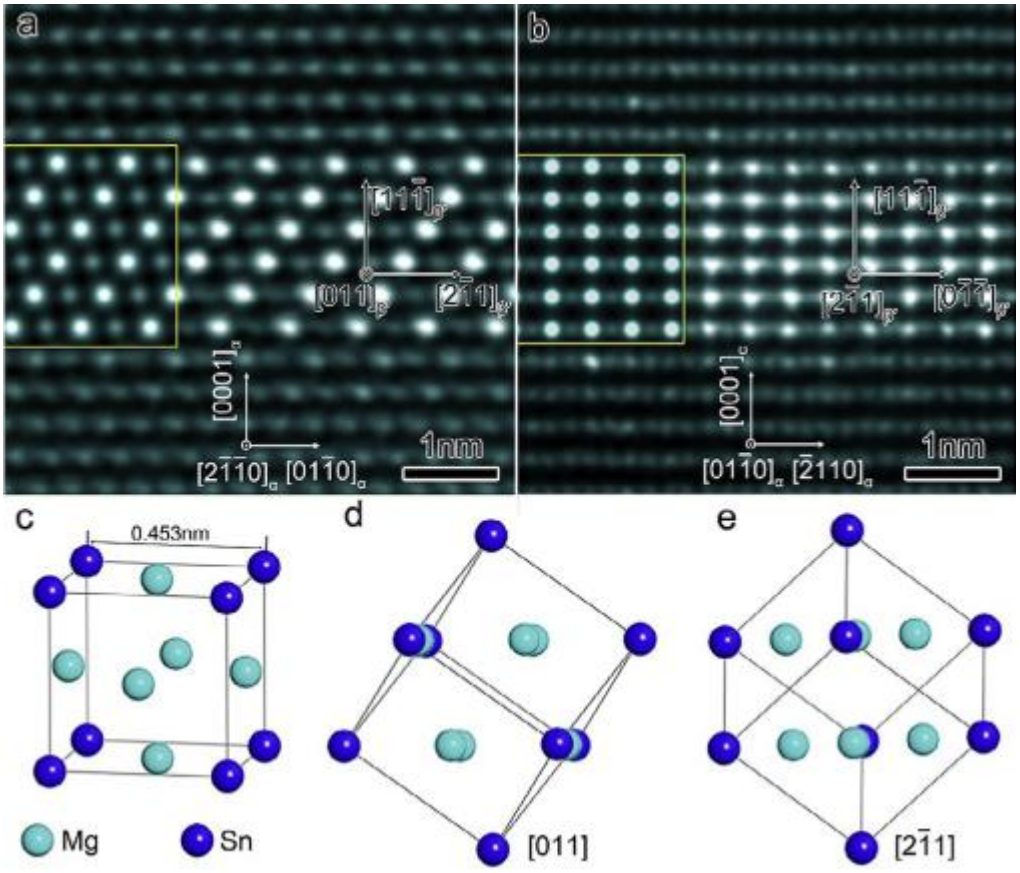


Figure 9 STEM-HAADF images along (a) $[2\bar{1}\bar{1}0]_{Mg}$ and (b) $[01\bar{1}0]_{Mg}$. Showing the structure of Mg_3Sn in the same sample aged for 2056h. (c) Schematic diagram showing the crystal structure of the Mg_3Sn phase. (d) Simulated Mg_3Sn crystal orientations corresponding to (a) and (b). The relevant structures are outlined by yellow rectangles. [48]

STEM-HAADF images have confirmed that there is a transformation from the G. P. zones to the Mg_3Sn phase, and then to the Mg_2Sn phase, as shown in Figure 10 and Figure 11. Observation indicates that the OR between the Mg matrix and the Mg_3Sn phase is $(0001)_{Mg} \parallel (11\bar{1})_{Mg3Sn}, [\bar{2}110]_{Mg} \parallel [011]_{Mg3Sn}$.

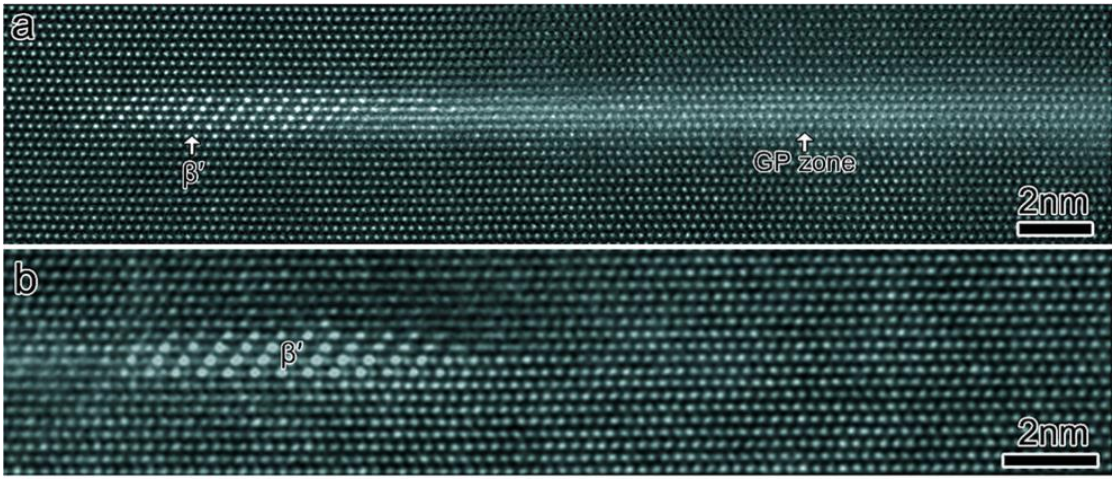


Figure 10 STEM-HAADF image showing the transition of the G.P. zone to the Mg_3Sn phase[48]

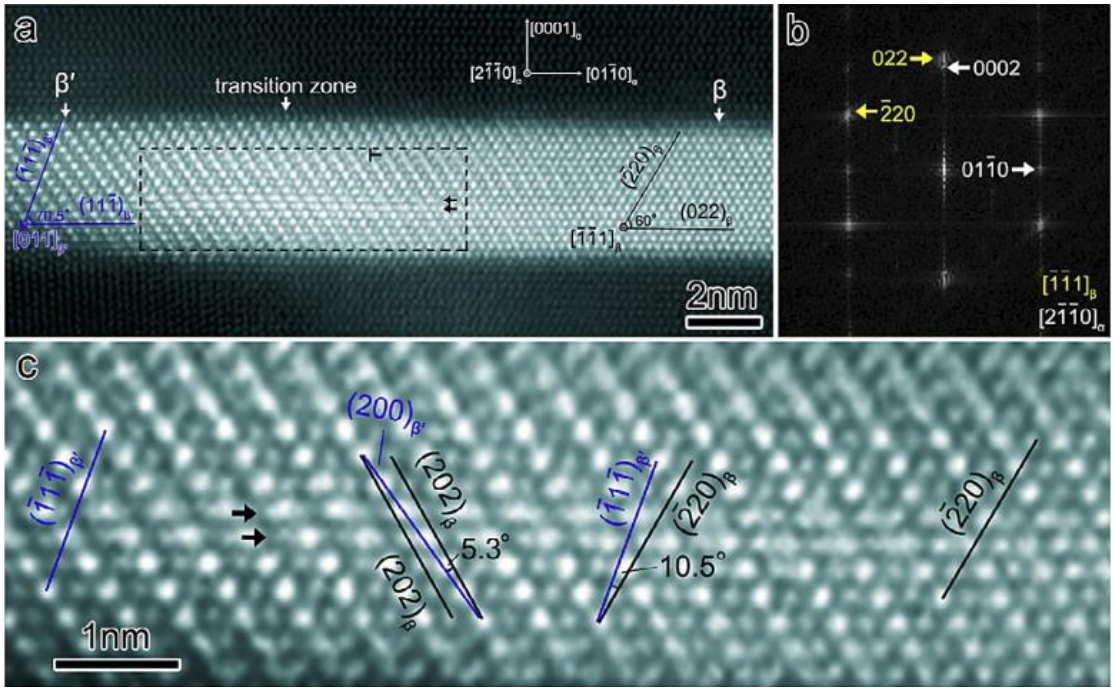


Figure 11 STEM-HAADF image showing the transition of the Mg_3Sn phase to the Mg_2Sn phase[48]

Therefore, the age hardening sequence of a binary Mg-Sn alloy can be determined as:

$$\mathrm{S.S.S.S} \rightarrow \mathrm{G.P.zone} \rightarrow Mg_3Sn(metastable) \rightarrow Mg_2Sn \quad \text{Equation 2-6}$$

One of the main shortcomings of the binary Mg-Sn alloy system is its slow age hardening response mainly due to the low diffusion coefficient of Sn in the Mg matrix. This can be improved by adding ternary alloying elements. Sasaki *et al.* reported that a Mg-9.9Sn (wt.%) alloy reached its peak hardness after ~250h of ageing at 180℃, but in only ~150h with 1.2 wt.% Zn added[49]. Elsayed *et al.* reported that an increase in hardness can still be observed in an Mg-9.9Sn (wt.%) alloy even after 1000h of ageing at 200℃. This can be reduced to 100h by a 3 wt.% Al addition. A combination of added elements also shortens the time needed to peak hardness to a great extent. Chen *et al.* reported that a Mg-3Sn-1Al (wt.%) alloy reached its peak hardness after ageing at 180℃ for 110h. With 2 wt.% Zn added to the alloy, the time to peak hardness can be shortened to 60h [50]. Mendis *et al.* reported that the time to peak hardness of a Mg-1.3Sn-1.2Zn-0.13Na (at%) alloy is 10h at 200℃ [5]. The peak hardness of a quinary Mg-9.8Sn-3Al-1.23Zn-0.1Na (wt.%) alloy was observed by Elsayed *et al.* after 9h at 200℃ [51]. Zhang *et al.* also reported that a Mg-5.29Sn-0.29Mn-0.22Si (wt.%) alloy reached its peak hardness after 10h at 150℃, 250℃ and 350℃ [52].

2.6 Precipitation in the Mg-Sn alloys

As described previously, basal slip is the dominating slip system in Mg alloys[15]. Non-basal precipitates are expected to be more effective at blocking basal slip, but the dominating habit plane of the precipitates in the Mg-Sn binary alloy is the basal plane, according to previous research by Henes and Gerold [8], Li *et al.* [53], Mendis *et al.* [54]. and Huang *et al.* [55]. It is, however, generally suggested that the habit planes of the precipitates can be controlled by heat

treatment and micro-alloying.

Many orientation relationships have been reported in previous research on Mg-Sn binary alloys. Early research by van der Planken[56], Henes and Gerold [8] reported 4 different kinds of different orientation relationships in a Mg-3.75wt.%Sn alloy and are listed in Table 7.

Table 7 Orientation relationships reported by Henes and Gerold[8]

Name	**Ageing temperature**	**OR**
OR1	160℃ ~ 200℃	$(0001)_{Mg} \parallel (110)_{Mg2Sn}, [2\bar{1}\bar{1}0]_{Mg} \parallel [001]_{Mg2Sn}$
OR2		$(0001)_{Mg} \parallel (110)_{Mg2Sn}, [2\bar{1}\bar{1}0]_{Mg} \parallel [1\bar{1}1]_{Mg2Sn}$
OR3	200℃ ~ 300℃	$(0001)_{Mg} \parallel (111)_{Mg2Sn}, [2\bar{1}\bar{1}0]_{Mg} \parallel [2\bar{1}\bar{1}]_{Mg2Sn}$
OR4		$(0001)_{Mg} \parallel (111)_{Mg2Sn}, [2\bar{1}\bar{1}0]_{Mg} \parallel [1\bar{1}0]_{Mg2Sn}$

These orientation relationships were later confirmed by Mendis *et al.* [54] and Sasaki *et al.* [49]. In addition, it was stated that the habit plane also varies with different heat treatment parameters, as listed in Table 8. It is suggested that a higher heat treatment temperature and double ageing makes possible the formation of pyramidal precipitates.

Table 8 Habit planes and heat treatment parameters in a Mg-3.75wt.%Sn alloy [8]

Ageing parameters	**Habit plane of Mg_2Sn phase in the Mg matrix**
200℃	(0001)
250℃	(0001)
Repeated aging at 250℃	(0001) and increasing $(10\bar{1}2)$

	precipitates on repetition
300℃	(0001) and $(10\bar{1}2)$
Cooling from 560℃ at 22℃/h	(0001), $(10\bar{1}1)$ and $(10\bar{1}2)$

For Mg-Sn alloys with ternary elements, Mendis *et al.* [5] found there are 3 types of precipitate morphologies in a Mg-6Sn-3Zn (wt.%) alloy (peak aged at 200℃): type 1 laths along the basal plane, type 2 laths along the prismatic plane and pyramidal type 3 laths which is less prevalent. The orientation relationship for type 1 and type 2 precipitates is $(0001)_{Mg} \parallel (111)_{Mg2Sn}, [2\bar{1}\bar{1}0]_{Mg} \parallel [1\bar{1}0]_{Mg2Sn}$ (OR4) and that of type 3 precipitates is $(0001)_{Mg} \parallel (110)_{Mg2Sn}, [2\bar{1}\bar{1}0]_{Mg} \parallel [1\bar{1}1]_{Mg2Sn}$ (OR2). The alloy showed better age-hardening response than binary Mg-6Sn, mainly due to a better precipitate distribution and the appearance of non-basal precipitates. Elsayed *et al.* [7] prepared Mg-9.9Sn (wt.%) alloys with different Al concentrations. Only basal precipitates existed in the binary alloy but there was an increasing occurrence of non-basal precipitates with increasing Al concentration. An additional orientation relationship is reported in the Mg-2.2Sn-3Al (at%) alloy peak aged at 200℃: $(10\bar{1}0)_{Mg} \parallel (1\bar{1}0)_{Mg2Sn}, [11\bar{2}0]_{Mg} \parallel [002]_{Mg2Sn}$. The addition of Al also promotes a refined precipitate distribution.

The morphology of the Mg_2Sn precipitates varies with different alloy composition and heat treatment parameters as well. Precipitates growing on the basal plane can either be plate-shaped [57], lath-shaped [58] or rod-shaped [59]. The pyramidal precipitates are normally lath-shaped [5], [57]. Rod-shaped precipitates normally grow along the $[0001]_{\alpha}$ direction [58].

The competition between the different orientation relationships and habit planes of Mg_2Sn

precipitates is quite complex. As summarized by Nie *et al.*, by 2018 14 types of orientation relationships had been reported for various Mg-Sn alloys[48]. A summary of the reported habit planes (HPs) and ORs for different Mg-Sn alloys can be found in Table 9.

According to previous studies of the orientation relationships and habit planes, the relationship between habit plane and orientation relationship is quite complex. The same orientation relationship may occur with different habit planes and vice versa. If the habit planes of the Mg-Sn alloys can be predicted and controlled, improvements in mechanical properties might be achieved.

Table 9 Summary of the reviewed Mg-Sn alloys with their compisition, ageing temperature, ageing time and precipitation distribution

Author	**Composition (wt.%)**	**Ageing temperature (℃)**	**Ageing time (h)**	**HP and OR**
Henes & Gerold[8]	Mg-3.75Sn	160	430	Basal: HP: (0001), OR: $(110)_\beta \parallel (0001)_\alpha, [1\bar{1}1]_\beta \parallel [2\bar{1}\bar{1}0]_\alpha$
Henes & Gerold[8]	Mg-3.75Sn	300	15	Basal: HP: (0001), OR: $(110)_\beta \parallel (0001)_\alpha, [1\bar{1}1]_\beta \parallel [2\bar{1}\bar{1}0]_\alpha$ Pyramidal: HP: $(10\bar{1}2)$, OR: $(110)_\beta \parallel (0001)_\alpha, [001]_\beta \parallel [2\bar{1}\bar{1}0]_\alpha$
Henes & Gerold[8]	Mg-3.75Sn	250	42	Basal: HP: (0001), OR: $(111)_\beta \parallel (0001)_\alpha, [1\bar{1}0]_\beta \parallel [2\bar{1}\bar{1}0]_\alpha$ Pyramidal: HP: $(10\bar{1}2)$, OR: $(110)_\beta \parallel (0001)_\alpha, [1\bar{1}1]_\beta \parallel [2\bar{1}\bar{1}0]_\alpha$
J. F. Nie[57]	Mg-9.8Sn-1.2Zn	200	88	Basal: HP: (0001), OR: $(111)_\beta \parallel (0001)_\alpha, [1\bar{1}0]_\beta \parallel [2\bar{1}\bar{1}0]_\alpha$ Pyramidal: HP: Undefined, OR: $(0001)_\alpha$~15.4°$(1\bar{1}0)_\beta$, $[2\bar{1}\bar{1}0]_\alpha \parallel [110]_\beta$ Prismatic: OR: $(110)_\beta \parallel (0001)_\alpha, [001]_\beta \parallel [2\bar{1}\bar{1}0]_\alpha$
Sasaki[59]	Mg-9.8Sn-1.2Zn-0.1Mn	200	40	Basal: HP: (0001), OR: $(111)_\beta \parallel (0001)_\alpha, [1\bar{1}0]_\beta \parallel [2\bar{1}\bar{1}0]_\alpha$ Pyramidal: HP:$(11\bar{2}2)$, OR: Unidentified Prismatic: $(110)_\beta \parallel (0001)_\alpha, [1\bar{1}1]_\beta \parallel [2\bar{1}\bar{1}0]_\alpha$
Sasaki[49]	Mg-9.8Sn-1.2Zn	200	40	Basal: HP: (0001), OR: $(111)_\beta \parallel (0001)_\alpha, [1\bar{1}0]_\beta \parallel [2\bar{1}\bar{1}0]_\alpha$ Pyramidal: HP:$(11\bar{2}2)$, OR: Unidentified Prismatic: $(110)_\beta \parallel (0001)_\alpha, [1\bar{1}1]_\beta \parallel [2\bar{1}\bar{1}0]_\alpha$
Elsayed[7]	Mg-9.9Sn-3Al	200	50	Basal: HP: (0001), OR: $(111)_\beta \parallel (0001)_\alpha, [1\bar{1}0]_\beta \parallel [2\bar{1}\bar{1}0]_\alpha$/ $(10\bar{1}0)_\alpha \parallel (1\bar{1}0)_\beta$, $[2\bar{1}\bar{1}0]_\alpha \parallel [002]_\beta$ Pyramidal: Not specified
W. Z. Zhang[52]	Mg-5.3Sn-0.3Mn-0.2Zn	250	10	Basal: HP: (0001), OR: $(110)_\beta \parallel (0001)_\alpha, [001]_\beta \parallel [2\bar{1}\bar{1}0]_\alpha$
Mendis[5]	Mg-6Sn	200	200	Basal: HP: (0001), OR: $(111)_\beta \parallel (0001)_\alpha, [1\bar{1}0]_\beta \parallel [2\bar{1}\bar{1}0]_\alpha$
Mendis[5]	Mg-6Sn-3Zn	200	100	Basal: HP: (0001), OR: $(111)_\beta \parallel (0001)_\alpha, [1\bar{1}0]_\beta \parallel [2\bar{1}\bar{1}0]_\alpha$ Prismatic: OR: $(110)_\beta \parallel (0001)_\alpha, [112]_\beta \parallel [01\bar{1}0]_\alpha$ Prismatic: $(110)_\beta \parallel (0001)_\alpha, [1\bar{1}1]_\beta \parallel [2\bar{1}\bar{1}0]_\alpha$

The exact mechanism of how micro-alloying alters the morphology and orientation relationship of the precipitates remains unknown, although several explanations have been put forward. Thermodynamically, Zhang *et al.* suggested that the competition between chemical free energy and strain energy provides the driving force for phase transformation which therefore results in a variation of habit plane [6]. It is also suggested by Elsayed *et al.* that the addition of micro-alloying elements helps to alter the interfacial energy between Mg_2Sn and the Mg matrix [7]. Mendis *et al.* reported that the exact mechanisms for different alloying elements may be very different, the addition of Na helps to increase the number density of the precipitates while Zn contributes more to precipitate morphology [5]. Liu *et al.* used STEM-HAADF to study the interface structure of a Mg-9.8Sn-1.2Zn alloy and found that Zn is segregated to the interface and might have changed the interface structure and energy [57]. However, the same effect is not found in the Mg-5Sn-3Zn-0.1Mn alloy of Shi[60]. Current problems in predicting the orientation relationships and morphologies of precipitates in the Mg-Sn alloy system stem from inability to determine the key parameters such as interfacial energy and strain energy. A few existing studies that have modelled the nucleation and growth of precipitates either "selected" an interfacial energy value without confirmation [6], or were inadequate to be applied to the complex precipitate distribution in the Mg-Sn system [61]. Additionally, different alloying elements exhibit different effects on precipitation and cannot be treated equally.

Some crystallographic models have also been presented describing different HPs and ORs. Among them there are edge-to-edge matching models of Zhang *et al.*[62], [63], but the as-predicted ORs have not been observed in the actual alloys. Zhang and her group have widely applied the coincidence site lattice (CSL), constrained coincidence site lattice (CCSL) and O-lattice model to describe the present ORs in Mg-Sn alloys and have had some

success[60], [64], [65]. However, confirmation is still required that the predicted interfacial structure agrees with the actual structure in the practical alloy.

In general, accurate prediction and control of morphologies and orientation relationships is still currently difficult. None can claim a systematic approach to estimating HPs and ORs. Such a model should involve both thermodynamic and crystallographic input and still requires intense work to develop.

2.7 Mg-Sn alloys strengthened by various types of precipitates

The advantage of non-basal precipitates over basal precipitates in Mg-Sn alloys is that they are more capable of blocking basal slip. The effect of precipitate strengthening mainly lies in precipitate shearing and Orowan strengthening, where dislocations bow around particles and introduce additional Orowan stress. Based on Hutchinson's equation for estimating the critical size of precipitates for shearing (Section 2.4.3), the critical size of Mg_2Sn precipitates in Mg-Sn alloys is 3.14nm, while that for $MgZn_2$ precipitates is 2.74nm [32]. Therefore, as the precipitates in Mg-Sn alloys are normally larger than 20nm, precipitate shearing can be disregarded, leaving Orowan strengthening the only possible precipitation strengthening mechanism.

The general Orowan strengthening equation assumes that all the precipitates are spherical particles. This simplifies the general calculation but is incapable of predicting the Orowan strengthening effect for complex precipitate morphologies. Nie has derived various mean particle spacings (λ) for different types of precipitates and these can be found in Table 10.

Table 10 Mean particle spacings for different types of precipitate in magnesium alloys[66]

Precipitate type	**Mean particle spacing λ**
Spherical	$\lambda = L_p - d_p = \frac{1.075}{\sqrt{N_A}} - \frac{\pi d_t}{4} = \left(\frac{0.779}{\sqrt{f}} - 0.785\right) d_t$
Basal spherical plates	$\lambda = L_p - d_p = \left(\frac{0.953}{\sqrt{f}} - 1\right) d_t$
Prismatic spherical plates	$\lambda = L_p - \frac{d_p}{2} - \frac{\sqrt{3} t_p}{2} = 0.825 \sqrt{\frac{d_t t_t}{f}} - 0.393 d_t - 0.866 t_t$
C-axis rods	$\lambda = L_p - d_p = \left(\frac{0.953}{\sqrt{f}} - 1\right) d_t$

where L_p is the planar centre-to-centre inter-precipitate spacing, d_p/d_t the mean planar diameter of the point obstacles (precipitates), t_t the thickness of a planar particle, N_A the number of particles intersected by unit area of slip plane and f the volume fraction of precipitates[66].

Currently, calculations on the Orowan strengthening effect have been attempted by various of existing works in different Mg alloys. Wan *et al.*, Si *et al.*, Zhang *et al.* and Li *et al.* calculated the effect of Orowan strengthening effect in different Mg-Al alloys [67]–[69]. Alizadeh *et al.* and Wang *et al.* made their attempt on the Mg-Zn alloy system [70], [71] and Yu *et al.* evaluated a Mg-Gd-Li-Y system [72]. The common ground of these studies is that they focused on the alloy systems that contains only one precipitate type, therefore modelling the precipitation strengthening will be more straightforward as only one set of effective mean particle spacings and effective particle radius is needed.

As for the Mg-Sn alloy system, the precipitate distribution varies with alloy composition and heat treatment. Based on the literature, multiple precipitate morphologies exist in different Mg-Sn alloys. Basal laths[7], [54], pyramidal laths[7], [49] and prismatic laths[5], [60] have all been found in Mg-Sn alloys and require different parameters. No existing studies have attempted to make an estimation on a system with multiple precipitate types. Therefore, in order to accurately predict the effect of Orowan strengthening, a proper model is required to estimate the strengthening behaviour in the Mg-Sn alloy system.

3 Aim and objectives

This project aims to understand the characteristics and effects of precipitates with different habit planes (HPs) and orientation relationships (ORs) in the Mg-Sn-X alloy system. The specific objectives are as follows:

To study the morphology, chemistry and crystallography of the precipitates in three Mg-Sn series alloys, being respectively Mg-6Sn, Mg-6Sn-3Al, Mg-6Sn-3Zn (wt.%).

To examine how different alloying elements affect the crystallography of the Mg_2Sn precipitates and how non-basal precipitates affect basal slip in Mg-Sn alloys.

To estimate the Orowan strengthening effect of non-basal precipitates and the cooperative strengthening effect between different types of precipitates.

4 Experimental methodology

4.1 Raw materials

The raw materials used for casting were pure Mg (99.9%), pure Al (99.9%), pure Zn (99.9%) and pure Sn (99.95%). The Sn was from William Rowland Ltd. and the Mg, Al and Zn from the department foundry stock. Before casting, the magnesium pieces were mechanically polished for a short period of time in order to remove the surface oxide.

4.2 Sand casting

The ingots used in this study were prepared by a bottom-fed sand-casting system. The design of the casting mould is shown below in Figure 12.

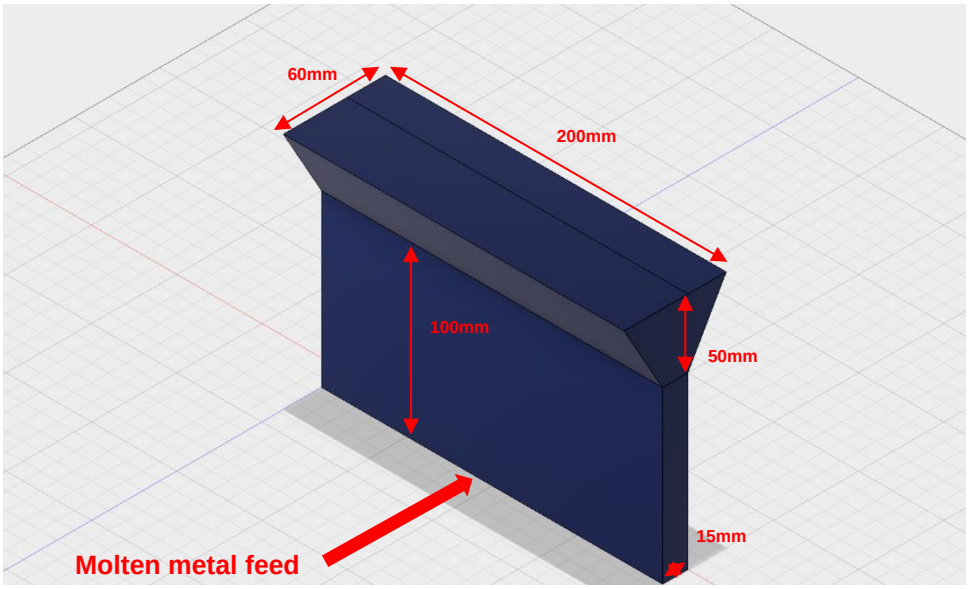


Figure 12 Design of the sand-casting system

The designed size of the ingot was 200mm*100mm*15mm. A feeder (the trapezium part) was applied to the top of the mould to minimize casting shrinkage. The molten metal was heated to 750℃ and then cast. Due to the nature of sand casting, the grain size of the alloys was on the

scales of millimetres. 3 alloys were cast with their respective target compositions Mg-6Sn, Mg-6Sn-3Al and Mg-6Sn-3Zn (wt.%), equivalent to Mg-1.4Sn, Mg-1.4Sn-3Al and Mg-1.4Sn-1.3Zn (at%), respectively.

4.3 Heat treatment

The as-cast alloys were then cut into long bars with an approximately 1.5cm^2 cross-section. The bars were sealed into quartz tubes filled with argon to ensure there is minimal oxidation. The as-cast alloys were homogenized and solution treated at 500℃ in a muffle furnace for 48 hours to dissolve any precipitate formed during the casting process and to improve the homogeneity of the sample. During the heat treatment, the samples may form Mg_2Si due to the reaction between the alloy and the quartz tube. The as-solution treated samples were finally mechanically ground to remove any possible Mg_2Si or oxidation. The as-solution treated samples were then artificially aged at 200℃ for, respectively, 2h, 5h, 10h, 24h, 48h, 72h, 96h, 144h and 312h in an oven.

4.4 Microstructure characterization

4.4.1 Optical microscopy (OM)

Optical microscopy is used as a generic method of microstructure characterization as it gives a wide range of view. 2mm slices were cut from the ingot and ground using silicon carbide grinding papers graded from P120 to P1200. The samples were then polished using a 1μm diamond polishing compound for a mirror-like surface. As magnesium oxidises rapidly, ethanol, rather than water was used during the polishing. The sample was etched for 5 seconds to reveal the precipitates. The etchant was a nitric acid solution (80% ethanol, 20% nitric acid solution (from a 70% nitric acid and 30% water)). One important feature of the Mg-Sn alloys is that the

as-etched surface is normally rough, mainly due to the corrosion product of insoluble $Sn(OH)_4$, as suggested by the Pourbaix diagram of tin, shown as Figure 13. Therefore, an ultrasonic bath in ethanol is helpful as it removes some of the corrosion product from the sample. Optical microscopy was performed with a Zeiss Axioskop microscope with 50x-500x magnification.

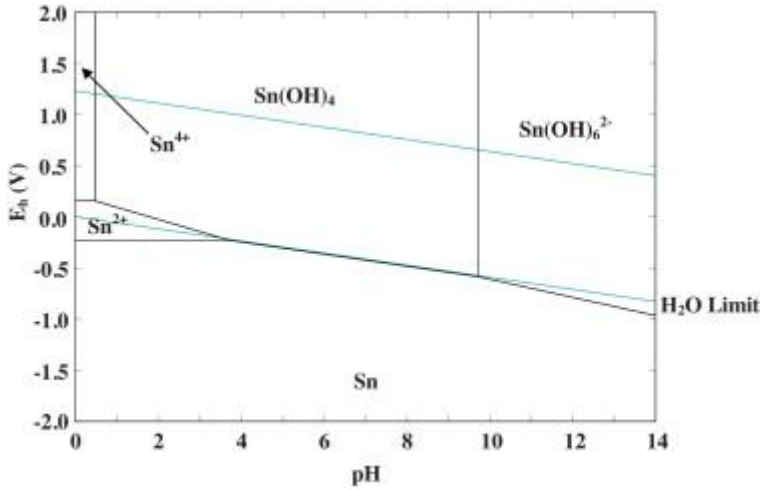


Figure 13 Tin-H_2O Pourbaix diagram at room temperature showing the insoluble corrosion product of $Sn(OH)_4$[73]

4.4.2 Scanning electron microscopy (SEM)

Theoretically, the limit of resolution in any microscope is given by the following equation:

$$d_{min} = \frac{\lambda}{2 \sin \alpha} \qquad \text{Equation 4-1}$$

where λ is the wavelength and α is the diffracted wave half angle. The equation suggests that the resolution of a microscope is dependent on wavelength. Therefore, due to the very short wavelength of the electron wave (theoretically ~$8.5*10^{-3}$ nm at 20kV compared to 400~700nm for light), electron microscopy is capable of revealing features with a very high resolution.

A MIRA TESCAN scanning electron microscope operating at 20kV for imaging and 15kV for EDS analysis was used to study the microstructural details of the as-prepared alloys. Generally, samples for optical microscopy are suitable for characterization by SEM.

4.4.2.1 Contrast mechanisms in conventional SEM imaging

In the secondary electron imaging mode, the precipitates present as the bright part and the matrix as the dark part, as the contrast of the secondary electron imaging is given by the height difference of the sample surface. In the backscattered electron imaging mode, the precipitates again present as the bright part and the matrix as the dark part. This is because the intensity of the backscattered electron image is affected by the atomic mass of the elements. Therefore, the precipitates containing Sn are brighter than the matrix, which is mainly Mg.

4.4.2.2 Chemical and grain orientation analysis in SEM

Energy dispersive spectrometry (EDS) characterization can also be performed by the attached Oxford Instruments X-max detector. The voltage used for EDS was 15kV and the dead time was given at around 30% for the conditions chosen, providing an appropriate number of X-ray signal.

The grain orientation determination for micro-pillar compression was performed by Electron BackScatter Diffraction (EBSD) at 20kV. For the Mg-Sn alloys, EBSD sample preparation needs to be very careful due to the existence of the above-mentioned $Sn(OH)_4$. Normally EBSD requires a high sample surface quality and therefore there should not be any remaining corrosion product on the sample. The approach to acquire reasonable EBSD samples is to perform fine mechanical polishing instead of using any etchant. In this study, EBSD samples were prepared using P120-P1200 silicon carbide grinding papers, followed by 1μm diamond suspension and finally 0.04μm colloidal silica.

4.4.2.3 TEM sample preparation and micro-pillar fabrication in SEM assisted by Focused Ion Beam (FIB)

FIB has proven to be a powerful tool to prepare TEM and microscale testing samples. In

the present work, thin TEM foils and micro-pillars were prepared by a FEI Helios FEG Dual Beam (SEM/FIB) with a Xe plasma source. By performing EBSD analysis prior to FIB, TEM foils with the desired foil normal can easily be acquired. Micro-pillars for compression tests can also be produced by FIB. Pillars with the desired loading directions and Schmid factors can be acquired via previous EBSD analysis.

4.4.3 X-ray diffraction analysis (XRD)

In order to identify the phases in the as-prepared alloys, an Inel Equinox 3000 X-ray diffraction system has been used. During the XRD scan, the 2θ angle ranges from 0°~115°. Each scan is performed for 30min for a sufficient number of counts. ~50000 counts were normally acquired for each sample. The structure factor of the Mg_2Sn crystal is:

$$F_{hkl} = \begin{cases} 4f_{Sn}, & h+k+l = 2N+1 \\ 4\left(f_{Sn} - 2f_{Mg}\right), & h+k+l = 4N+2 \\ 4\left(f_{Sn} + 2f_{Mg}\right), & h+k+l = 4N \end{cases} \quad \text{Equation 4-2}$$

The as-acquired XRD data was then processed by Jade 5.0 software to identify the phases in the sample.

4.4.4 Transmission electron microscopy (TEM)

A FEI Talos F200X and a FEI Tecnai F30 transmission electron microscope has been used to study in detail the morphology and orientation of the precipitates. The morphologies of the precipitates were studied using bright field (BF) and dark field (DF) imaging as well as scanning transmission electron microscopy (STEM). The structure and orientation relationships were studied by selected area electron diffraction (SAED) and the chemical compositions of the precipitates were determined by using energy dispersive spectrometry (EDS) in STEM-HAADF imaging mode. To analyse the T-shaped precipitates in the Mg-6Sn-3Zn alloys, a

tomography holder with a tilting range of -70°~70° was chosen followed by 3D tomographic reconstruction.

The TEM samples were either prepared using twin-jet polishing or by SEM-FIB. To prepare the TEM samples via twin jet polishing, the samples were first cut into thin slices, punched into 3 mm discs and thinned down to less than 200μm with P1200 grinding paper. Final polishing was performed by a Tenupol-3 twin jet polisher. The twin jet polishing was carried out with a solution which consisted of 10g lithium chloride, 22g magnesium chloride, 200ml butoxyethanol and 1000ml methanol. In order to minimize oxidation, the solution was cooled down by liquid nitrogen to -20℃~-30℃. The voltage used for polishing was ~90V.

For the determination of the chemical composition of the precipitates in the TEM samples, as the matrix and the precipitate will both contribute to the EDS signal, the chemical composition of the precipitates cannot be determined by directly putting the beam on the precipitate. Many data points were taken from different precipitates. The competition between the matrix and the precipitates will be different, but the atomic ratios of the precipitates will remain unchanged and can subsequently be acquired by quantitative analysis. The detailed approach used for determining the chemical composition of the precipitates will be described in Chapter 5.

In order to accurately determine the shape of the T-shaped precipitates formed in the Mg-6Sn-3Zn (wt.%) alloys, HAADF imaging was used as the Z-contrast strongly suppresses the diffraction contrast and is therefore very useful to produce images for tomography reconstruction. HAADF images were taken over a tilt range of -70°~70° with an angular interval of 2°. 70 images were taken for each precipitate and were processed by the TomoJ plugin of ImageJ to produce a stack of ~400 images. The stacked images were then reconstructed using the ChimeraX software for a 3D model.

Determination of orientation relationships between the precipitate and the matrix was performed by stereographic projection analysis. Zone axis diffraction patterns from each phase were recorded by TEM and plotted on a stereographic diagram and all other main axes were constructed. The as-reconstructed stereographic diagram shows a series of superimposed zone axes which therefore indicate the parallel directions and planes. The stereographic diagrams in this study were produced by CrystalMaker and SingleCrystal.

4.5 Hardness

The hardness of the alloys was measured using a Mitutoyo MVK-H1 hardness tester fitted with a Vickers indenter to produce an age hardening curve. The Vickers hardness is one of the most widely applied hardness testing techniques. The advantages of the Vickers hardness include:

Hardness values are independent of the size of the indenter tip and the load.

No need to change the indenter tip for different materials.

The square indent is easy to measure.

The Vickers hardness is produced by using a pyramidal shaped diamond indenter with a tip angle of 136°. The Vickers hardness is calculated as follows:

$$\mathrm{HV} = \frac{F}{S} = \frac{2F \cdot \sin\frac{136^\circ}{2}}{g \cdot d^2} \cong 0.1891 \cdot \frac{F}{d^2} \qquad \text{Equation 4-3}$$

where F is the load, S is the surface area of the indent, d is the diagonal length of the indent and g is the gravitational acceleration. Generally, samples suitable for optical microscopy can be used for hardness tests (without etching). The load was 50g held for 10s. 20 measurements were taken from each sample to improve accuracy.

5 Characterization of precipitates in Mg-Sn alloys

5.1 Introduction

The work related in this thesis focus on the Mg-Sn alloy system, which is a competitive replacement for the Mg-RE alloys. As the morphology and crystallography of the precipitates in the Mg-Sn alloy system vary greatly with alloy composition and heat treatment, Mg-6Sn, Mg-6Sn-3Al and Mg-6Sn-3Zn (wt.%) were selected in this study. The addition of 6% Sn produces a moderate number of precipitates, while Al and Zn, based on the existing literature, have the effect of promoting non-basal precipitates. As the Mg-Sn alloy system is precipitation strengthened, it is vital to characterise the precipitates before any analysis on strengthening behaviour can be performed. The precipitates in the three alloys have been analysed for their morphology, crystallography and chemistry by a combination of OM, SEM and TEM both as-cast and peak-aged.

5.2 Characterisation of the as-cast alloys

The chemical compositions of the as-prepared alloys were measured by SEM-EDS. In order to assure the accuracy of the EDS measurement, 10 measurements were taken across the sample. Standardized ZAF quantification was applied, where Z is the atomic number correction, A is the absorption correction and F is the florescence correction. The nominal and measured compositions of the as-cast alloys are shown in Table 11 below.

Table 11 Chemical composition of the as-cast Mg-Sn alloys measured by SEM-EDS (wt.%)

Alloy	**Composition wt.%/at%**	**Mg/%**	**Sn/%**	**Al/%**	**Zn%**	**Bal.%**

Mg-Sn	Nominal	94.00/98.71	6.00/1.29	0	0	0
	Measured	93.47/98.52	6.25/1.35	0	0	0.28/0.13
Mg-Sn-Al	Nominal	91.00/95.86	6.00/1.69	3.00/2.85	0	0
	Measured	89.96/95.59	6.78/1.47	2.89/2.77	0	0.37/0.17
Mg-Sn-Zn	Nominal	91.00/97.49	6.00/1.32	0	3.00/1.19	0
	Measured	90.30/97.15	5.89/1.30	0	3.32/1.33	0.49/0.22

The microstructures of the as-cast alloys were characterized by OM and SEM:

5.2.1 Optical microscopy

Optical microscope images of Mg-6Sn, Mg-6Sn-3Al and Mg-6Sn-3Zn are shown in Figure 14, Figure 15 and Figure 16. The α-Mg matrix is indicated by a red arrow and the Mg_2Sn phase is indicated by a green arrow. The two phases can be found clearly in the images, but the contrast at high magnification is not adequate. Therefore, SEM was used for further microstructure characterization using back-scattered electron mode to give better contrast.

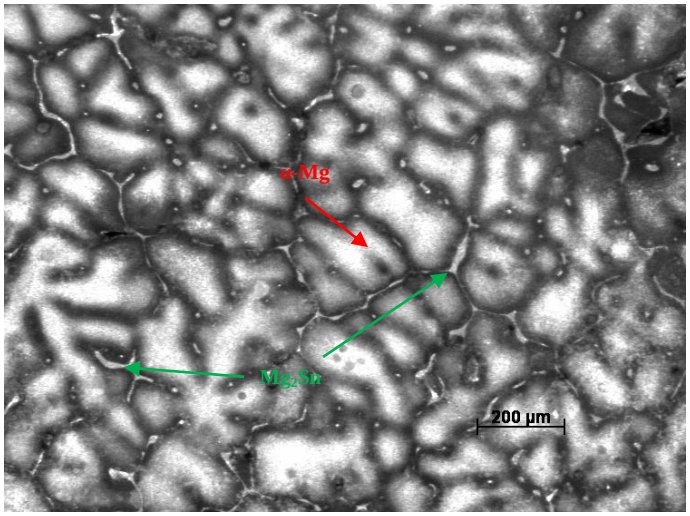


Figure 14 Optical microscope image of as-cast Mg-6Sn alloy

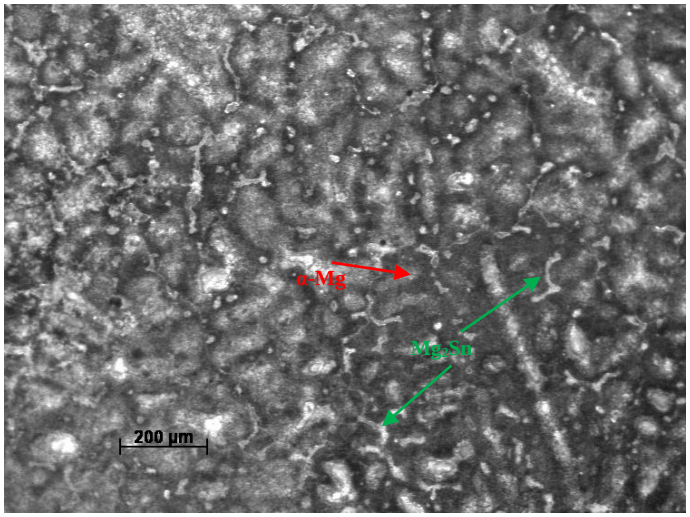


Figure 15 Optical microscope image of as-cast Mg-6Sn-3Al alloy

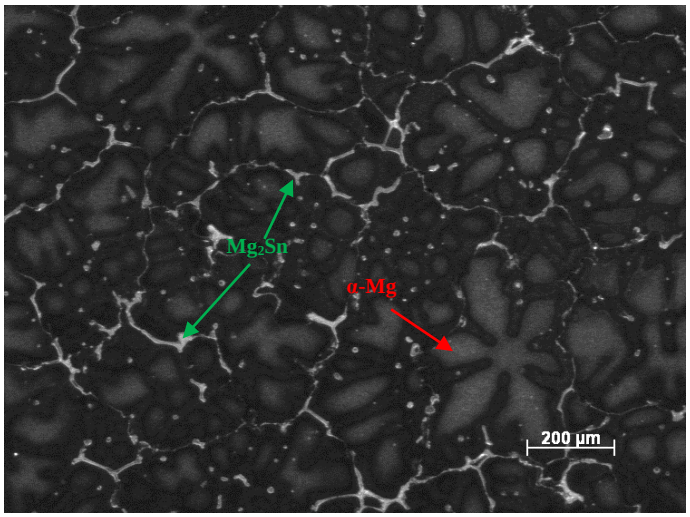


Figure 16 Optical microscope image of as-cast Mg-6Sn-3Zn alloy

5.2.2 SEM

Backscattered electron images of Mg-6Sn, Mg-6Sn-3Al and Mg-6Sn-3Zn have been acquired and are shown in Figure 17, Figure 18 and Figure 19, respectively, to better describe the microstructures and phase distributions of the as-cast alloys. In the SEM images, the α-Mg matrix is the dark part and the Sn-rich area is the bright part based on the back-scattered electron contrast mechanism. The Sn enrichment and Mg_2Sn precipitates are mostly on the grain boundaries. This is due to the change of liquid composition during the solidification process.

As the liquid composition moves along the liquidus line in the phase diagram, the liquid that solidifies last will exhibit the highest Sn concentration, leading to the formation of an Sn-rich area and the eutectic Mg_2Sn phase.

Another feature of the as-cast microstructures is that the distribution of Mg_2Sn phase is refined in the Mg-6Sn-3Al alloy. The area fraction of the precipitates was calculated using ImageJ. The precipitates in Mg-6Sn, Mg-6Sn-3Al and Mg-6Sn-Zn occupy 1.3%, 1.4% and 2.1% respectively of the area fraction. However, it can be found clearly from the images that the precipitates in the Mg-6Sn-3Al alloy are finer than in the other alloys, which is in good agreement with Elsayed *et al.* [7]. A refined microstructure in the Mg-6Sn-3Al alloys will lead to higher hardness as-cast.

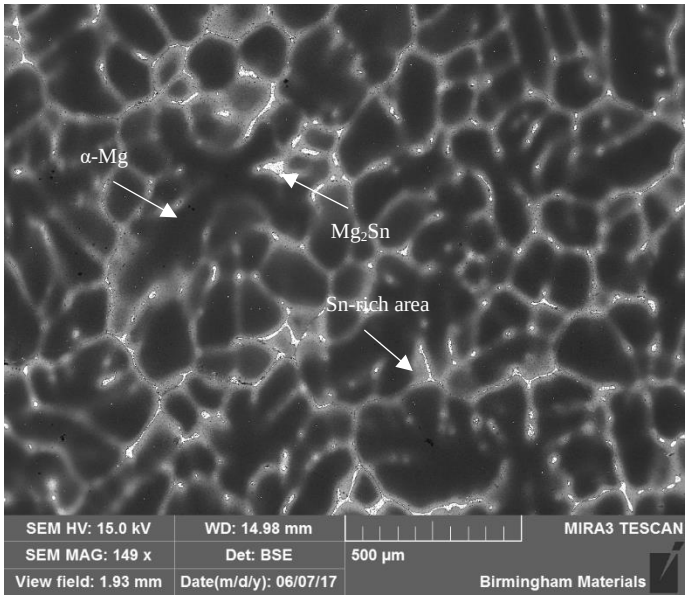


Figure 17 As-cast structure of Mg-6Sn alloy

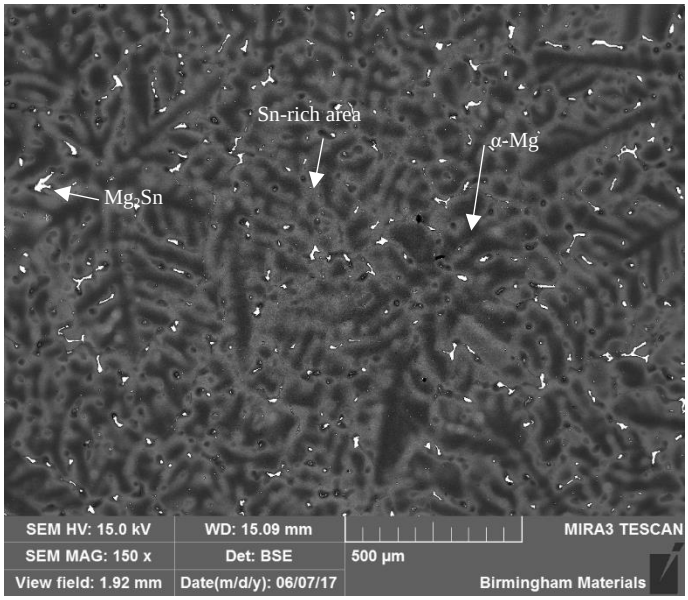


Figure 18 As-cast structure of Mg-6Sn-3Al alloy

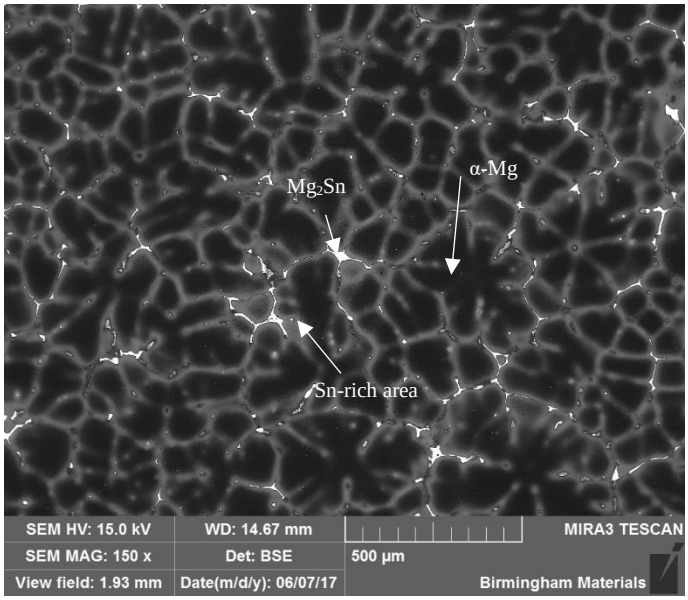


Figure 19 As-cast structure of Mg-6Sn-3Zn alloy

5.3 Age hardening response of the as-aged Mg-6Sn alloys

All three Mg-Sn alloys were solution treated at 500℃ for 48h and then aged at 200℃ until peak hardness was observed. 20 indents were made on each of the aged specimens. The hardness of the as-cast alloys is shown below in Figure 20.

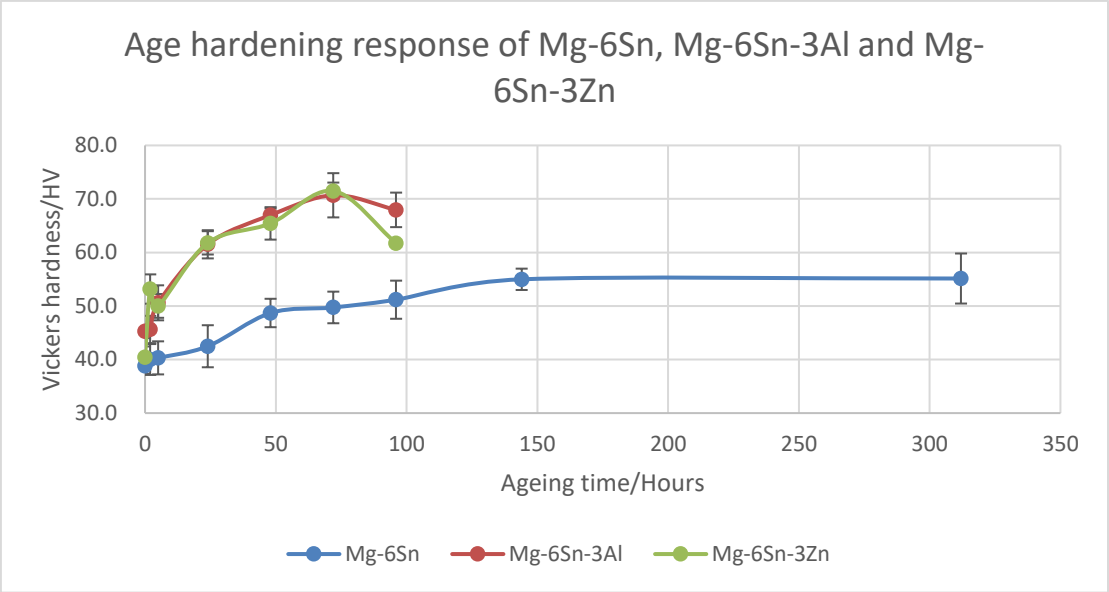


Figure 20 Vickers micro-hardness acquired from the Mg-Sn alloys with 50g load

For the Mg-6Sn binary alloy, peak hardness is not observed until an ageing time of 144h is reached. According to the existing data, this is mainly due to the low diffusion coefficient of Sn in Mg, which was previously studied by Zhou *et al.*[74]. For example, at 200 °C, the basal and normal diffusion coefficients of Al in Mg are $1.26*10^{-38}m^2/s$ and $2.78*10^{-39}m^2/s$ respectively while those of Sn in Mg are $6.83*10^{-39}m^2/s$ and $1.42*10^{-39}m^2/s$ respectively.

The two ternary alloys exhibit a better age hardening response, as can be seen from the peak hardness values and times until peak hardness. An increment of ~15HV is observed in both alloys, which can be seen reaching their peak hardness at around 72h.

5.4 Studying the precipitates in Mg-Sn alloys

In order to identify the phases present in all three Mg-Sn alloys, XRD as well as STEM-EDS has been applied. For the XRD analysis, considering the possible phases based on the chemical composition of the alloys as well as the phase diagram, α-Mg, Mg_2Sn, $Mg_{17}Al_{12}$ and

$MgZn_2$ were selected for matching. The XRD spectra for all three alloys at peak ageing can be found below with the peaks of each phase marked.

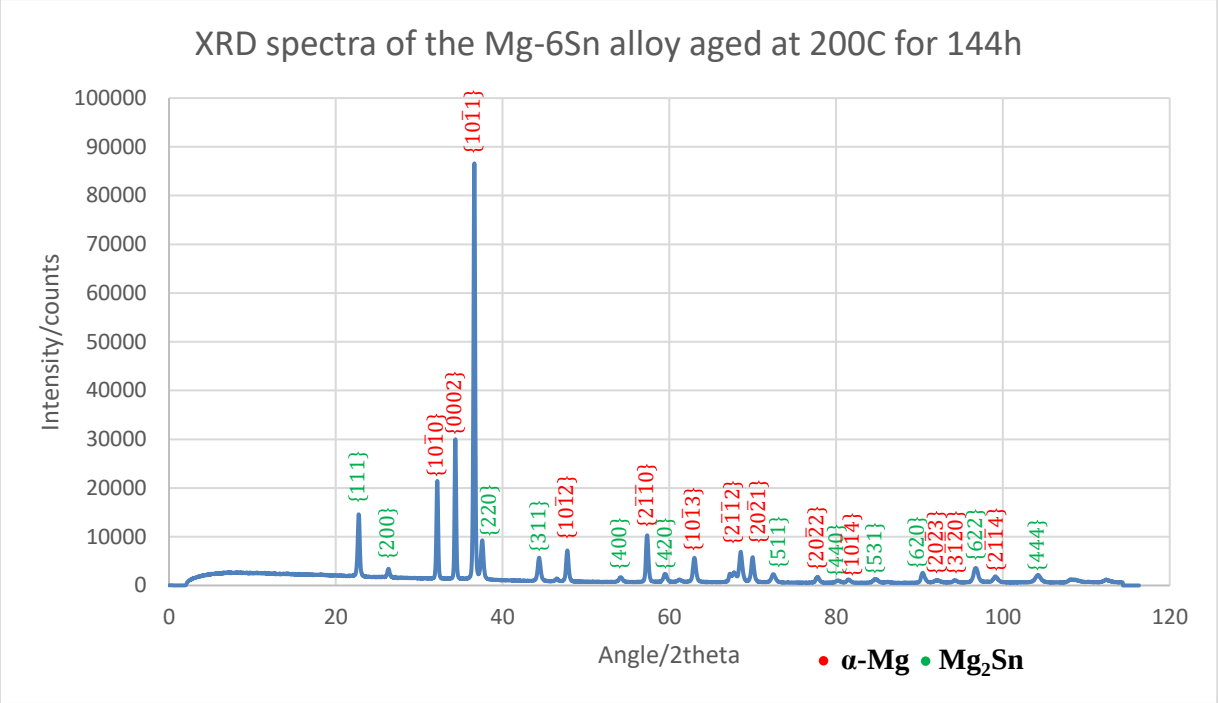


Figure 21 XRD spectra of the peak aged Mg-6Sn binary alloy

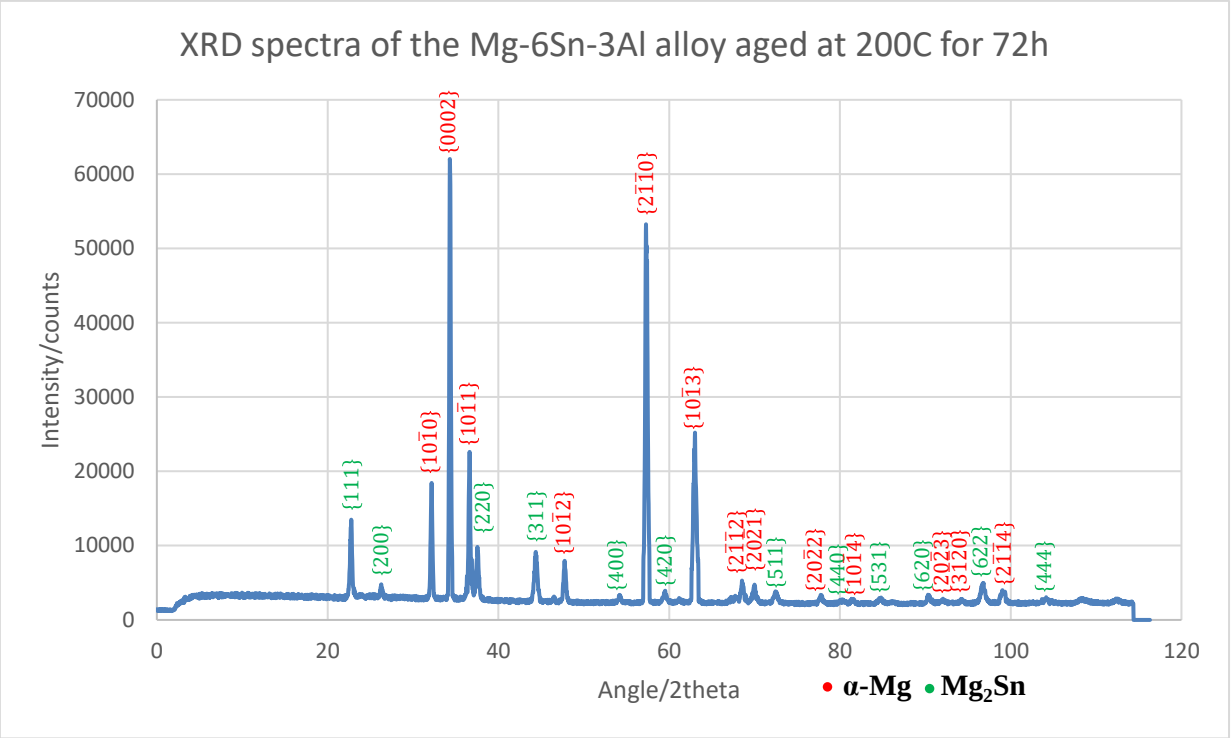


Figure 22 XRD spectra of the peak aged Mg-6Sn-3Al ternary alloy

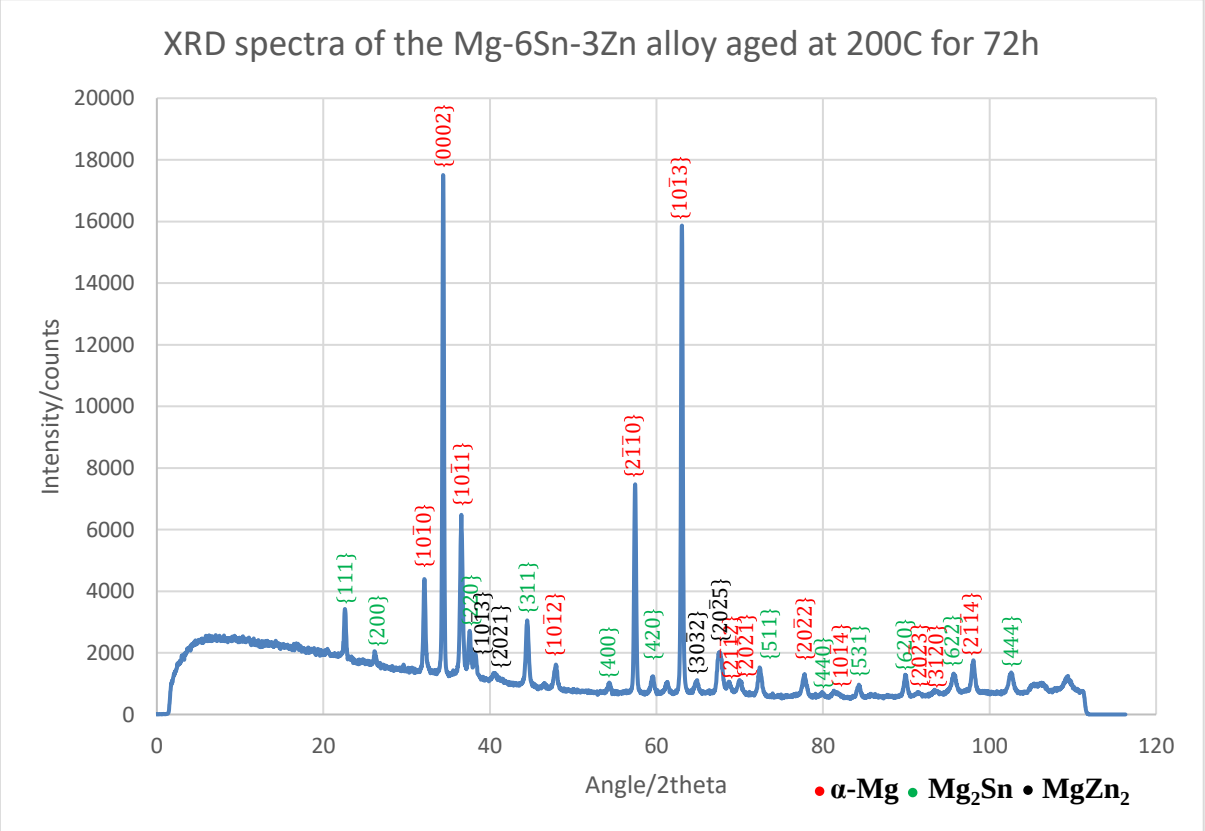


Figure 23 XRD spectra of the peak aged Mg-6Sn-3Zn ternary alloy

Comparing Figure 21, Figure 22 and Figure 23, it can be found that the intensities of some XRD reflections are not consistent between the different samples. This is due to a difference in the grain orientation of the different samples. The XRD spectra confirmed the following phases:

Binary Mg-6Sn: α-Mg+Mg_2Sn

Ternary Mg-6Sn-3Al: α-Mg+Mg_2Sn

Ternary Mg-6Sn-3Zn: α-Mg+Mg_2Sn+$MgZn_2$

The phases were then confirmed by STEM-EDS. Several spectra were collected from the precipitates. Each spectra is contributed by both the precipitate and the matrix. In order to separate out these two contributions, the composite results, each involving a different contribution from the (unwanted) matrix, were plotted on a normal diagram. A regression line can then be established via linear regression analysis which can be extrapolated to the atomic ratios for the precipitates. For example, a determination of the chemical compositions of the precipitates was performed on the Mg-6Sn-3Zn alloy. The matrix will contain both Sn and Zn in solid solution. The Mg-Sn precipitates, however, will be effectively Zn-free and the Mg-Zn precipitates Sn-free according to the ternary phase diagram[75]–[77]. Thus, by extending the regression line to the Zn-free and Sn-free sides, the exact compositions of the precipitates can be accurately determined. For the Mg-Sn precipitates, the normal plot indicating the chemical composition is shown in Figure 24, where the X axis stands for Mg concentration from the spectra and the Y axis stands for the Zn concentration. The Zn-free crossing of the regression line on the X axis (marked by the black cross) leads to a chemical composition of ~62% Mg and ~38% Sn which is close to 2:1. Therefore, the Mg-Sn precipitate in the alloy can be confirmed as being Mg_2Sn. The slope of the regression line, 0.0343, indicates the ratio of Mg/Zn in the matrix and is close to 3.3%. This value is higher than expected and may indicate

a Zn segregation near the Mg_2Sn precipitates which is in agreement with what Liu *et al* has observed via high-resolution EDS mapping[57].

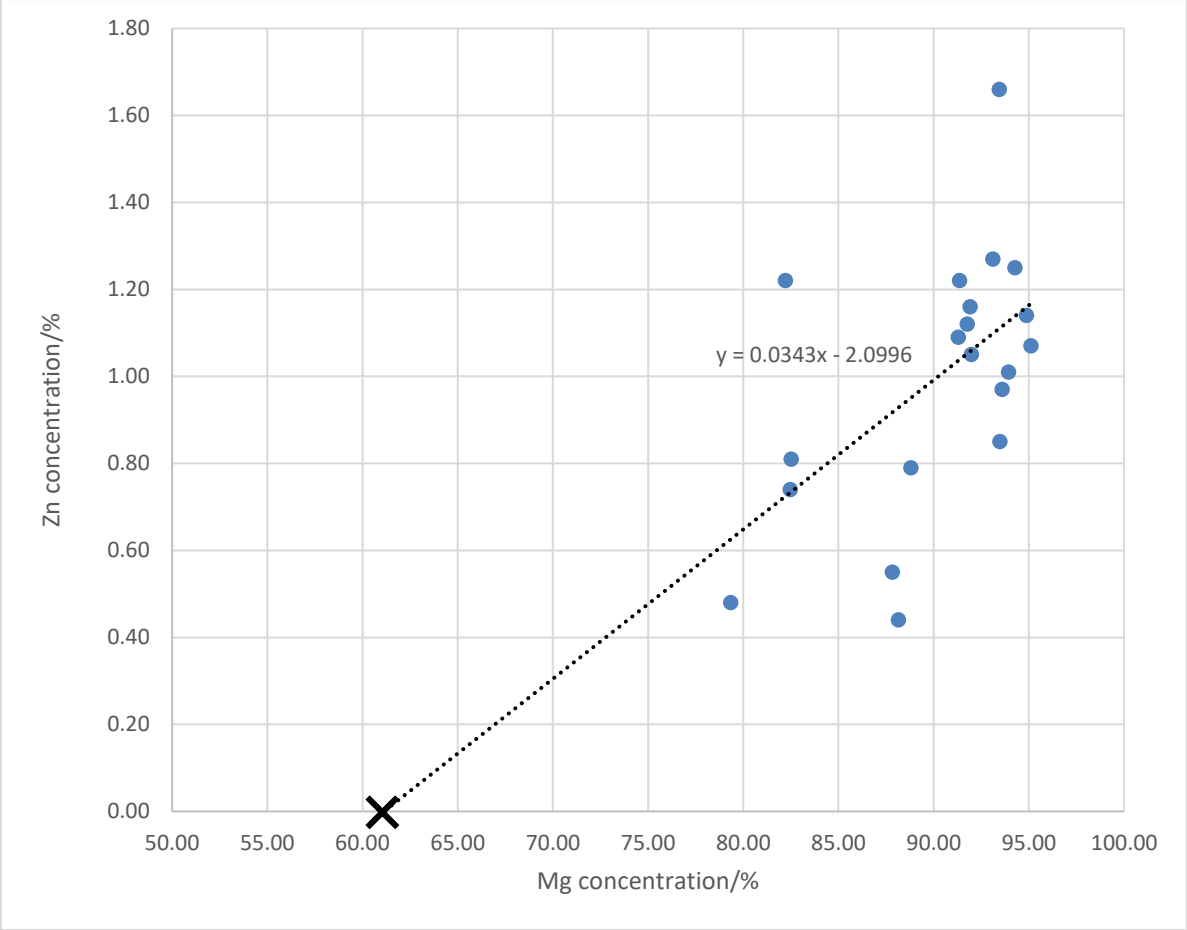


Figure 24 Normal plot establishing the chemical composition of the Mg-Sn precipitates, with all spectra marked as blue dots and the straight line coloured in black. The cross of the regression line on X axis has been marked with a cross.

For the Mg-Zn precipitates, the normal plot identifying their chemical composition is shown in Figure 25. The Sn-free crossing of the regression line on the X axis (marked by the black cross) leads to a chemical composition of ~37% Mg and ~63% Zn which is close to 1:2. Therefore, the Mg-Zn precipitate in the alloy can be confirmed as being $MgZn_2$. The slope of the regression line, 0.0085, indicates the ratio of Mg/Sn in the matrix and is close to 0.8%.

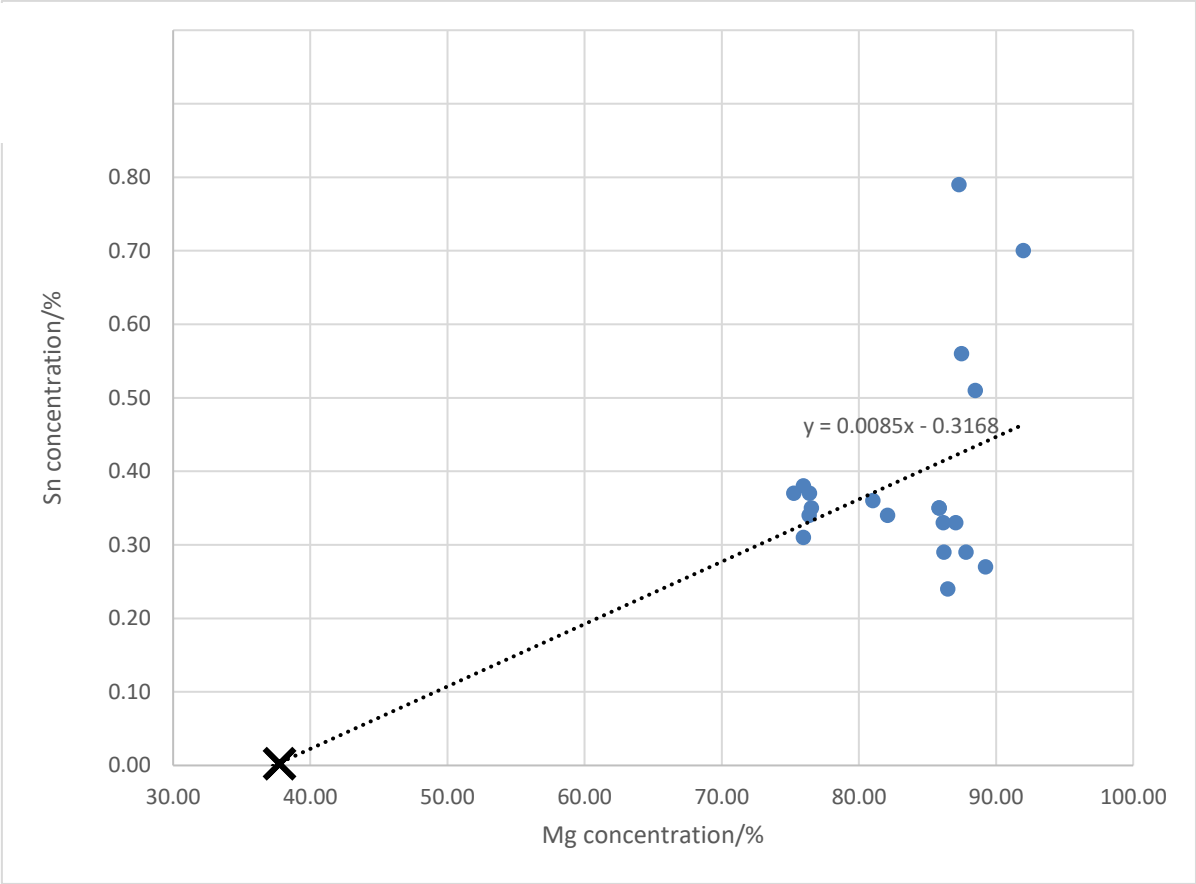


Figure 25 Normal plot establishing the chemical composition of the Mg-Zn precipitates, with all spectra marked in blue dots and the straight line coloured in black. The cross of the regression line on X axis has been marked with a cross.

5.4.1 Morphology and crystallography of precipitates in Mg-6Sn

In general, two types of Mg_2Sn precipitate were found in the peak aged Mg-6Sn binary alloy. A general STEM-HAADF image of the microstructure of the alloy is presented in Figure 26. As can be seen from the image, the peak aged binary alloy is dominated by lath-shaped precipitates with a habit plane of $(0001)_{Mg}$ (basal plane). The basal laths with long axis along the $\langle 11\bar{2}0\rangle_{Mg}$ directions are named Type 1 precipitates while the basal laths with long axis along the $\langle 10\bar{1}0\rangle_{Mg}$ directions are named Type 2 precipitates. Both types of precipitate are marked by arrows in Figure 26.

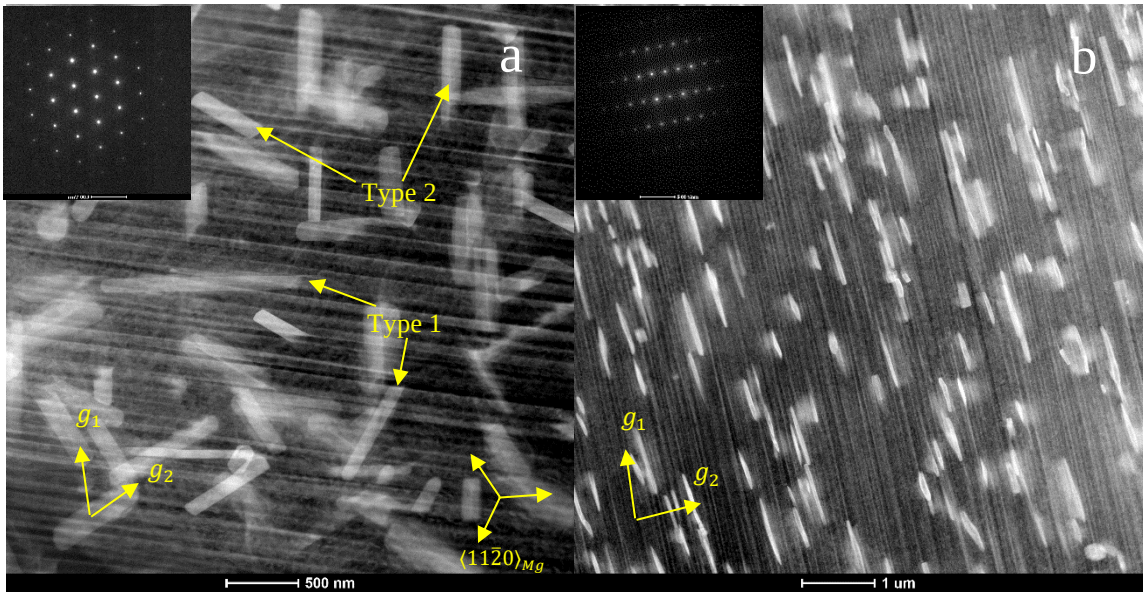


Figure 26 STEM-HAADF image showing the general microstructure of the peak aged Mg-6Sn binary alloy, (a) B ≈ $[0001]_{Mg}, g_1 = 10\bar{1}0_{Mg}, g_2 = 01\bar{1}0_{Mg}$, (b) B ≈ $[11\bar{2}0]_{Mg}, g_1 = 10\bar{1}0_{Mg}, g_2 = 0002_{Mg}$

5.4.1.1 Type 1 basal laths with long axis parallel to $\langle 11\bar{2}0\rangle_{Mg}$ directions

A STEM-HAADF image showing the exact morphology of a Type 1 precipitate can be found in Figure 27. Type 1 laths tend to have round tips and an aspect ratio of normally around 10:1. A selected area diffraction pattern indicating the OR between the Type 1 precipitates and the Mg matrix is shown in Figure 28. The diffraction pattern is contributed by both the Mg-matrix and the precipitate. The diffraction pattern from the Mg-matrix can be indexed as the $[0001]_{Mg}$ zone axis, while that from the FCC structured Mg_2Sn can be indexed as the $[110]_{Mg2Sn}$ zone axis. The rest of the diffraction pattern is contributed by double diffraction. As can be seen from the diffraction pattern, $g11\bar{2}0_{Mg} \parallel g002_{Mg2Sn}$, $g1\bar{1}00_{Mg} \parallel g2\bar{2}0_{Mg2Sn}$. Therefore, the OR between the Mg-matrix and the Type 1 precipitates is determined to be $(0001)_{Mg} \parallel (110)_{Mg2Sn}, [11\bar{2}0]_{Mg} \parallel [001]_{Mg2Sn}$. This OR

is equivalent to the OR1 first reported by Henes & Gerold and also in some other studies[8], [52], [59].

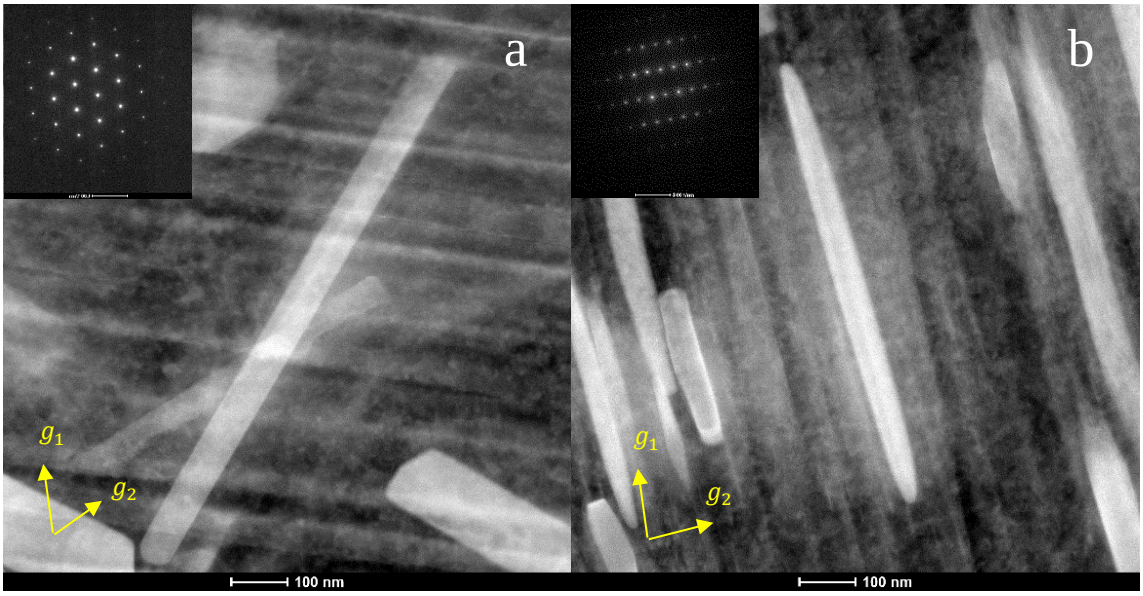


Figure 27 STEM-HAADF image showing the morphology of a Type 1 basal lath, (a) B ≈ $[0001]_{Mg}, g_1 = 10\bar{1}0_{Mg}, g_2 = 01\bar{1}0_{Mg}$, (b) B ≈ $[11\bar{2}0]_{Mg}, g_1 = 1\bar{1}00_{Mg}, g_2 = 0002_{Mg}$

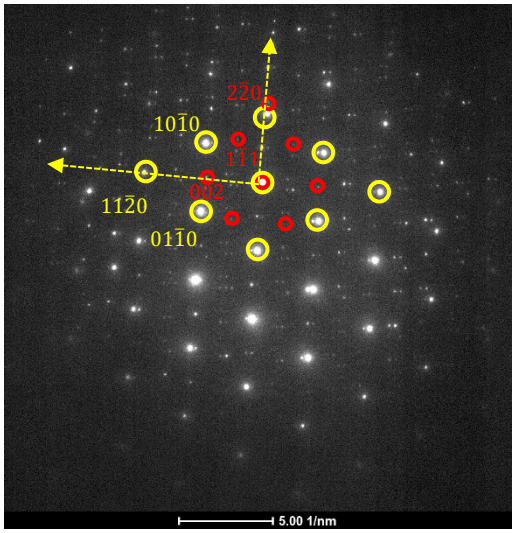


Figure 28 Selected area diffraction pattern determining the OR between a Type 1 precipitate and the Mg matrix. Reflections from the $[0001]_{Mg}$ zone axis are marked with yellow circles, reflections from the $[110]_{Mg2Sn}$ zone axis are marked with red circles. The OR given by the diffraction pattern is $(0001)_{Mg} \parallel (110)_{Mg2Sn}, [11\bar{2}0]_{Mg} \parallel [001]_{Mg2Sn}$.

5.4.1.2 Type 2 basal laths with long axis parallel to $\langle 10\bar{1}0\rangle_{Mg}$ directions

Another type of precipitate found in the peak-aged Mg-6Sn binary alloys is a basal lath which has its long axis parallel to the $\langle 10\bar{1}0\rangle_{Mg}$ directions and which will be called Type 2. The morphology of the Type 2 precipitates is shown in a STEM-HAADF image in Figure 29. Compared with the Type 1 precipitates, the Type 2 precipitates tend to have a smaller aspect ratio, around 5:1. In addition, differently from the round tips of the Type 1 precipitates, Type 2 precipitates exhibit three obvious facets which are marked by arrows in Figure 29(a). One of the facets is parallel to $\{11\bar{2}0\}_{Mg}$ (F1) while the other two facets are parallel to $\{10\bar{1}0\}_{Mg}$ (F2 and F3).

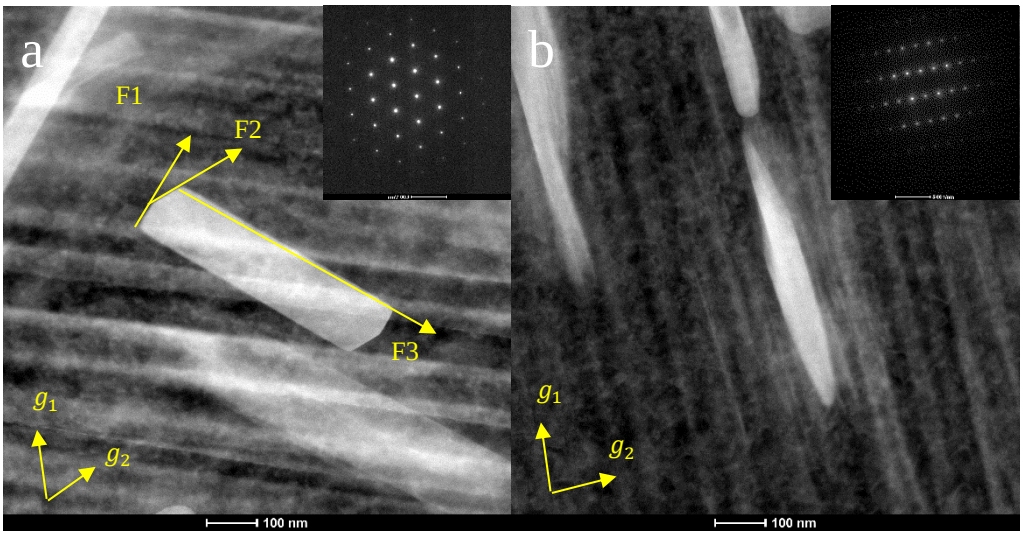


Figure 29 STEM-HAADF image showing the morphology of a Type 2 basal lath, (a) B ≈ $[0001]_{Mg}, g_1 = 10\bar{1}0_{Mg}, g_2 = 01\bar{1}0_{Mg}$, (b) B ≈ $[11\bar{2}0]_{Mg}, g_1 = 1\bar{1}00_{Mg}, g_2 = 0002_{Mg}$

A selected area diffraction showing the OR between the Type 2 precipitates and the Mg-matrix can be found in Figure 30. The diffraction pattern is contributed to by both the Mg-matrix and the precipitate. The diffraction pattern from the Mg-matrix can be indexed as the $[0001]_{Mg}$ zone axis, while that from the Mg_2Sn can be indexed as the $[110]_{Mg2Sn}$ zone axis. The rest of the diffraction pattern is contributed by double diffraction; for example, forbidden

reflections such as $g1\bar{1}\bar{2}_{Mg2Sn}$ and $g001_{Mg2Sn}$ (marked by blue circles in Figure 30). As can be seen from the diffraction pattern, $g2\bar{1}\bar{1}0_{Mg} \parallel g1\bar{1}1_{Mg2Sn}$, $g01\bar{1}0_{Mg} \parallel g1\bar{1}\bar{2}_{Mg2Sn}$. Therefore, the OR between the Mg-matrix and the Type 2 precipitates can be determined as $(0001)_{Mg} \parallel (110)_{Mg2Sn}, [2\bar{1}\bar{1}0]_{Mg} \parallel [1\bar{1}1]_{Mg2Sn}$. This OR is equivalent to the OR2 first reported by Henes & Gerold and also reported in some other studies[6], [8], [49].

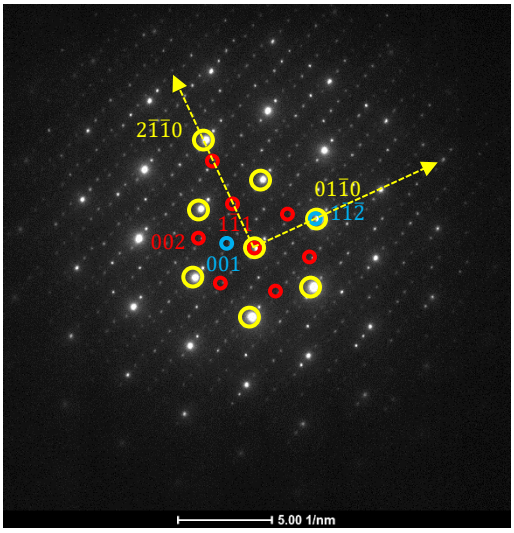


Figure 30 Selected area diffraction pattern defining the OR between the Type 2 precipitates and the Mg matrix. Reflections from the $[0001]_{Mg}$ zone axis are marked with yellow circles, reflections from the $[110]_{Mg2Sn}$ zone axis are marked with red circles, a few forbidden reflections from the $[110]_{Mg2Sn}$ zone axis are marked with blue circles. The OR given by the diffraction pattern is $(0001)_{Mg} \parallel (110)_{Mg2Sn}, [2\bar{1}\bar{1}0]_{Mg} \parallel [1\bar{1}1]_{Mg2Sn}$.

5.4.2 Morphology and crystallography of precipitates in Mg-6Sn-3Al ternary alloy

With the addition of 3% Al to the binary alloy, the precipitate distribution becomes more complex. STEM-HAADF images showing the microstructure of the Mg-6Sn-3Al alloy are shown below in Figure 31, with a magnified image in Figure 32 showing the exact

morphology of the precipitates. The addition of Al leads to there being one type of basal rods in the alloy, which will be called Type 3, accompanied by additional basal plates, c-axis rods and pyramidal laths, labelled Type 4, Type 5 and Type 6 respectively. The details of the precipitates are as follows.

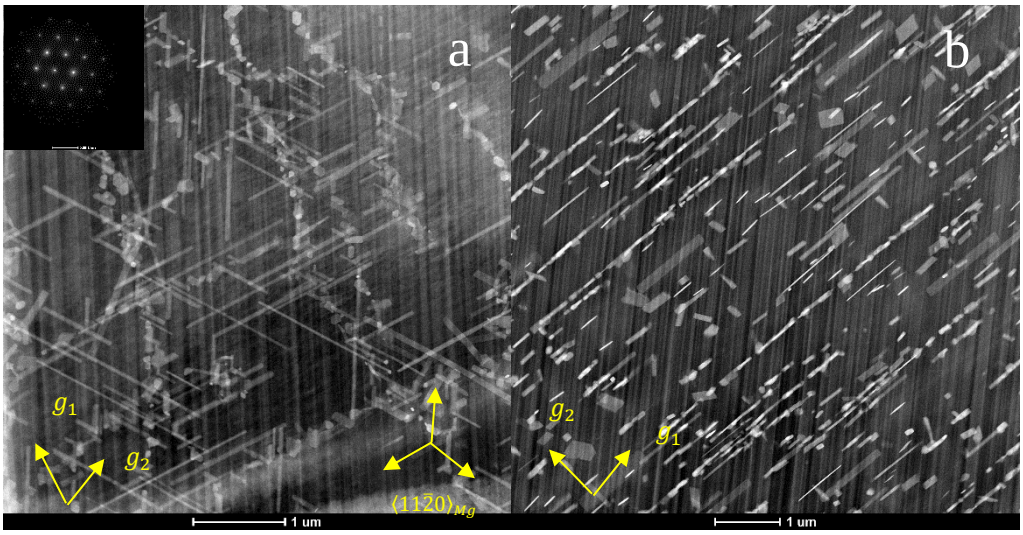


Figure 31 STEM-HAADF image showing the microstructure of the peak aged (72h) Mg-6Sn-3Al alloy, (a) B $\approx [0001]_{Mg}, g_1 = 10\bar{1}0_{Mg}, g_2 = 01\bar{1}0_{Mg}$, (b) B $\approx [1\bar{1}00]_{Mg}, g_1 = 11\bar{2}0_{Mg}, g_2 = 0002_{Mg}$

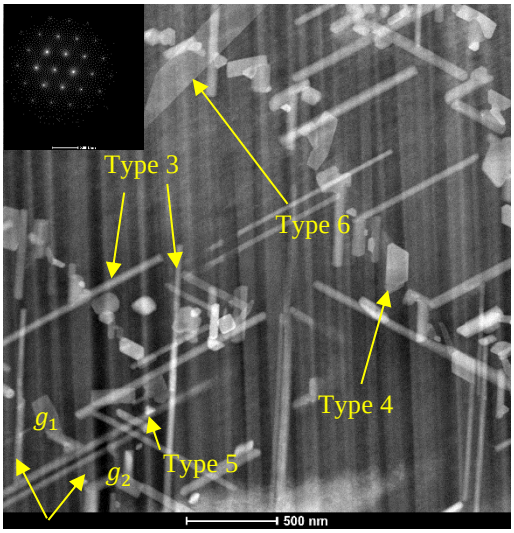


Figure 32 A higher magnification STEM-HAADF image of the peak aged Mg-6Sn-3Al alloy showing the different types of precipitates. B $\approx [0001]_{Mg}, g_1 = 10\bar{1}0_{Mg}, g_2 = 01\bar{1}0_{Mg}$

5.4.2.1 Type 3 basal rods with long axis parallel to the $\langle 11\bar{2}0\rangle_{Mg}$ directions

The addition of Al has caused a rod-shaped basal precipitate to occur. These Type 3 basal Mg_2Sn rods have their long axis parallel to the $\langle 11\bar{2}0\rangle_{Mg}$ directions. A magnified image showing the exact morphology of a Type 3 precipitate can be found in Figure 33. Type 3 precipitates normally have a high aspect ratio, around 25:1 with a rectangular cross-section. Some of the Type 3 precipitates have their tips slightly faceted (as marked in Figure 33(a). F1 is parallel to $\{11\bar{2}0\}_{Mg}$ and F2 is parallel to $\{10\bar{1}0\}_{Mg}$) but most of them tend to have round tips.

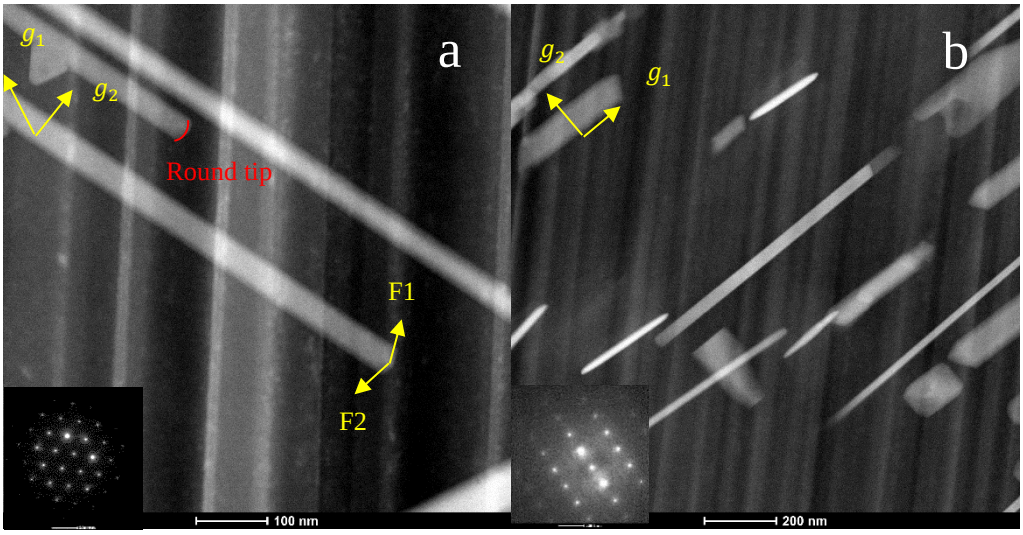


Figure 33 STEM-HAADF image showing the exact morphology of the Type 3 Mg_2Sn precipitates. (a) B $\approx [0001]_{Mg}, g_1 = 10\bar{1}0_{Mg}, g_2 = 01\bar{1}0_{Mg}$, (b) B $\approx [1\bar{1}00]_{Mg}, g_1 = 11\bar{2}0_{Mg}, g_2 = 0002_{Mg}$.

A selected area diffraction showing the OR between the Type 3 precipitates and the Mg-matrix can be found in Figure 34. The diffraction pattern is contributed to by both the Mg-matrix and the precipitate. The diffraction pattern from the Mg-matrix can be indexed as the $[0001]_{Mg}$ zone axis, while that from the Mg_2Sn can be indexed as the $[111]_{Mg2Sn}$ zone axis. The rest of the diffraction pattern is caused by double diffraction, for example forbidden reflections such as $g1\bar{1}0_{Mg2Sn}$ and $g1\bar{2}1_{Mg2Sn}$ (marked by blue circles in Figure 34). The diffraction pattern shows a series of parallel reflections such as $g11\bar{2}0_{Mg} \parallel g1\bar{1}0_{Mg2Sn}$, $g10\bar{1}0_{Mg} \parallel g1\bar{2}1_{Mg2Sn}$. Therefore, the OR between the Mg-matrix and the Type 3 precipitates can be determined as $(0001)_{Mg} \parallel (111)_{Mg2Sn}, [11\bar{2}0]_{Mg} \parallel [1\bar{1}0]_{Mg2Sn}$. First determined by Henes & Gerold as OR4, this OR is one of the most commonly reported ORs between the Mg matrix and a Mg_2Sn precipitate [5], [7], [8], [49], [52], [54].

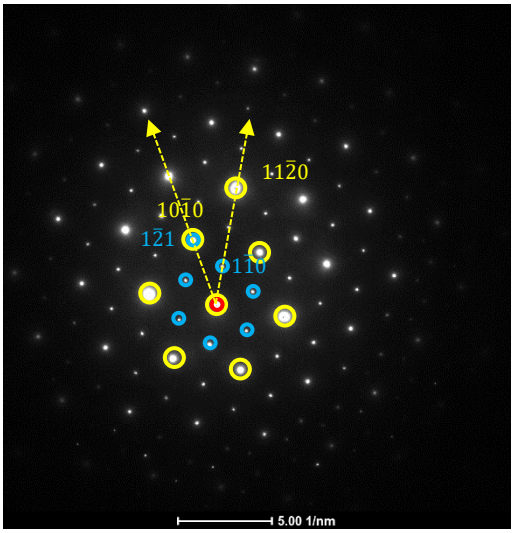


Figure 34 Selected area diffraction pattern defining the OR between the Type 3 precipitates and the Mg matrix. Reflections from the $[0001]_{Mg}$ zone axis are marked with yellow circles, forbidden reflections from the $[111]_{Mg2Sn}$ zone axis are marked with blue circles. The OR given by the diffraction pattern is $(0001)_{Mg} \parallel (111)_{Mg2Sn}, [11\bar{2}0]_{Mg} \parallel [1\bar{1}0]_{Mg2Sn}$

5.4.2.2 Type 4 hexagonal basal plates

The addition of Al also caused basal Mg_2Sn plates to appear in the alloy. These plate-shaped precipitates inhabit the basal plane and will be called Type 4 basal plates. The morphology of this type of precipitate is demonstrated in Figure 35. Type 4 basal plates are obviously faceted with their 3 sets of facets parallel to $\{11\bar{2}0\}_{Mg}$, as marked in the figure below.

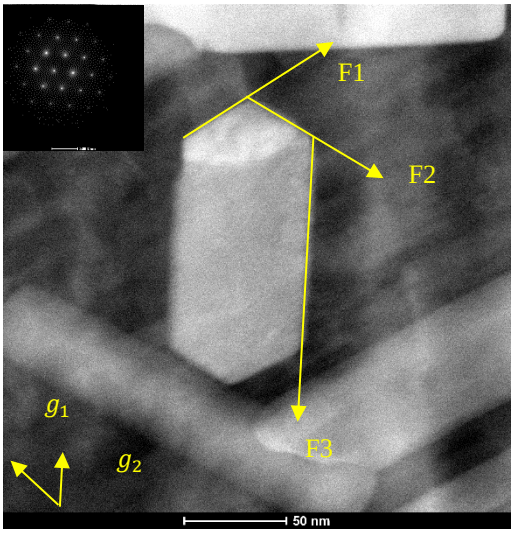


Figure 35 STEM-HAADF micrographs showing the morphology of the Type 4 basal plates, $B \approx [0001]_{Mg}, g_1 = 11\bar{2}0_{Mg}, g_2 = 1\bar{2}10_{Mg}$

A selected area diffraction pattern from the Type 4 basal plate is shown below in Figure 36. The diffraction pattern is identical to those from precipitate Type 3. With $g11\bar{2}0_{Mg} \parallel g1\bar{1}0_{Mg2Sn}$, $g10\bar{1}0_{Mg} \parallel g1\bar{2}1_{Mg2Sn}$, the OR between the Type 4 precipitates and the Mg matrix is $(0001)_{Mg} \parallel (111)_{Mg2Sn}, [11\bar{2}0]_{Mg} \parallel [1\bar{1}0]_{Mg2Sn}$, namely OR4.

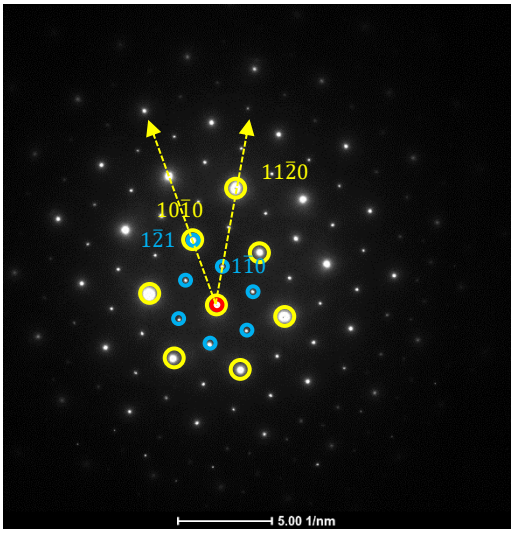


Figure 36 Selected area diffraction pattern from a Type 4 basal plate showing OR4. Reflections from the $[0001]_{Mg}$ zone axis are marked with yellow circles, forbidden

reflections from the $[111]_{Mg2Sn}$ zone axis are marked with blue circles. The OR given by the diffraction pattern is $(0001)_{Mg} \parallel (111)_{Mg2Sn}, [11\bar{2}0]_{Mg} \parallel [1\bar{1}0]_{Mg2Sn}$

5.4.2.3 Type 5 c-axis rods with long axis along the $[0001]_{Mg}$ direction

When observed from the $[0001]_{Mg}$ direction, these precipitates exhibit a triangular cross-section, with the three facets parallel to $\{11\bar{2}0\}_{Mg}$. The long axis is parallel to $[0001]_{Mg}$. This precipitate type is categorized as Type 5 c-axis rods. A STEM-HAADF image showing their exact morphology can be found in Figure 37.

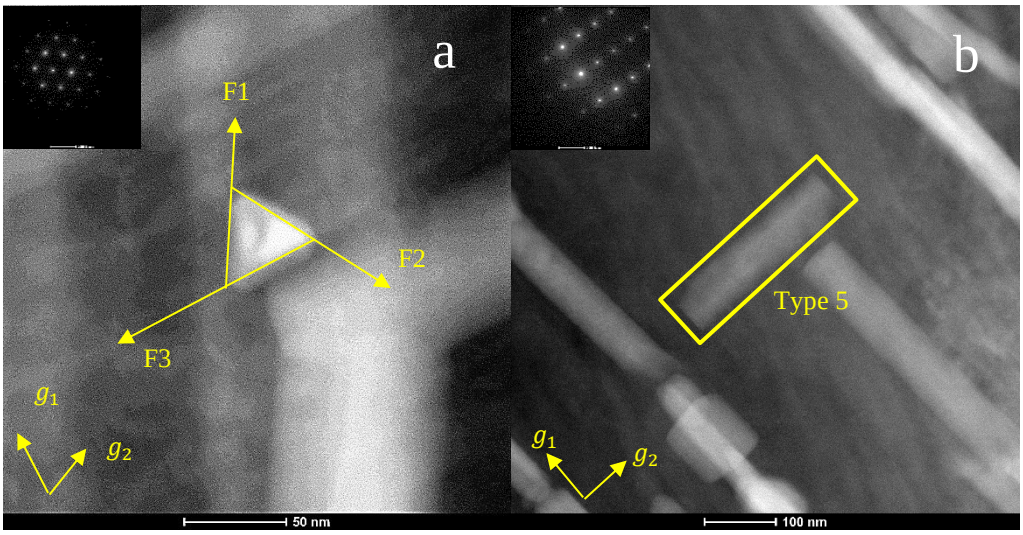


Figure 37 STEM-HAADF images showing the exact morphology of the Type 5 c-axis rods, (a) B $\approx [0001]_{Mg}, g_1 = 10\bar{1}0_{Mg}, g_2 = 01\bar{1}0_{Mg}$, (b) B $\approx [1\bar{1}00]_{Mg}, g_1 = 11\bar{2}0_{Mg}, g_2 = 0002_{Mg}$.

A selected area diffraction pattern acquired from the precipitate is shown below in Figure 38. With $g11\bar{2}0_{Mg} \parallel g1\bar{1}0_{Mg2Sn}$, $g10\bar{1}0_{Mg} \parallel g1\bar{2}1_{Mg2Sn}$, the OR between the Type 5 c-axis rods and the Mg matrix is $(0001)_{Mg} \parallel (111)_{Mg2Sn}, [11\bar{2}0]_{Mg} \parallel [1\bar{1}0]_{Mg2Sn}$, i.e. OR4.

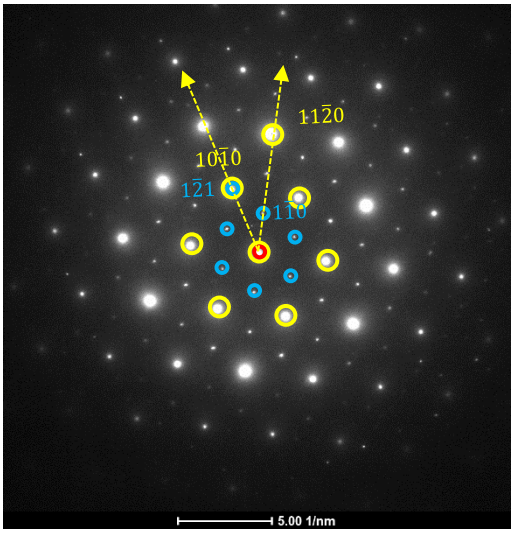


Figure 38 Selected area diffraction pattern demonstrating ORs between the Type 5 c-axis rods and the Mg matrix. Reflections from the $[0001]_{Mg}$ zone axis are marked with yellow circles, forbidden reflections from the $[111]_{Mg2Sn}$ zone axis are marked with blue circles. The OR given by the diffraction pattern is $(0001)_{Mg} \parallel (111)_{Mg2Sn}$, $[11\bar{2}0]_{Mg} \parallel [1\bar{1}0]_{Mg2Sn}$

5.4.2.4 Type 6 pyramidal laths with long axis along $\langle 11\bar{2}0 \rangle_{Mg}$ directions

Pyramidal laths also were found in the Mg-6Sn-3Al alloy. These precipitates are categorised as Type 6 pyramidal laths. TEM tilting series have confirmed that these precipitates have a first order pyramidal habit plane. An example of a tilting series for two pyramidal laths is shown below in Figure 39. An image was taken every 15° of α-tilt.

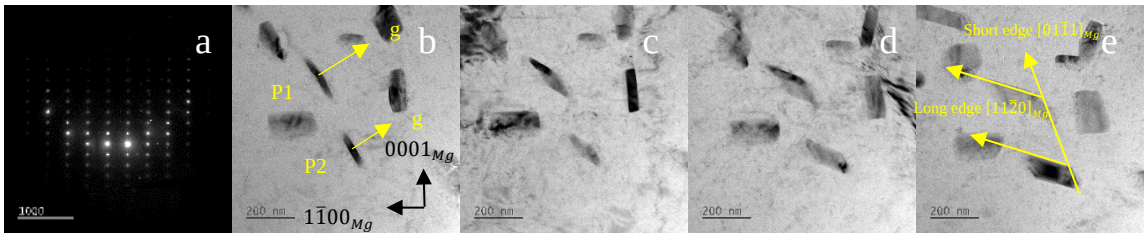


Figure 39 Tilting series for two pyramidal laths (a) Diffraction pattern showing the near-$[11\bar{2}0]_{Mg}$ beam direction at α~-15° tilt (b) α~-15°, both precipitates are edge-on, $B \approx$

$[11\bar{2}0]_{Mg}$, the g-vector defining the habit plane is $1\bar{1}01_{Mg}$ (c) α~0°, (d) α~15°, (e) α~30°, the long and short edges of the laths are marked in the figure

Thus, these precipitates lie on $(1\bar{1}01)_{Mg}$. The ORs for these pyramidal precipitates appear to be rather variable. For example, the diffraction patterns for P1 and P2 are shown below in Figure 40, where the reflections from Mg are marked yellow and those from Mg_2Sn are marked red. For P1, the orientation relationship with the Mg-matrix is $(11\bar{2}0)_{Mg} \parallel (110)_{Mg2Sn}, [1\bar{1}01]_{Mg} \parallel [1\bar{1}3]_{Mg2Sn}$ and that for P2 is $(11\bar{2}0)_{Mg} \parallel (110)_{Mg2Sn}, [1\bar{1}01]_{Mg} \parallel [1\bar{1}5]_{Mg2Sn}$. This variability is not currently understood.

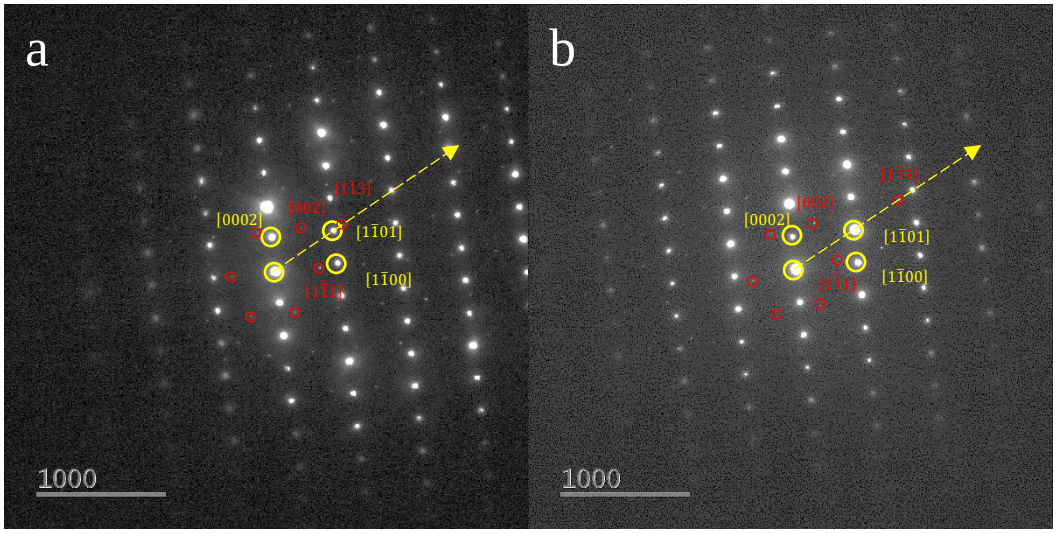


Figure 40 Diffraction patterns showing the OR between P1 (a), P2 (b) and the Mg-matrix. For P1, the OR given by the diffraction pattern is $(11\bar{2}0)_{Mg} \parallel (110)_{Mg2Sn}, [1\bar{1}01]_{Mg} \parallel [1\bar{1}3]_{Mg2Sn}$, for P2, the OR given by the diffraction pattern is $(11\bar{2}0)_{Mg} \parallel (110)_{Mg2Sn}, [1\bar{1}01]_{Mg} \parallel [1\bar{1}5]_{Mg2Sn}$. Note that the diffraction pattern is slightly rotated by the rotational TEM holder for better imaging quality

Some existing research also reported the habit planes of pyramidal Mg_2Sn precipitates in Mg alloys. Sasaki *et al*. reported pyramidal laths with $\{11\bar{2}2\}_{Mg}$ habit planes and $\langle 10\bar{1}0\rangle_{Mg}$

long axes without specifying the orientation relationship[78]. But no other research either confirms or denies this. Some habit planes and orientation relationships occur more frequently.

5.4.2.5 Basal plate clusters

There also appear clusters of basal Mg_2Sn plates in the Mg-6Sn-3Al alloy. When observed along $[0001]_{Mg}$, these precipitates exhibit different shapes and are normally concentrated in one particular area. Observations along $[10\bar{1}0]_{Mg}$ show that these precipitates, although exhibiting quite various morphologies, are plate-shaped precipitates on the basal plane. STEM-HAADF images of these clusters can be found in Figure 41.

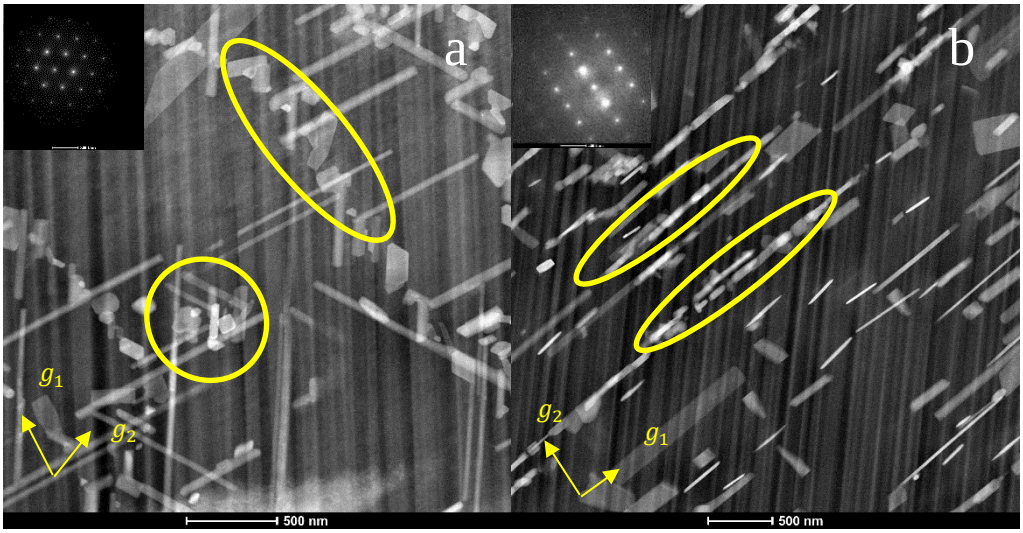


Figure 41 STEM-HAADF images showing the exact morphology of the clustered basal precipitates. (a) B $\approx [0001]_{Mg}, g_1 = 10\bar{1}0_{Mg}, g_2 = 01\bar{1}0_{Mg}$, (b) B $\approx [10\bar{1}0]_{Mg}, g_1 = 11\bar{2}0_{Mg}, g_2 = 0002_{Mg}$

Interestingly, although the clustered precipitates vary in shape and size, they still exhibit a few facets parallel to the low index directions in the $(0001)_{Mg}$ plane. However, they are not as faceted as the Type 4 basal plates. A series of images showing these facets is shown below in Figure 42.

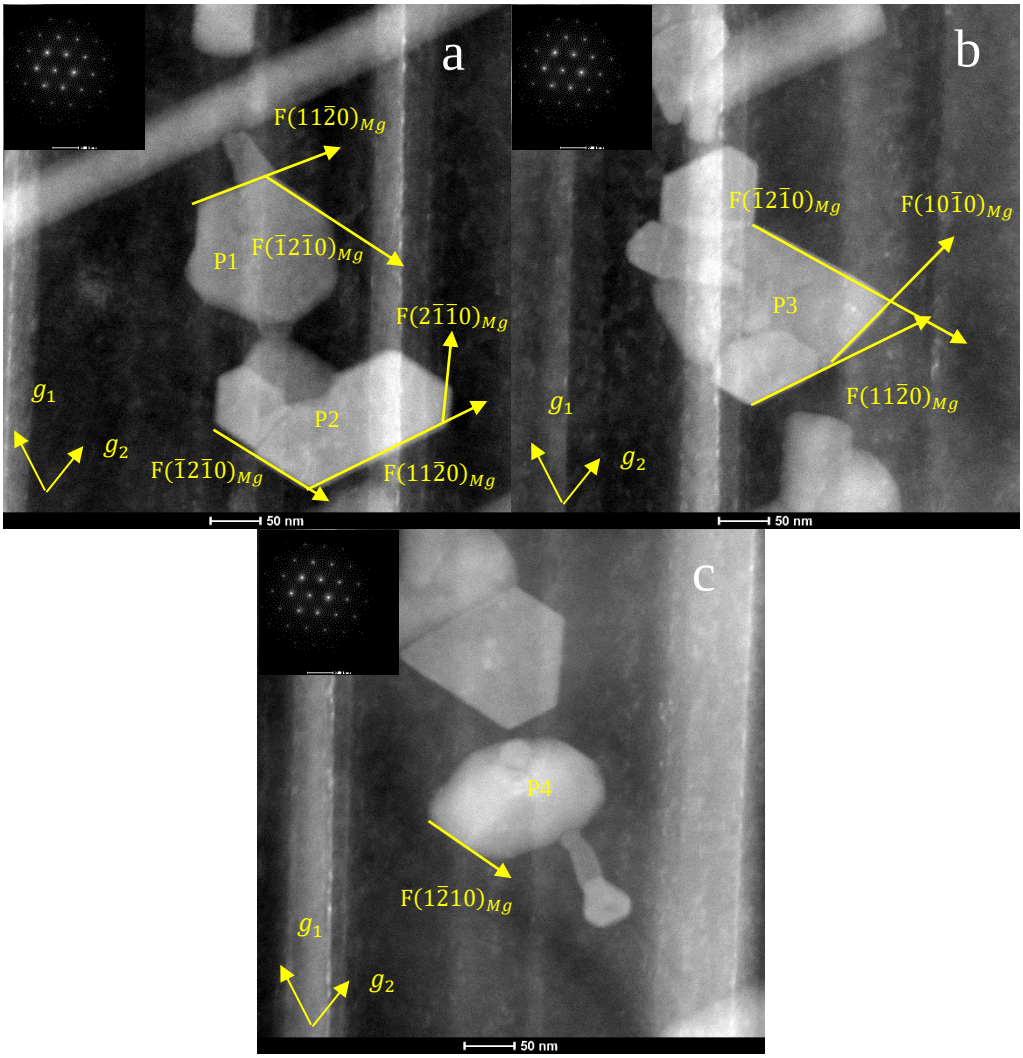


Figure 42 STEM-HAADF images showing facets of the clustered precipitates. B ≈ $[0001]_{Mg}, g_1 = 10\bar{1}0_{Mg}, g_2 = 01\bar{1}0_{Mg}$

Some selected area diffraction patterns were taken from the clustered precipitates with B = $[0001]_{Mg}$ to identify their OR with the Mg-matrix. Four diffraction patterns from four precipitates P1, P2, P3 and P4 are shown below as Figure 43 (a), (b), (c) and (d). All four precipitates exhibit the same OR as the Type 3, 4 and 5 precipitates, with $g11\bar{2}0_{Mg} \parallel g1\bar{1}0_{Mg2Sn}$, $g10\bar{1}0_{Mg} \parallel g1\bar{2}1_{Mg2Sn}$. Thus $(0001)_{Mg} \parallel (111)_{Mg2Sn}, [11\bar{2}0]_{Mg} \parallel [1\bar{1}0]_{Mg2Sn}$, which is OR4 [8].

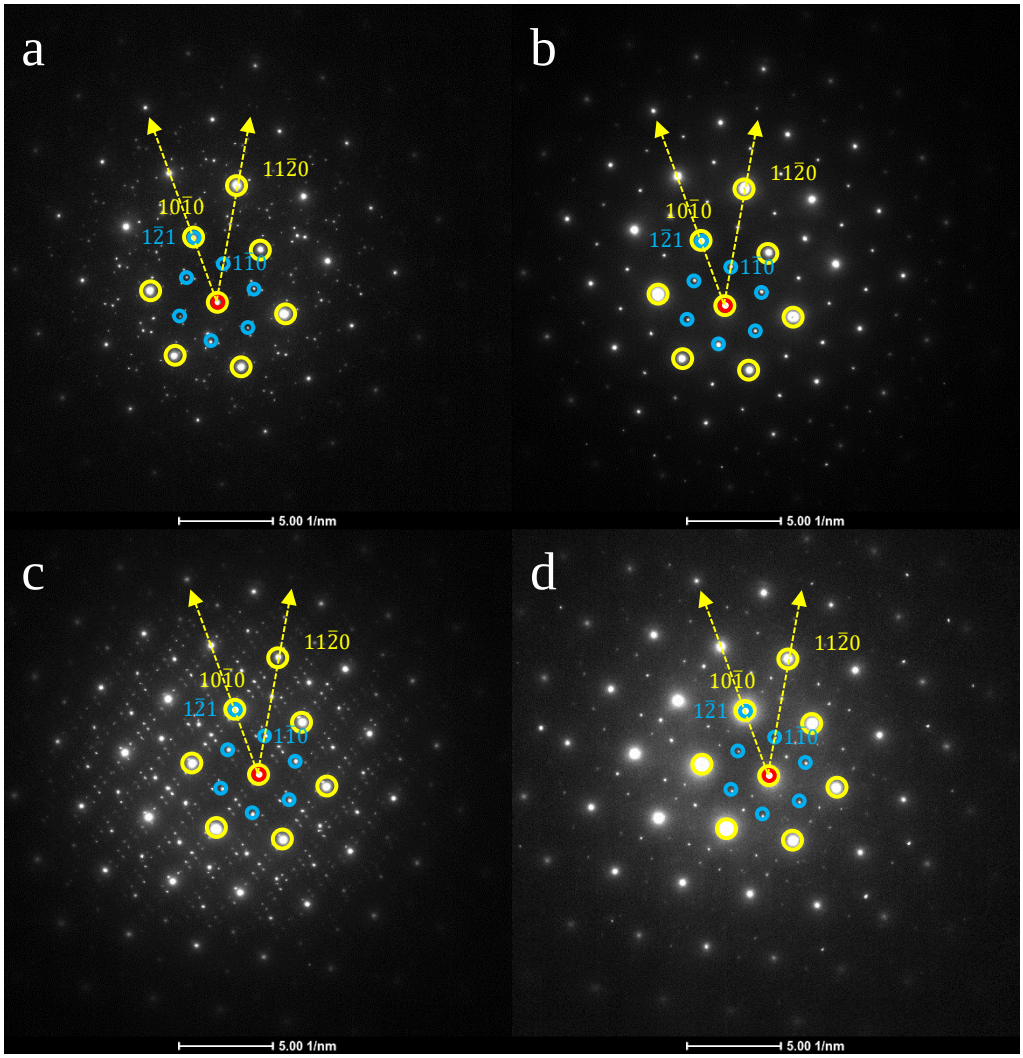


Figure 43 Selected area diffraction patterns from four of the clustered precipitates showing their ORs with the Mg-matrix. (a) P1, (b) P2, (c) P3, (d) P4. Reflections from the $[0001]_{Mg}$ zone axis are marked with yellow circles, forbidden reflections from the $[111]_{Mg2Sn}$ zone axis are marked with blue circles. The OR given by the diffraction patterns are all

$$(0001)_{Mg} \parallel (111)_{Mg2Sn}, [11\bar{2}0]_{Mg} \parallel [1\bar{1}0]_{Mg2Sn}$$

5.4.2.6 The distribution of Al in the Mg-6Sn-3Al alloy

As Al did not form its 'own' precipitates in the Mg-6Sn-3Al ternary alloy, EDS mapping was performed to determine the distribution of Al in the alloy and is shown below in Figure 44. The distribution of Mg, Sn and Al are shown in their respective maps. As can be seen

from the images, most of the Sn is concentrated in the Mg_2Sn precipitates, while a smaller amount remains in the Mg-matrix in a solid solution state. Al on the other hand, is homogeneously distributed in the matrix. A particle rich in Al has been marked by the white circle in Figure 44(d). This may be due to the presence of pre-existing crystallographic features favourable for the formation of Al-rich particle and is not a common case.

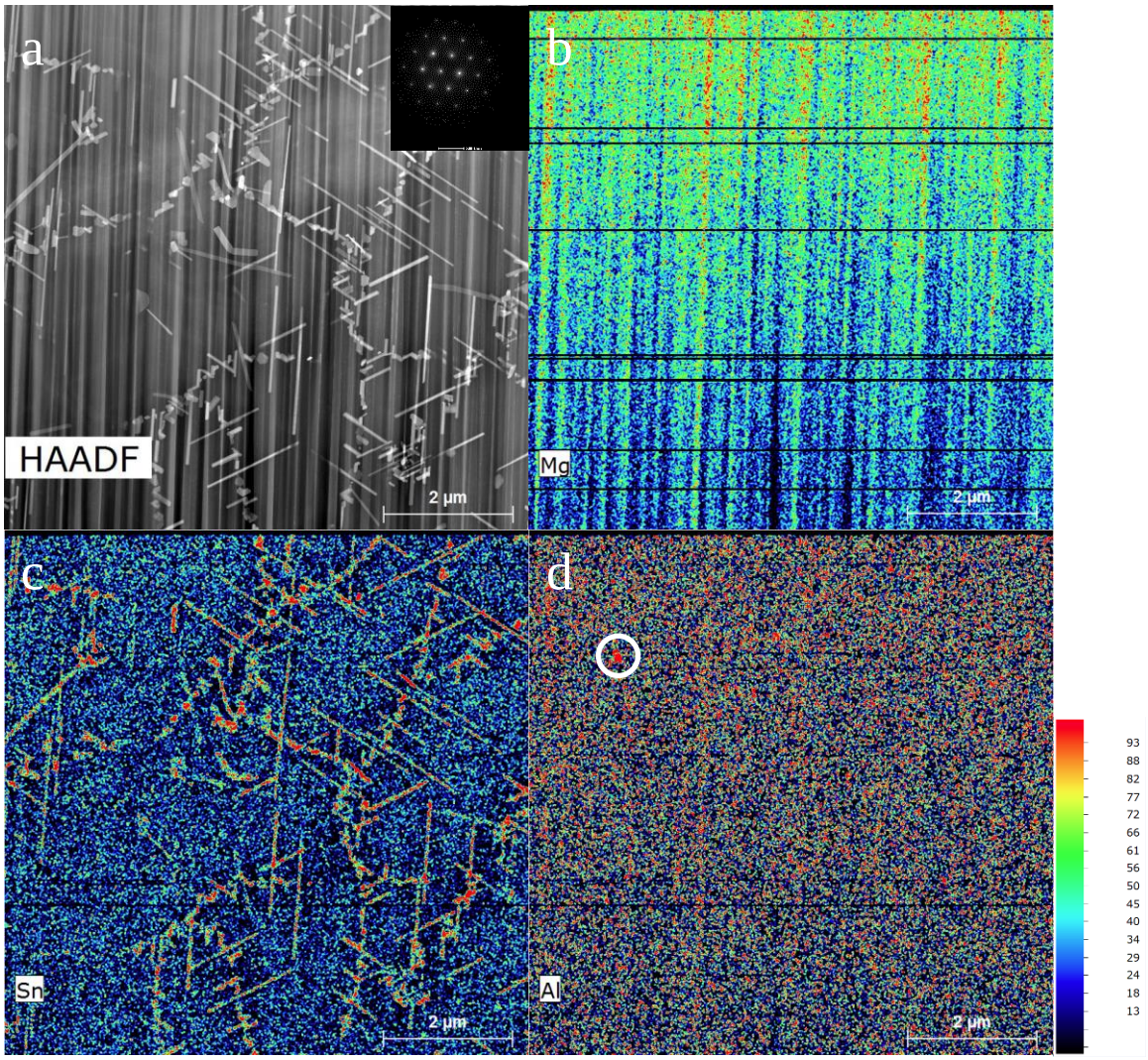


Figure 44 STEM-EDS maps showing the distribution of elements in the peak aged Mg-6Sn-3Al alloy, (a) STEM-HAADF image, (b) Mg distribution, (c) Sn distribution, (d) Al distribution, the white circle marks an Al-rich particle. The stripes on (a) and (b) are from the curtaining effect by FIB milling.

5.4.3 Morphology and crystallography of precipitates in Mg-6Sn-3Zn ternary alloy

The morphology and crystallography of the precipitates in the ternary Mg-6Sn-3Zn alloy are different from those in the other two alloys. Except for the presence of Type 2 basal laths, prismatic Mg_2Sn laths (Type 7) and c-axis $MgZn_2$ rods are also found in the alloy. In addition, most of the $MgZn_2$ rods and Type 2 basal laths are connected, forming a T-shaped morphology. A STEM-HAADF image showing the general microstructure of the peak aged Mg-6Sn-3Zn alloy appears in Figure 45, with all the precipitate types marked. The details of all precipitate types are explained below.

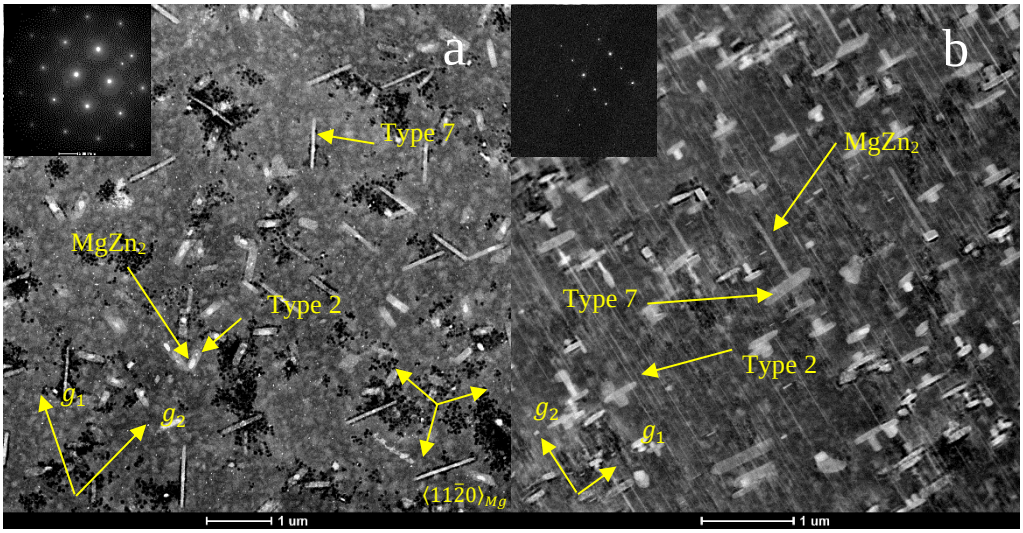


Figure 45 STEM-HAADF images showing the general microstructure of the precipitates in the peak aged Mg-6Sn-3Zn alloy, (a) B $\approx [0001]_{Mg}, g_1 = 10\bar{1}0_{Mg}, g_2 = 01\bar{1}0_{Mg}$, (b) B $\approx [1\bar{1}00]_{Mg}, g_1 = 11\bar{2}0_{Mg}, g_2 = 0002_{Mg}$.

5.4.3.1 Type 2 basal Mg_2Sn laths in the Mg-6Sn-3Zn alloy with long axis parallel to the $\langle 10\bar{1}0\rangle_{Mg}$ directions

Type 2 basal Mg_2Sn laths have been observed in the Mg-6Sn-3Zn alloy, but with a small difference from those in the binary Mg-6Sn alloy. Similarly to the Type 2 basal laths found in the binary Mg-6Sn alloy, they have their long axis parallel to the $\langle 10\bar{1}0\rangle_{Mg}$ directions and 3 facets parallel to $\{10\bar{1}0\}_{Mg}$. The difference is that most of the Type 2 basal laths are connected to a c-axis $MgZn_2$ rod, which is a commonly reported phenomenon in the Mg-Sn-Zn alloys. This will be enlarged on in a later section. STEM-HAADF images showing the exact morphology of the Type 2 basal lath are shown below in Figure 46, along with a magnified image (from Figure 46(a)) in Figure 47 marking all the facets of a Type 2 precipitate.

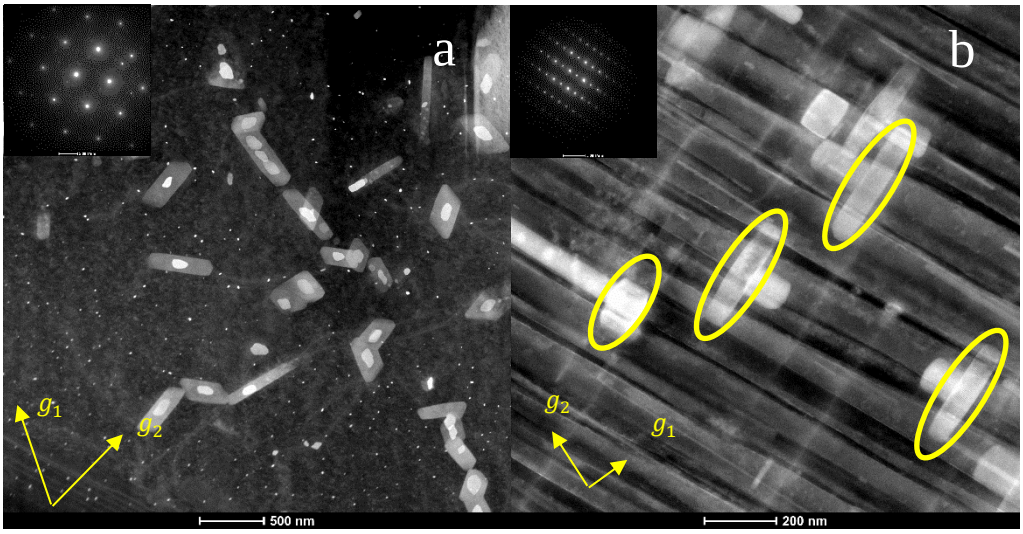


Figure 46 STEM-HAADF images showing the morphology of the Type 2 basal laths in the Mg-6Sn-3Zn ternary alloy. (a) B $\approx [0001]_{Mg}, g_1 = 10\bar{1}0_{Mg}, g_2 = 01\bar{1}0_{Mg}$, (b) B $\approx [11\bar{2}0]_{Mg}, g_1 = 1\bar{1}00_{Mg}, g_2 = 0002_{Mg}$. Type 2 laths are marked with yellow circles. The small bright dots in (a) are the $MgZn_2$ narrow laths.

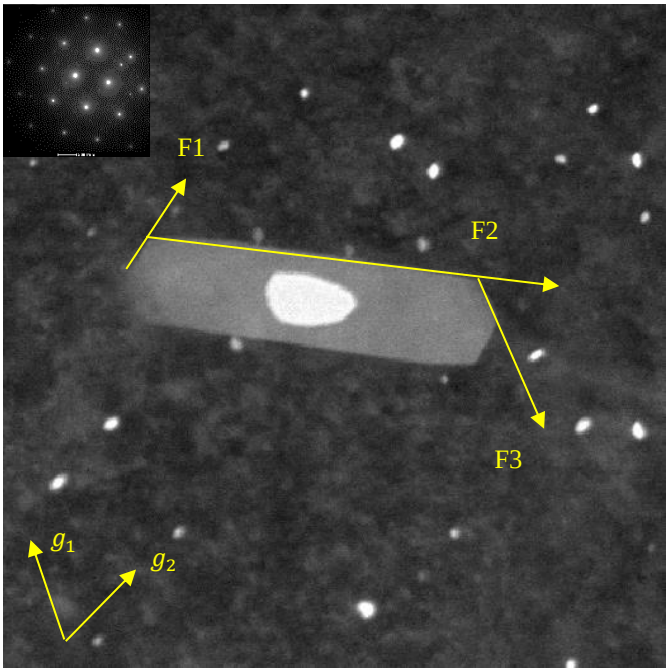


Figure 47 Magnified image of a Type 2 basal lath showing its three $\{10\bar{1}0\}_{Mg}$ facets. B ≈ $[0001]_{Mg}, g_1 = 10\bar{1}0_{Mg}, g_2 = 01\bar{1}0_{Mg}$. The bright shape within the precipitate is the connected $MgZn_2$ rod.

The Type 2 basal laths in the ternary Mg-6Sn-3Zn alloy exhibit the same OR as those in the binary alloy. A selected area diffraction pattern showing this appears in Figure 48. The diffraction pattern from the Mg-matrix can be indexed as the $[0001]_{Mg}$ zone axis, while that from the Mg_2Sn can be indexed as $[110]_{Mg2Sn}$. The rest of the diffraction pattern is contributed by double diffraction, hence the forbidden reflections such as $g1\bar{1}2_{Mg2Sn}$ and $g001_{Mg2Sn}$ were enabled (marked by blue circles in Figure 48). As can be seen from the diffraction pattern, $g2\bar{1}\bar{1}0_{Mg} \parallel g1\bar{1}1_{Mg2Sn}$, $g01\bar{1}0_{Mg} \parallel g1\bar{1}\bar{2}_{Mg2Sn}$. Therefore, the OR between the Mg-matrix and the Type 2 basal laths in the Mg-6Sn-3Zn ternary alloy can be determined as $(0001)_{Mg} \parallel (110)_{Mg2Sn}, [2\bar{1}\bar{1}0]_{Mg} \parallel [1\bar{1}1]_{Mg2Sn}$, namely OR2.

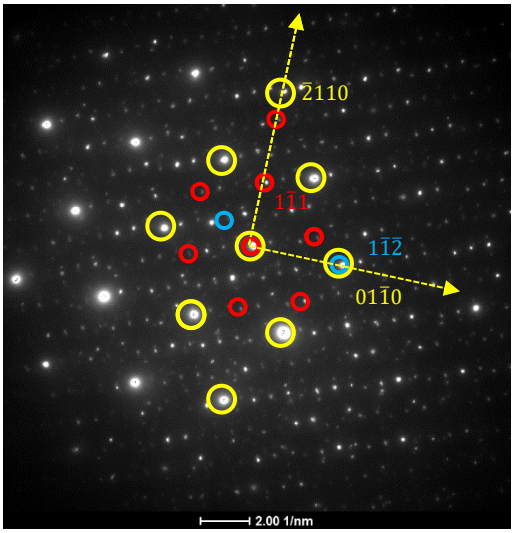


Figure 48 Selected area diffraction pattern showing the OR between the Type 2 basal laths and the Mg-matrix. The OR given by the diffraction pattern is $(0001)_{Mg} \parallel (110)_{Mg2Sn}, [2\bar{1}\bar{1}0]_{Mg} \parallel [1\bar{1}1]_{Mg2Sn}$.

5.4.3.2 Type 7 prismatic Mg_2Sn laths with long axis parallel to $\langle 11\bar{2}0\rangle_{Mg}$ directions

The addition of Zn to the binary Mg-6Sn alloy resulted in a new type of prismatic Mg_2Sn lath with its long axis parallel to the three $\langle 11\bar{2}0\rangle_{Mg}$ directions. These precipitates are obviously narrower than the Type 2 basal laths and are wider on the prismatic $\{11\bar{2}0\}_{Mg}$ planes than on the basal. Therefore, these precipitates are categorized as Type 7 prismatic laths. STEM-HAADF images showing the morphology of the Type 7 prismatic laths can be found below in Figure 49, with the Type 7 prismatic laths marked with yellow circles. Another image with the Type 7 prismatic lath edged-on is shown in Figure 50.

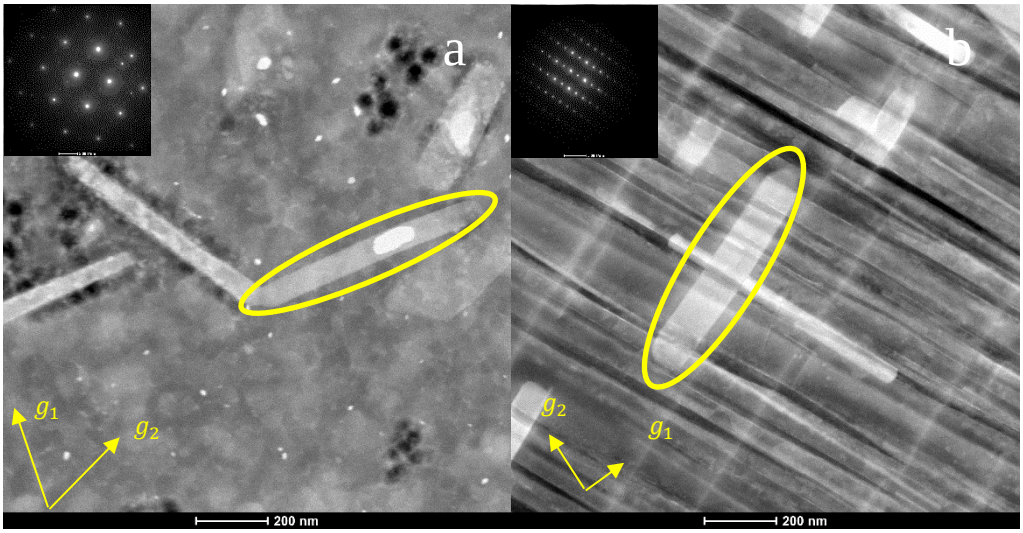


Figure 49 STEM-HAADF images showing the morphology of Type 7 prismatic laths, (a) B ≈ $[0001]_{Mg}, g_1 = 10\bar{1}0_{Mg}, g_2 = 01\bar{1}0_{Mg}$, (b) B ≈ $[11\bar{2}0]_{Mg}, g_1 = 1\bar{1}00_{Mg}, g_2 = 0002_{Mg}$.

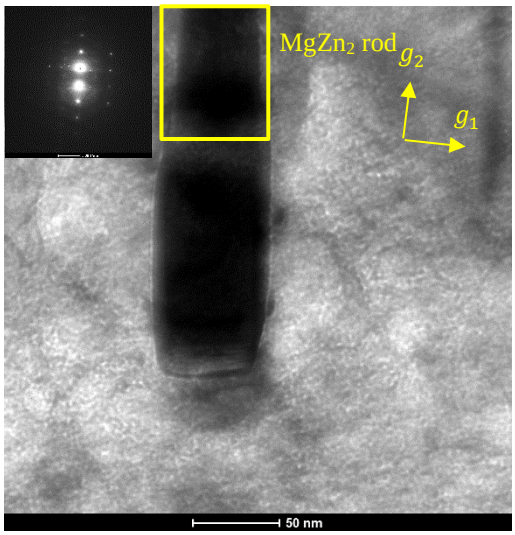


Figure 50 STEM-BF image showing a Type 7 prismatic lath edged-on. B ≈ $[11\bar{2}0]_{Mg}, g_1 = 1\bar{1}00_{Mg}, g_2 = 0002_{Mg}$. The c-axis $MgZn_2$ rod is marked with the yellow rectangle.

For the selected area diffraction patterns shown below in Figure 51, the diffraction patterns from the Mg-matrix and the precipitate can be indexed as $[0001]_{Mg}$ and $[110]_{Mg2Sn}$ respectively. With $g11\bar{2}0_{Mg} \parallel g002_{Mg2Sn}$, $g1\bar{1}00_{Mg} \parallel g2\bar{2}0_{Mg2Sn}$, the OR can be determined as $(0001)_{Mg} \parallel (110)_{Mg2Sn}, [11\bar{2}0]_{Mg} \parallel [001]_{Mg2Sn}$ which is OR1. The

diffraction patterns taken from the Type 7 prismatic laths are therefore similar to those from the Type 1 basal laths. Shi and Zhang observed similar precipitation behaviour in a Mg-Sn-Zn-Mn alloy although the precipitate they reported is not perfectly parallel to the basal plane and the OR is also 0.39° deviated from OR1 and is named "near OR1" [60]. On the other hand, the precipitates in this work are fully parallel to the basal plane and have the precise OR1 relationship.

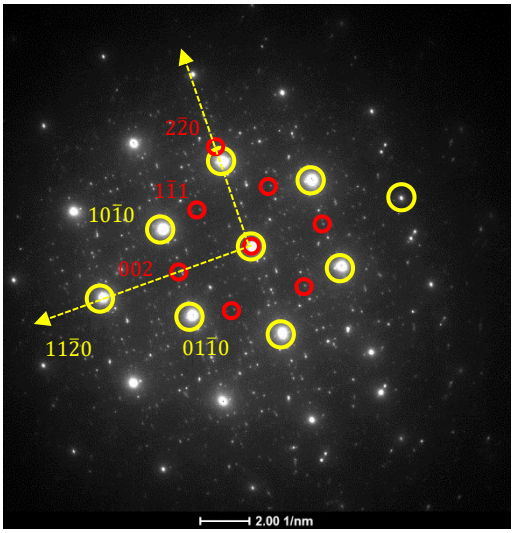


Figure 51 Selected area diffraction pattern indicating the OR between the Type 7 prismatic laths and the Mg-matrix. The OR given by the diffraction pattern is $(0001)_{Mg} \parallel (110)_{Mg2Sn}, [11\bar{2}0]_{Mg} \parallel [001]_{Mg2Sn}$.

5.4.3.3 C-axis $MgZn_2$ rods

Differently from the Al which is homogeneously distributed in the Mg-6Sn-3Al ternary alloy, Zn tends to form its own precipitates in the Mg-6Sn-3Zn alloy. XRD and STEM-EDS confirmed the presence of $MgZn_2$ precipitates in the alloy (see Section 5.4). This phase has an HCP structure with the space group $P6_3/mmc$ (a=0.525nm, c=0.845nm). There are two types of $MgZn_2$ precipitate, wide c-axis $MgZn_2$ rods and narrow c-axis $MgZn_2$ rods. STEM-HAADF images showing the morphology of the $MgZn_2$ precipitates are shown below in

Figure 52. As can be seen from the images, the precipitates with long axis parallel to the $[0001]_{Mg}$ direction are brighter than the attached Mg_2Sn precipitates, which means a higher average atomic mass. These c-axis precipitates are the $MgZn_2$ rods.

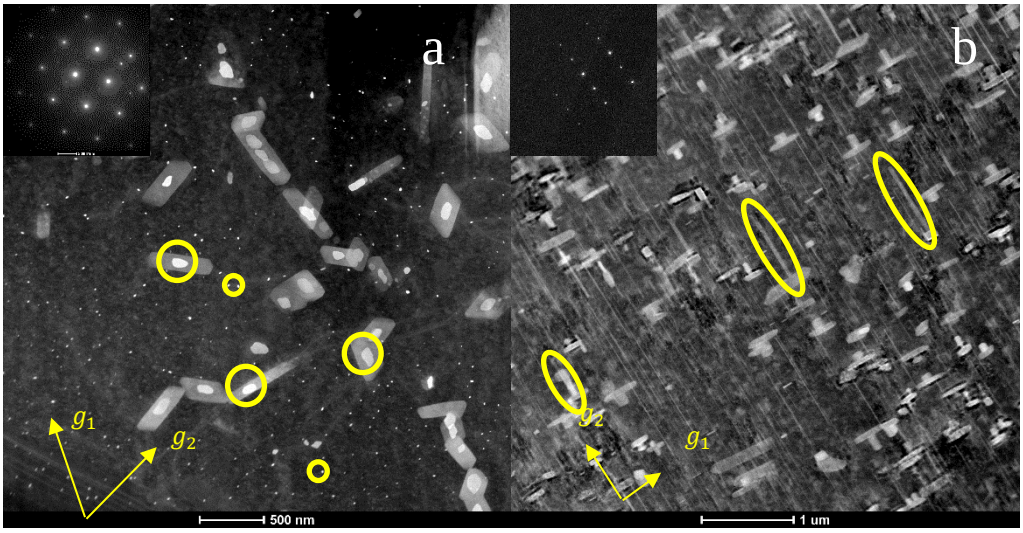


Figure 52 STEM-HAADF images showing the morphology of the $MgZn_2$ precipitates, (a) $B \approx [0001]_{Mg}, g_1 = 10\bar{1}0_{Mg}, g_2 = 01\bar{1}0_{Mg}$, (b) $B \approx [11\bar{2}0]_{Mg}, g_1 = 1\bar{1}00_{Mg}, g_2 = 0002_{Mg}$. Small bright dots are the narrow $MgZn_2$ rods

An illustration of the crystal structure of $MgZn_2$ can be found in Figure 53. Due to the small volume of the $MgZn_2$ precipitates, the diffraction spots from them are fairly weak. A diffraction pattern showing the OR between the $MgZn_2$ precipitates and the matrix can be found below in Figure 54, with the reflections from the Mg-matrix marked in yellow and those from the $MgZn_2$ precipitate marked in red. The diffraction pattern from the Mg-matrix can be indexed as $[1\bar{2}10]_{Mg}$ while that from the $MgZn_2$ precipitates can be indexed as $[10\bar{1}0]_{MgZn2}$. With $g0002_{Mg} \parallel g2\bar{4}20_{MgZn2}$, $g10\bar{1}0_{Mg} \parallel g0002_{MgZn2}$, the OR between the Mg-matrix and the $MgZn_2$ precipitates can be determined as $(0001)_{Mg} \parallel (1\bar{2}10)_{MgZn2}, [11\bar{2}0]_{Mg} \parallel [10\bar{1}0]_{MgZn2}$. This OR can be further confirmed by HRTEM images taken from the Mg-matrix and the $MgZn_2$ precipitate as shown in Figure 55(a) and (b).

The images indicate that $[0001]_{Mg} \parallel [1\bar{2}10]_{MgZn2}, [10\bar{1}0]_{Mg} \parallel [0001]_{MgZn2}, [11\bar{2}0]_{Mg} \parallel [10\bar{1}0]_{MgZn2}$, therefore giving the same OR.

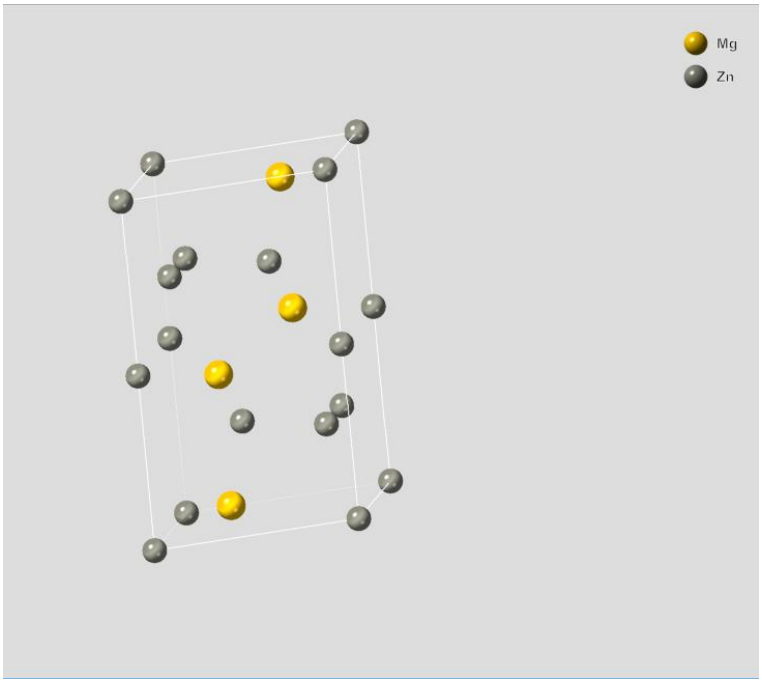


Figure 53 Crystal structure of the $MgZn_2$ precipitate viewed in CrystalMaker

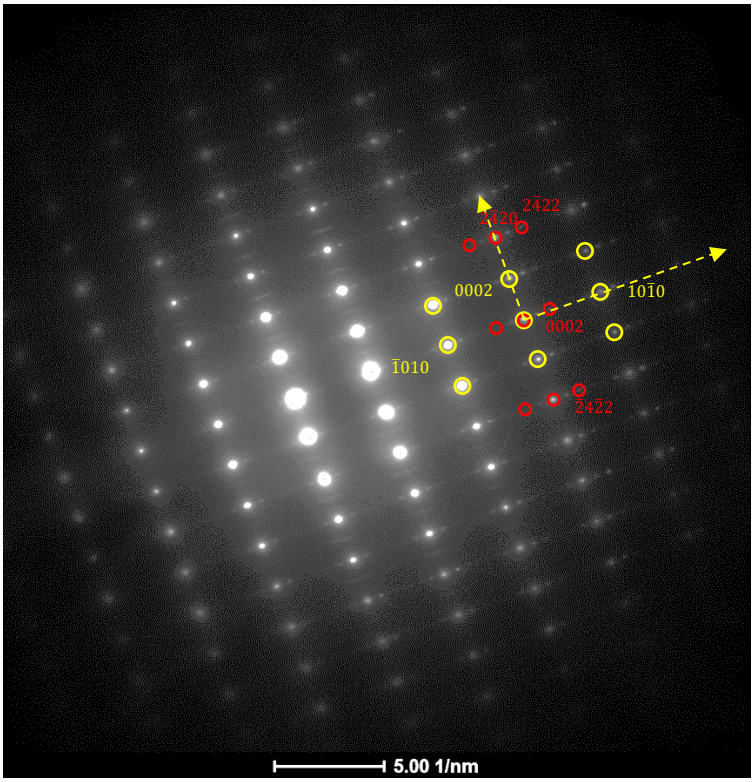


Figure 54 Selected area diffraction pattern showing the OR between the $MgZn_2$ precipitate and the Mg-matrix. The OR given by the diffraction pattern is $[0001]_{Mg} \parallel [1\bar{2}10]_{MgZn2}, [10\bar{1}0]_{Mg} \parallel [0001]_{MgZn2}, [11\bar{2}0]_{Mg} \parallel [10\bar{1}0]_{MgZn2}$.

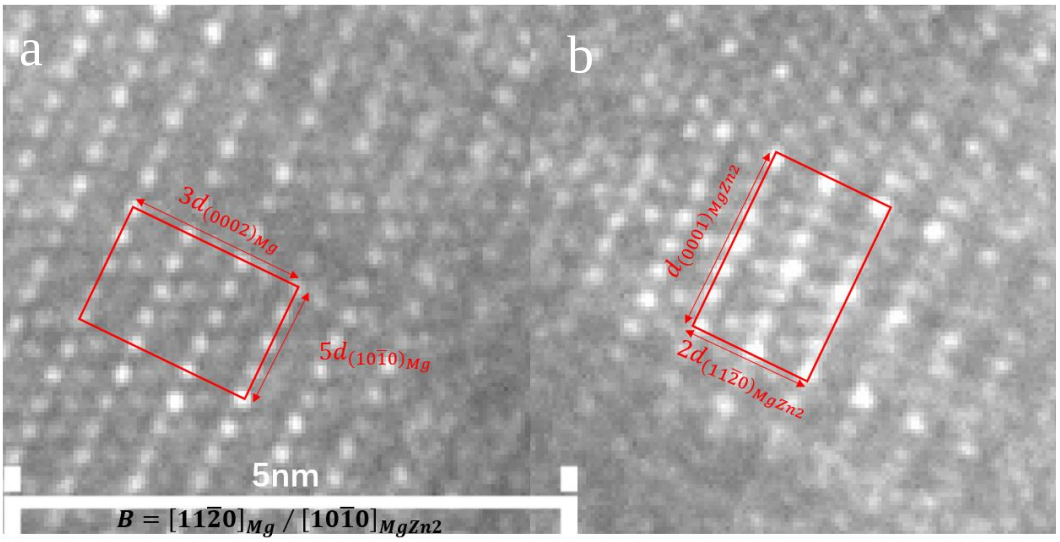


Figure 55 HRTEM image showing the crystal structures of the Mg-matrix and the $MgZn_2$ precipitate. (a) HRTEM image of the Mg-matrix, (b) HRTEM image of the $MgZn_2$ precipitate. Note that the two images were taken inside of each phase under different defocus.

5.4.3.4 The distribution of Zn in the Mg-6Sn-3Zn ternary alloy

As a $MgZn_2$ precipitate has been discovered in the Mg-6Sn-3Zn ternary alloy, it is useful to know the distribution of Zn in the alloy. STEM-EDS mapping has been performed with the maps shown below in Figure 56. Sn and Zn are concentrated in their respective precipitates which are Mg-depleted. In addition, different precipitate types can also be identified in the maps. Type 2, Type 7 Mg_2Sn precipitates and $MgZn_2$ rods are all distinguishable and marked by arrows in the maps.

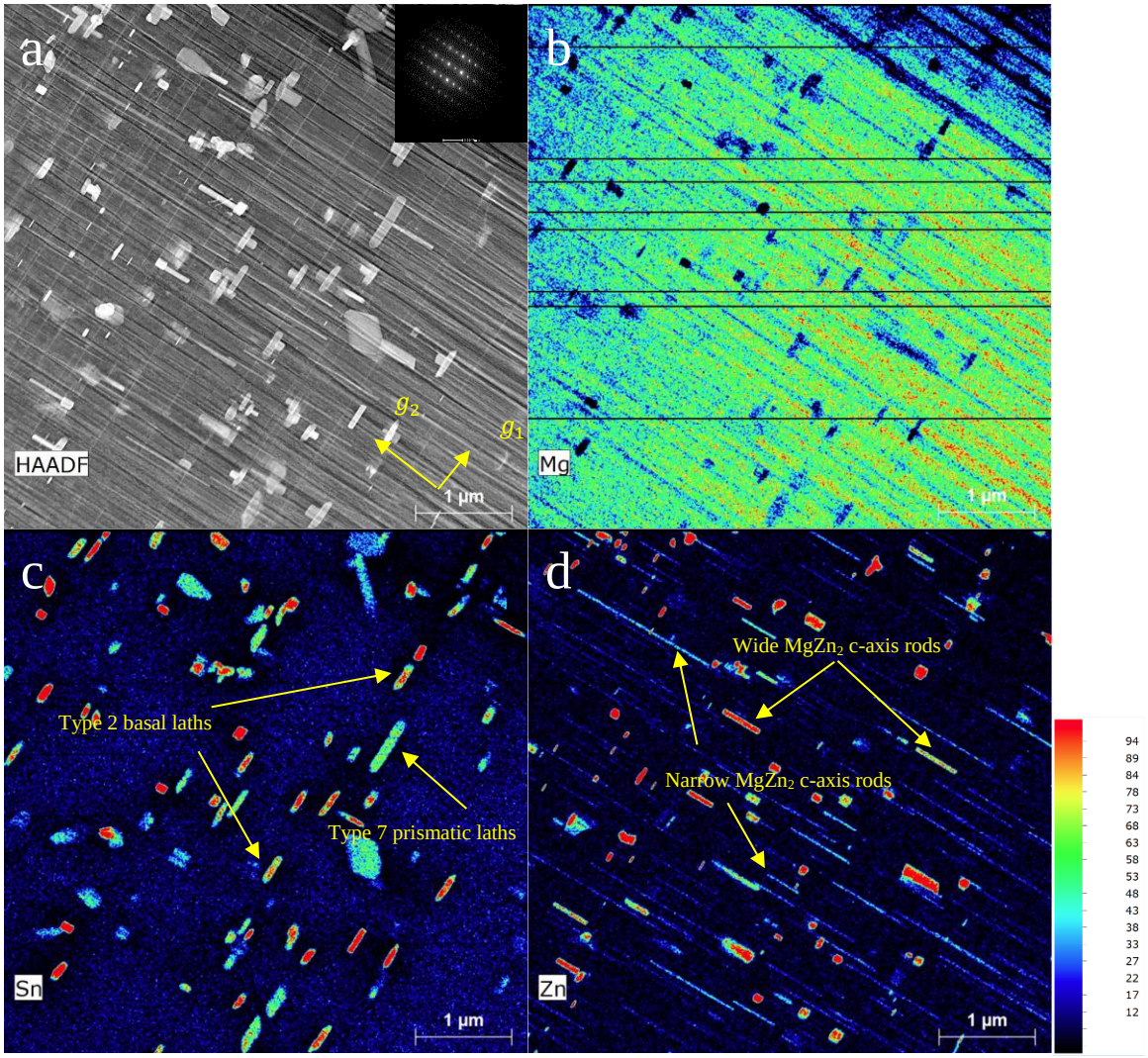


Figure 56 STEM-EDS mapping showing the distribution of elements in the Mg-6Sn-3Zn alloy, B $= [11\bar{2}0]_{Mg}$, $g_1 = 10\bar{1}0_{Mg}$, $g_2 = 0002_{Mg}$. (a) STEM-HAADF image, (b) Mg distribution, (c) Sn distribution, (d) Zn distribution. The stripes on (a) and (b) are from the curtaining effect by FIB milling.

5.4.3.5 The exact morphology of the T-shaped precipitates

As indicated by the TEM images above in Section 5.4.3.2, nearly every Type 2 Mg_2Sn basal lath is connected to a $MgZn_2$ rod. To determine exactly the morphology of the T-shaped precipitates, TEM tomography has been applied.

In order to produce a 3D reconstruction, a tomography holder with a tilting angle of -70°~70° was used to produce 70 STEM-HAADF images at different angles. An image was thus taken every 2°. A few images of a T-shaped precipitate from different tilting angles (respectively -70°, -36°, 0°, 36° and 70°) are presented below in Figure 57. Post processing by the TomoJ plugin of ImageJ produced a stack of 400 images which could then be assembled to produce a reconstructed 3D model. A few stack images are given below in Figure 58 to show different cross sections from the stack.

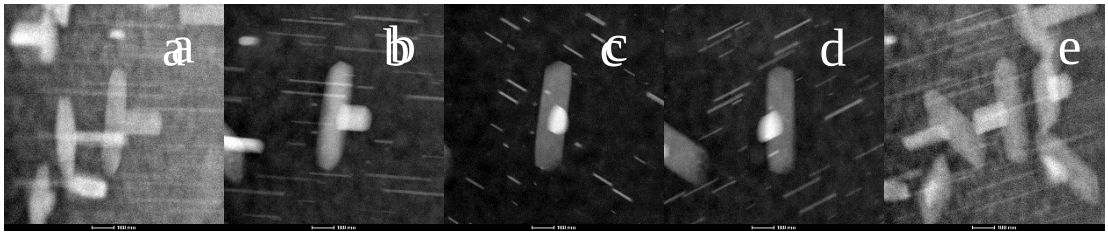


Figure 57 STEM-HAADF images of the precipitate for TEM-tomography, (a) -70° tilt, (b), -36° tilt, (c) 0° tilt, (d) 36° tilt, (e) 70° tilt

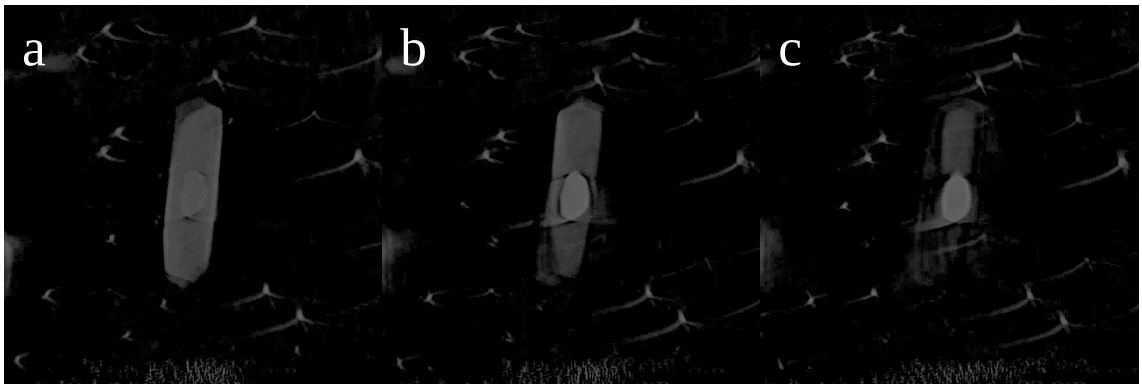


Figure 58 Images from the reconstruction stack showing different cross-sections through the 3D model. (a) Image 100, (b) Image 150, (c) Image 200

3D-reconstruction of the image stacks eventually produced a 3D model in OBJ format, with a three-view schematic shown below in Figure 59. The 3D model clearly shows the morphology of the T-shaped assembly. As can be seen from the images, the Type 2 basal lath

and the c-axis $MgZn_2$ rod are in contact with each other. In addition, the three $[10\bar{1}0]_{Mg}$ facets of the Type 2 basal lath are shown in the images, marked by arrows.

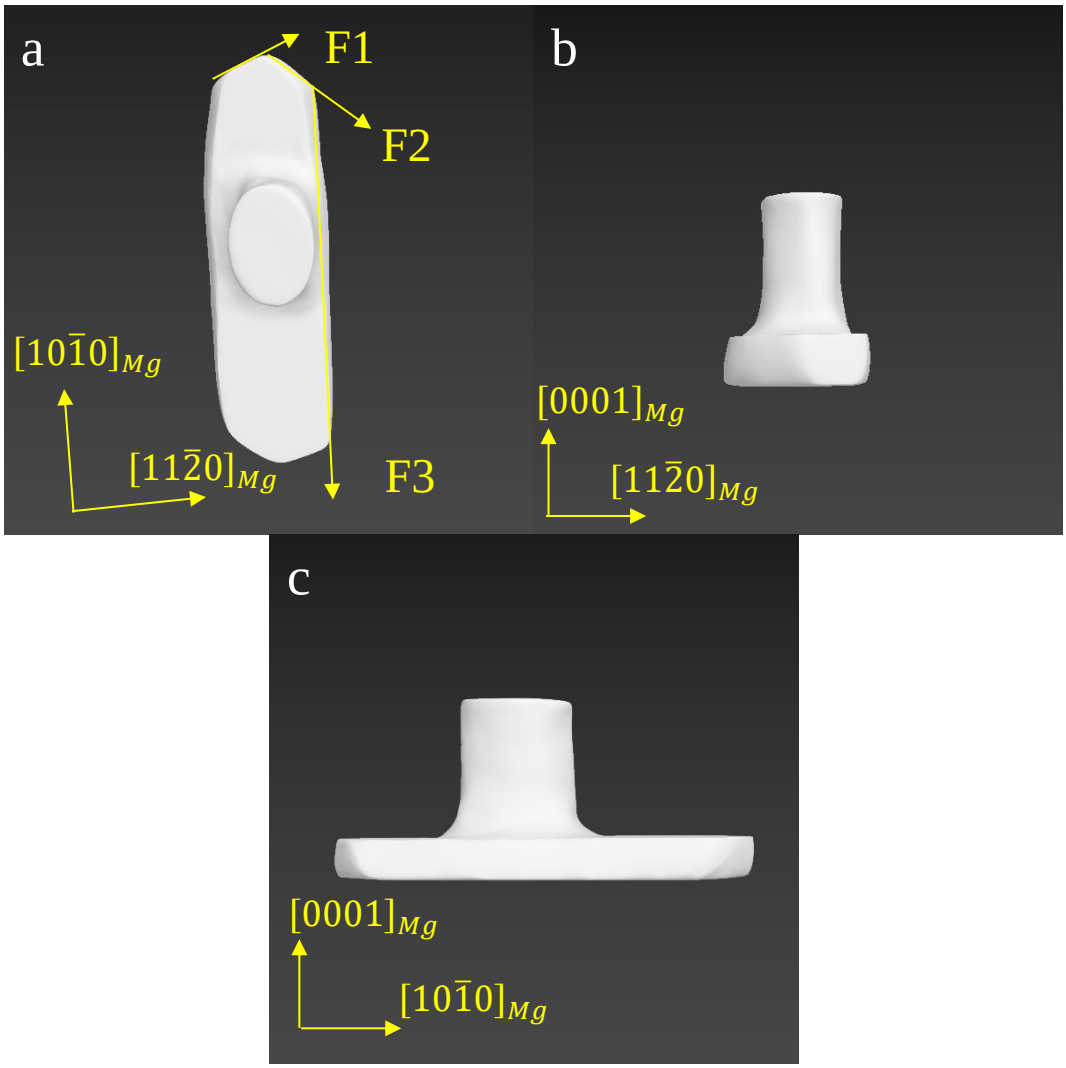


Figure 59 Three different views of the reconstructed 3D model of the T-shaped precipitate, (a) from $[0001]_{Mg}$, (b) from $[10\bar{1}0]_{Mg}$, (c) from $[11\bar{2}0]_{Mg}$

5.5 Summary

To summarize the precipitation behaviour of all three Mg-Sn alloys, the different types of precipitate in the Mg-6Sn binary alloy, Mg-6Sn-3Al ternary and Mg-6Sn-3Zn ternary have been identified and analysed by XRD, STEM-HAADF imaging, STEM-EDS and electron diffraction.

For the Mg-6Sn binary alloy, the Mg_2Sn precipitates are dominated by basal precipitates including Type 1 and Type 2 basal laths which lack the capability for blocking basal slip. The ORs of the two precipitate types were investigated and are in good agreement with previous reports [5], [8], [47], [50], [57] .

The Mg-6Sn-3Al ternary alloy has a much more varied precipitate distribution. Along with the Type 3 and Type 4 basal precipitates, Type 5 c-axis rods and Type 6 pyramidal laths also exist. With a much larger cross-section inclined to the basal plane, these two precipitate types would possess better capability against basal slip. Interestingly, most of the precipitates types in the Mg-6Sn-3Al alloy follow one OR (OR4) [5], [7], [8], [49], [52], [54].

With the addition of Zn, the Mg-6Sn-3Zn alloy exhibits two precipitates phases, Mg_2Sn and $MgZn_2$. The Mg_2Sn precipitates appear as Type 2 basal laths (OR2) with additional Type 7 prismatic laths with OR1. The $MgZn_2$ precipitates normally appear as c-axis rods. Both the Type 7 Mg_2Sn laths and the $MgZn_2$ rods would have the capability to block basal slip. In addition, the combined T-shaped precipitation behaviour of the Type 2 basal laths and the $MgZn_2$ rods has been analysed and a 3D model showing its exact morphology has been produced.

The numerical ratios and dimensions of all types of precipitates have been statistically analysed for later Orowan strengthening calculations. The statistics of the precipitates in the Mg-Sn alloys can be found in Section 7.2.2.

6 Analysis of basal slip using micro-pillar compression

6.1 Introduction

As currently reported research on the mechanical properties of Mg-Sn alloys has only evaluated either hardness [5], [49], [51] (normally Vickers hardness) or macroscopic (i.e. polycrystalline) mechanical strength (normally tensile strength) [58], [59], [80], the exact behaviour of the plastic deformation of Mg-Sn alloys is still not well understood. In the Mg-Sn alloys with non-basal precipitates, basal slip will encounter more resistance. Therefore, as well as evaluating the macroscopic mechanical properties, it will be useful to study how Mg-Sn alloys deform in a single crystal. Using micro-pillar compression tests designed to activate basal slip, the impact of non-basal precipitates on basal slip can be thus evaluated.

6.2 The calculation of Schmid factors in determining the loading direction

To activate the desired basal slip and calculate its CRSS accurately, the Schmid factors for a certain loading direction must be calculated prior to the pillar-compression experiments. Schmid's law can be written as:

$$\tau = m\sigma \qquad \text{Equation 6-1}$$

where σ is the stress applied to the material and m is known as the Schmid factor, being:

$$m = \cos\varphi \cos\lambda \qquad \text{Equation 6-2}$$

where φ is the angle between the loading direction $[u_1 v_1 t_1 w_1]$ and the slip plane normal $[h_1 k_1 i_1 l_1]$ and λ is the angle between the loading direction $[u_1 v_1 t_1 w_1]$ and the slip direction

$[u_2 v_2 t_2 w_2]$. For an HCP crystal e.g. magnesium, the Schmid factor can be calculated using the following equation [81]:

$$\mathrm{m} = \cos\varphi \cos\lambda = \frac{h_1u_1+k_1v_1+i_1t_1+\frac{3c^2}{2a^2}l_1w_1}{\sqrt{\left(h_1^2+k_1^2+i_1^2+\frac{3c^2}{2a^2}l_1^2\right)\left(u_1^2+v_1^2+t_1^2+\frac{3c^2}{2a^2}w_1^2\right)}} \frac{u_1u_2+v_1v_2+t_1t_2+\frac{3c^2}{2a^2}w_1w_2}{\sqrt{\left(u_1^2+v_1^2+t_1^2+\frac{3c^2}{2a^2}w_1^2\right)\left(u_2^2+v_2^2+t_2^2+\frac{3c^2}{2a^2}w_2^2\right)}}$$

Equation 6-3

For all three Mg-Sn alloys, the Schmid factors for each slip system have been calculated and are listed in Table 12, Table 13 and Table 14. Note that a negative value indicates an opposite slip direction and does not indicate that the Schmid factor is negative. For some loading directions, although the Schmid factors for some slip systems are high (e.g., 1st order pyramidal $\langle a \rangle$ slip), the CRSS for pyramidal slip is much higher than that of the basal slip, and therefore basal slip is still expected to dominate the deformation behaviour.

Table 12 Calculated Schmid factors for possible slip systems in the peak aged Mg-6Sn alloy with their respective loading directions (Highest Schmid factors are marked in red)

Slip system	**Slip plane**	**Slip direction**	**Loading direction**	
			$[01\bar{1}1]_{Mg}$	$[\bar{1}2\bar{1}\bar{2}]_{Mg}$
Basal $\langle a \rangle$	$(0001)_{Mg}$	$[11\bar{2}0]_{Mg}$	**0.4321**	0.2492
	$(0001)_{Mg}$	$[\bar{2}110]_{Mg}$	0.0000	0.2492
	$(0001)_{Mg}$	$[1\bar{2}10]_{Mg}$	**-0.4321**	**-0.4984**
Prismatic $\langle a \rangle$	$(1\bar{1}00)_{Mg}$	$[11\bar{2}0]_{Mg}$	-0.2303	-0.1992
	$(10\bar{1}0)_{Mg}$	$[1\bar{2}10]_{Mg}$	-0.2303	0.0000
	$(01\bar{1}0)_{Mg}$	$[\bar{2}110]_{Mg}$	0.0000	-0.1992
	$(1\bar{1}01)_{Mg}$	$[11\bar{2}0]_{Mg}$	-0.0005	-0.0589
	$(10\bar{1}1)_{Mg}$	$[1\bar{2}10]_{Mg}$	-0.4062	-0.2340

1st order pyramidal $\langle a \rangle$	$(01\bar{1}1)_{Mg}$	$[11\bar{2}0]_{Mg}$	0.0000	-0.2929

Table 13 Calculated Schmid factors for possible slip systems in the peak aged Mg-6Sn-3Al alloy with their respective loading directions (Highest Schmid factors are marked in red)

Slip system	**Slip plane**	**Slip direction**	**Loading direction**	
			$[\bar{1}3\bar{2}\bar{2}]_{Mg}$	$[\bar{1}8\bar{7}\bar{9}]_{Mg}$
Basal $\langle a \rangle$	$(0001)_{Mg}$	$[11\bar{2}0]_{Mg}$	-0.3089	-0.3990
	$(0001)_{Mg}$	$[\bar{2}110]_{Mg}$	-0.1545	-0.0570
	$(0001)_{Mg}$	$[1\bar{2}10]_{Mg}$	**0.4634**	**0.4560**
Prismatic $\langle a \rangle$	$(1\bar{1}00)_{Mg}$	$[11\bar{2}0]_{Mg}$	-0.3293	-0.2126
	$(10\bar{1}0)_{Mg}$	$[1\bar{2}10]_{Mg}$	-0.1235	-0.1620
	$(01\bar{1}0)_{Mg}$	$[\bar{2}110]_{Mg}$	-0.2058	-0.0506
1st order pyramidal $\langle a \rangle$	$(1\bar{1}01)_{Mg}$	$[11\bar{2}0]_{Mg}$	-0.4357	-0.3750
	$(10\bar{1}1)_{Mg}$	$[1\bar{2}10]_{Mg}$	0.1085	0.0710
	$(01\bar{1}1)_{Mg}$	$[11\bar{2}0]_{Mg}$	-0.1092	-0.0179

Table 14 Calculated Schmid factors for possible slip systems in the peak aged Mg-6Sn-3Zn alloy with their respective loading directions (Highest Schmid factors are marked in red)

Slip system	**Slip plane**	**Slip direction**	**Loading direction**	
			$[\bar{1}8\bar{7}\bar{6}]_{Mg}$	$[25\bar{7}6]_{Mg}$
Basal $\langle a \rangle$	$(0001)_{Mg}$	$[11\bar{2}0]_{Mg}$	-0.3848	**0.4828**
	$(0001)_{Mg}$	$[\bar{2}110]_{Mg}$	-0.0550	-0.1379

	$(0001)_{Mg}$	$[1\bar{2}10]_{Mg}$	**0.4397**	-0.3448
Prismatic $\langle a \rangle$	$(1\bar{1}00)_{Mg}$	$[11\bar{2}0]_{Mg}$	-0.3076	-0.1286
	$(10\bar{1}0)_{Mg}$	$[1\bar{2}10]_{Mg}$	-0.2344	-0.2757
	$(01\bar{1}0)_{Mg}$	$[\bar{2}110]_{Mg}$	-0.0732	0.1470
1st order pyramidal $\langle a \rangle$	$(1\bar{1}01)_{Mg}$	$[11\bar{2}0]_{Mg}$	-0.4522	0.1130
	$(10\bar{1}1)_{Mg}$	$[1\bar{2}10]_{Mg}$	-0.0005	-0.4053
	$(01\bar{1}1)_{Mg}$	$[11\bar{2}0]_{Mg}$	-0.0389	0.1946

Micro-pillars have been fabricated from the peak-aged Mg-6Sn, Mg-6Sn-3Al and Mg-6Sn-3Zn alloys by SEM-FIB. For Orowan strengthening investigation involving precipitates, a larger pillar size will be needed to assure enough dislocation-precipitate interaction. Therefore, the pillars used in this study were chosen to have a diameter of 10μm and a height of ~20μm. A moderate height-diameter ratio of the pillars is important, as a higher ratio may cause the pillars easy to buckle. The micro-pillars were compressed with a loading direction favourable for basal slip using the grains that are favourably oriented and selected via EBSD. The as-produced stress-strain curves have been evaluated alongside the TEM images of the TEM foils fabricated from the as-compressed pillars with the sample normal determined via EBSD. 4 pillars were milled and compressed respectively for each loading direction. The pillars were compressed to a strain of 10%, with their yield stress determined by the 0.2% proof stress.

6.3 Basal slip behaviour of the peak aged Mg-6Sn binary alloy

6.3.1 Micro-pillar compression of the peak aged Mg-6Sn binary alloy

An SEM image of an as-milled pillar of the peak aged Mg-6Sn binary alloy before compression is shown below in Figure 60, while the image of an as-compressed pillar compressed along $[01\bar{1}1]_{Mg}$ is shown in Figure 61. The slip traces can clearly be seen on the as-compressed pillars, indicating a slip system has been activated.

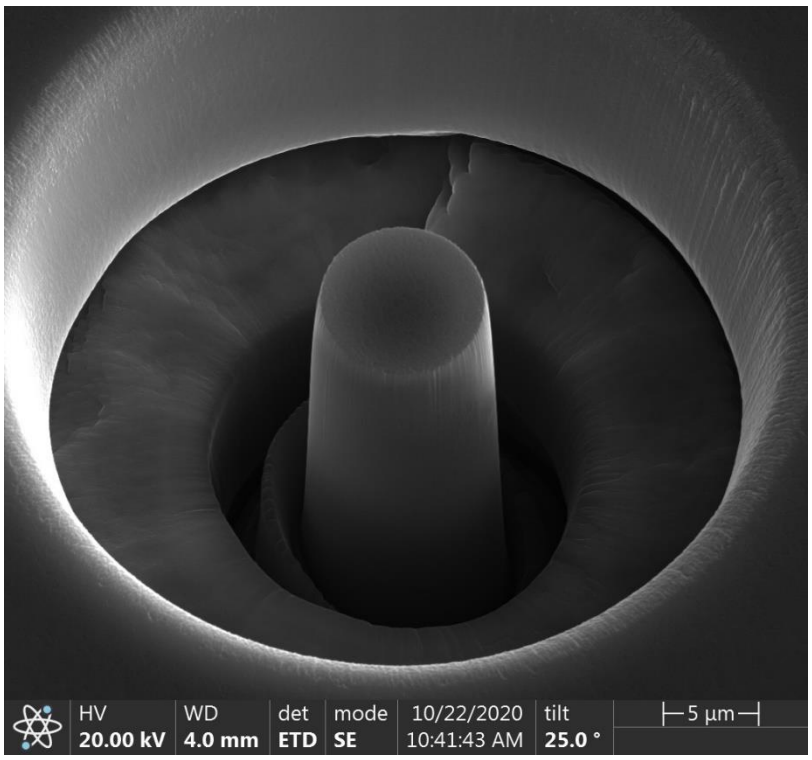


Figure 60 SEM image of an as-milled pillar from the peak-aged Mg-6Sn alloy

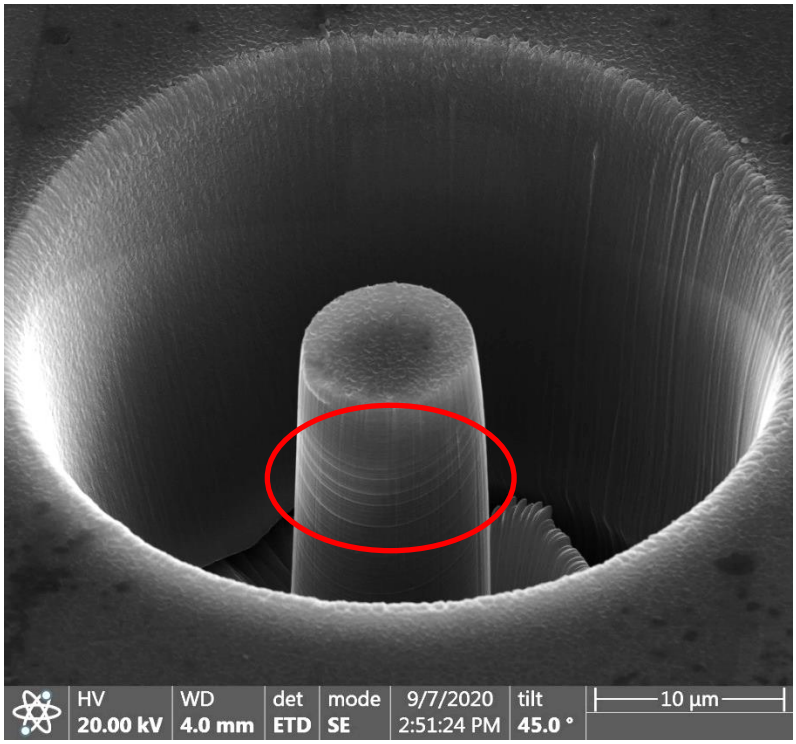


Figure 61 SEM image of an as-compressed pillar from the peak-aged Mg-6Sn alloy compressed along $[01\bar{1}1]_{Mg}$. The slip traces of the $\frac{1}{3}\langle 11\bar{2}0\rangle(0001)_{Mg}$ slip system can be seen clearly and are marked with a red ellipse

The stress-strain curves acquired from loading directions $[01\bar{1}1]_{Mg}$ and $[\bar{1}2\bar{1}\bar{2}]_{Mg}$ were plotted and are shown in Figure 62 and Figure 63. During loading, near linear elastic deformation occurs first and can be observed in the curves for both loading directions, indicating a good alignment between the compression tip and the pillar top. After elastic deformation, the pillars began to yield, detectably from ~0.2% strain. Strain bursts and load drops can be observed in the curves for both loading directions, but are more obvious for the pillars loaded along $[\bar{1}2\bar{1}\bar{2}]_{Mg}$, as indicated by the red ellipses. This is mainly due to the generation and motion of dislocations which will result in the formation of slip bands. No obvious work hardening can be observed in the stress-strain curves, which can be explained by the lack of resistance to basal dislocation motion, a result of basal precipitate-dominated

microstructure. For the binary Mg-6Sn alloy, the microstructure is dominated by two types of precipitate, both basal. With a low effective cross-section perpendicular to the basal plane, the dislocations will not effectively interact with the precipitates, thus causing a low CRSS and work hardening.

The mean averaged yield stress determined from the 0.2% proof stress is 28.66MPa, leading to the as-calculated average CRSS for both loading directions being 13.22MPa.

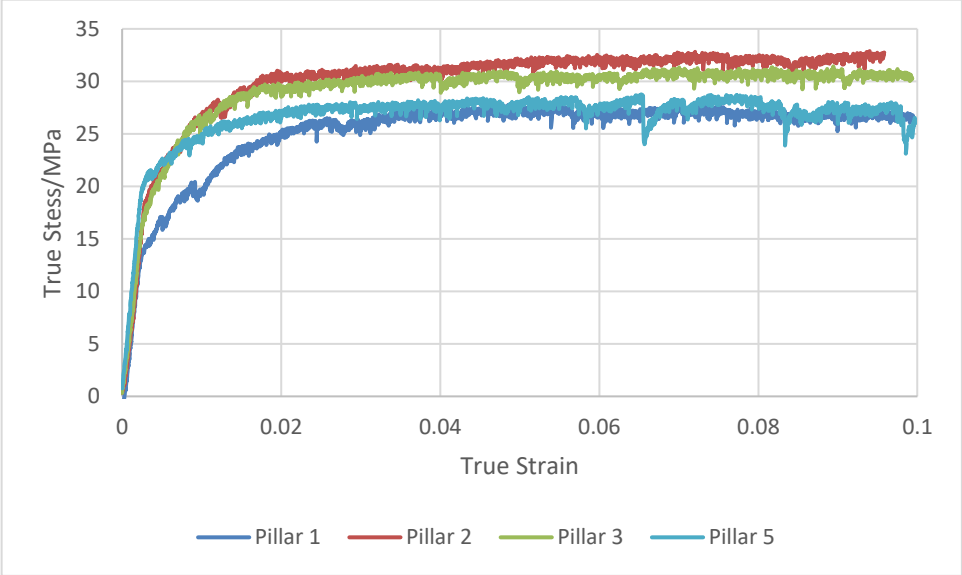


Figure 62 Stress-strain curves obtained from as-compressed pillars from peak aged Mg-6Sn alloy with a loading direction of $[01\bar{1}1]_{Mg}$

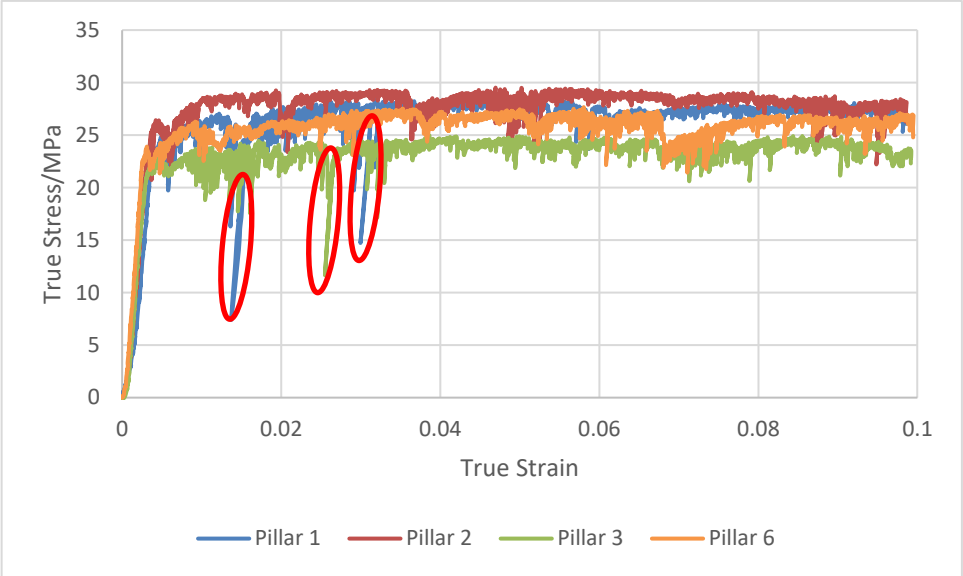


Figure 63 Stress-strain curves obtained from as-compressed pillars of peak aged Mg-6Sn alloy with a loading direction of $[\bar{1}2\bar{1}\bar{2}]_{Mg}$. Note that obvious strain bursts are marked by red ellipses.

6.3.2 Dislocation analysis of the Mg-6Sn pillars compressed along $[01\bar{1}1]_{Mg}$

A TEM foil from pillar 1 for the $[01\bar{1}1]_{Mg}$ loading direction has been fabricated along the dashed line as shown in Figure 64. This direction ensures the slip direction is in the foil and is therefore providing a foil normal of near $\langle 10\bar{1}0\rangle_{Mg}$ or $\langle 11\bar{2}0\rangle_{Mg}$. For this specific TEM foil, the foil normal is $[1\bar{2}10]_{Mg}$.

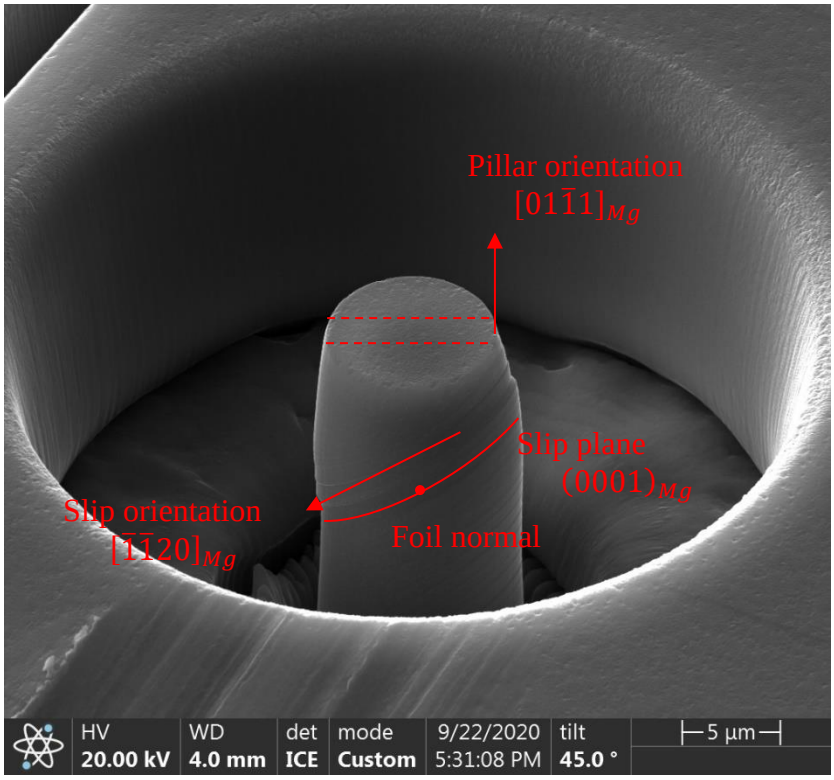


Figure 64 Pillar 1 with a $[01\bar{1}1]_{Mg}$ loading direction, with the TEM foil lift out marked by the red dashed lines

When imaged along $[1\bar{2}10]_{Mg}$ with $\mathrm{g} = 0002$, as shown in Figure 65, no dislocations can be observed i.e. $\mathrm{g} \cdot \mathrm{b} = 0$. By changing the g vector to $\mathrm{g} = 10\bar{1}0$, the dislocations became visible, as shown in Figure 66. The dislocations are edged-on when observed from $[1\bar{2}10]_{Mg}$. Therefore, these dislocations can be confirmed being basal a dislocations. In addition, no other types of dislocations were found in the TEM samples, indicating that basal a slip is the only slip system activated. No precipitate shearing is observed.

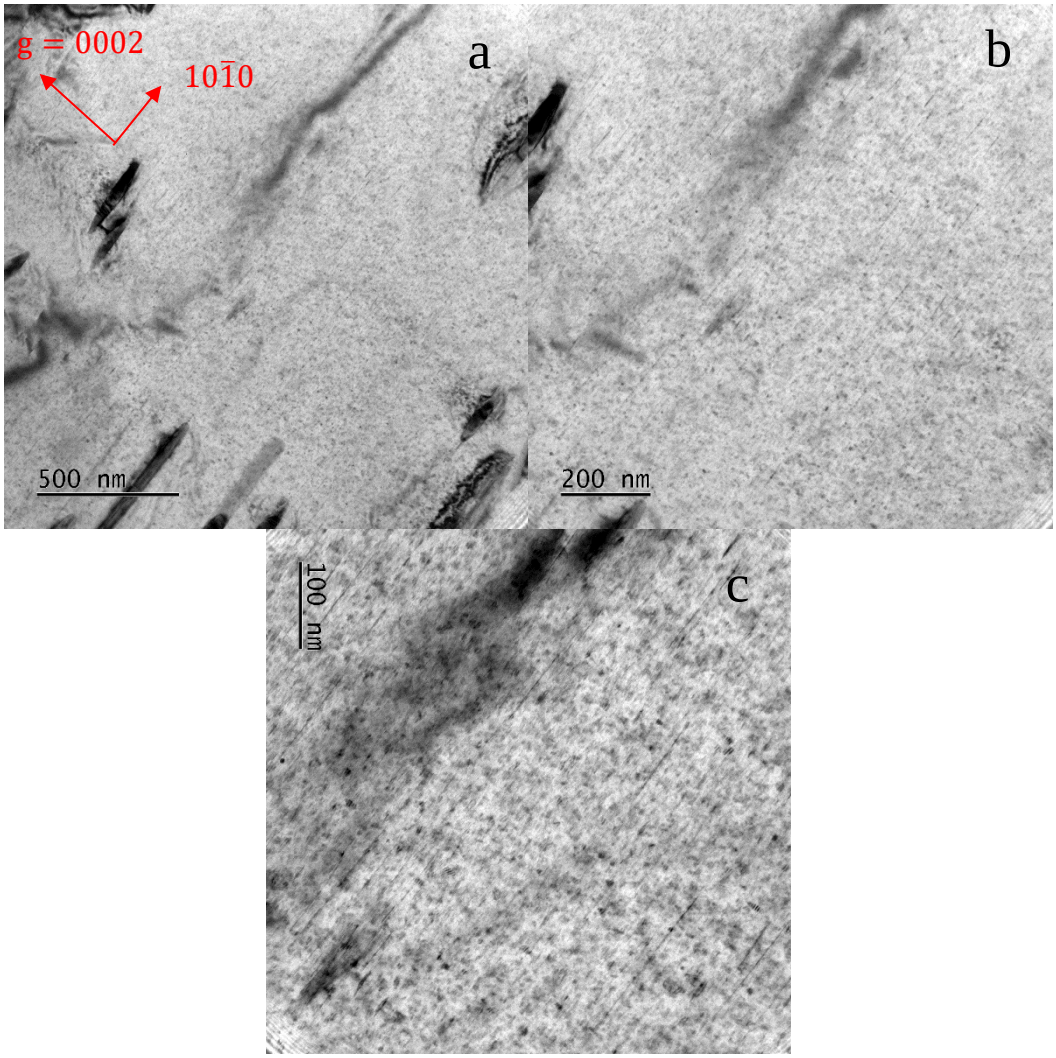


Figure 65 TEM images from a Mg-6Sn pillar compressed along $[01\bar{1}1]_{Mg}$, viewed along $[1\bar{2}10]_{Mg}$ with g = 0002. (a) low magnification, (b) medium magnification, (c) high magnification. All dislocations are invisible.

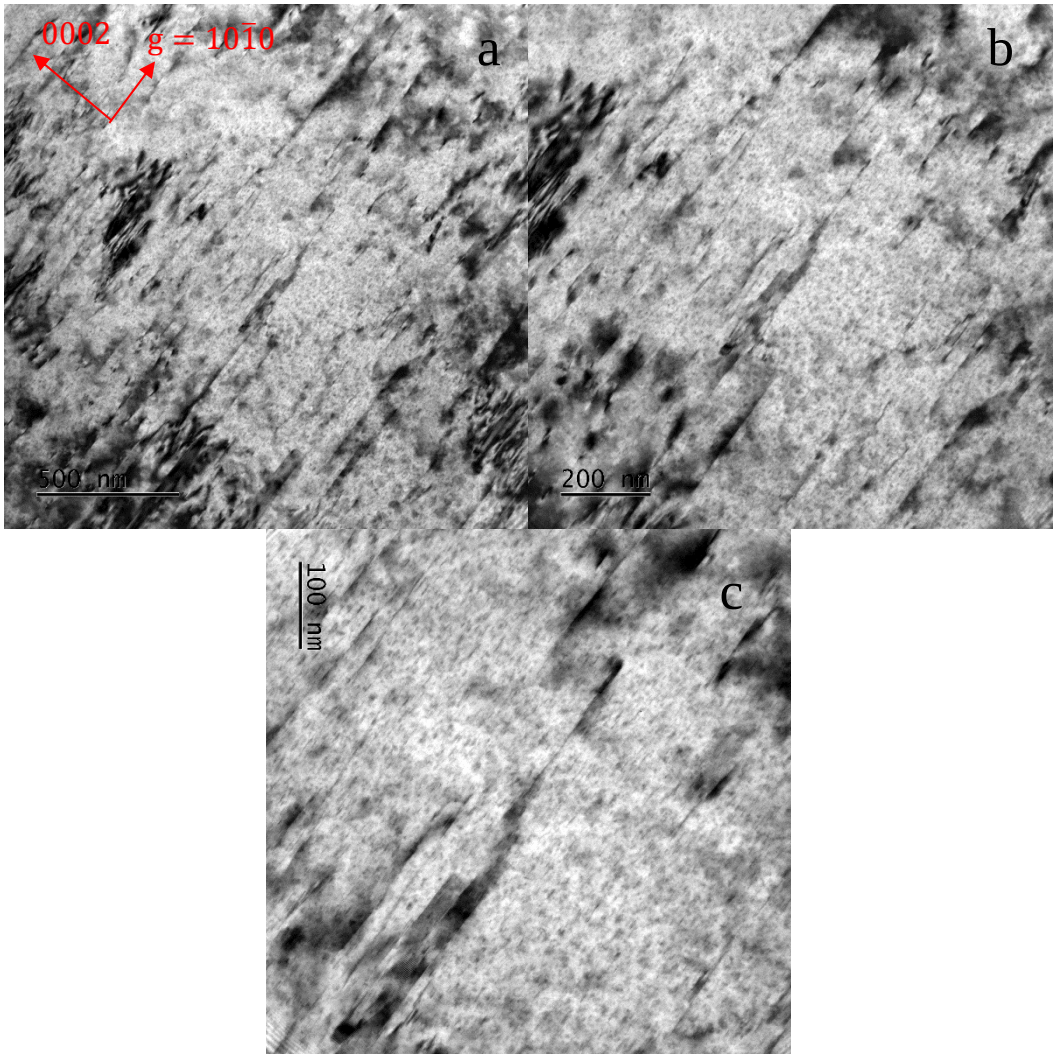


Figure 66 TEM images from a Mg-6Sn pillar compressed along $[01\bar{1}1]_{Mg}$, viewed along $[1\bar{2}10]_{Mg}$ with g = 10$\bar{1}$0. (a) low magnification, (b) medium magnification, (c) high magnification. The same viewing area as in Figure 65. The dislocations have become visible.

6.4 Basal slip behaviour of the peak aged Mg-6Sn-3Al ternary alloy

6.4.1 Micro-pillar compression of the peak aged Mg-6Sn-Al ternary alloy

An SEM image of an as-milled Mg-6Sn-3Al micro-pillar before compression is shown below in Figure 67, with the image of an as-compressed pillar shown in Figure 68. Obvious slip traces can be seen on the pillar, proving that a slip system has been activated.

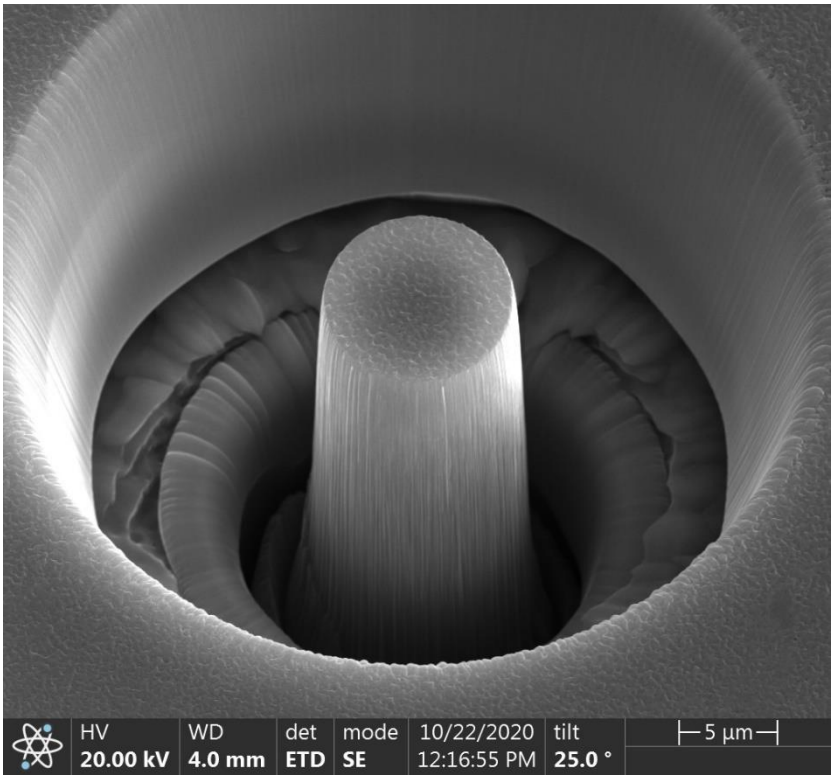


Figure 67 SEM image of an as-milled pillar from the peak-aged Mg-6Sn-3Al alloy

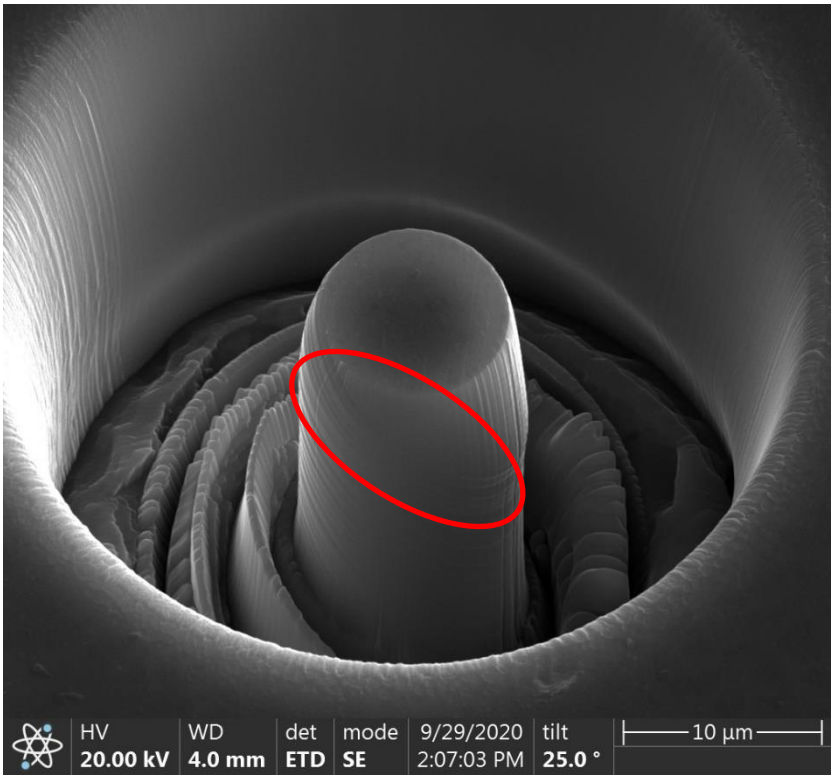


Figure 68 SEM image of an as-compressed pillar from the peak aged Mg-6Sn-3Al alloy. The slip traces of the $\frac{1}{3}\langle 11\bar{2}0\rangle(0001)_{Mg}$ slip system can clearly be seen from the image and are marked with a red ellipse.

Stress-strain curves from the as-compressed pillars compressed along $[\bar{1}3\bar{2}\bar{2}]_{Mg}$ and $[\bar{1}8\bar{7}\bar{9}]_{Mg}$ are shown respectively in Figure 69 and Figure 70 respectively. The elastic and yielding part of the curves is similar to that of the Mg-6Sn. Strain bursts and load drops can be observed for both loading directions, but is more obvious for the $[\bar{1}8\bar{7}\bar{9}]_{Mg}$ loading direction, as marked by the red ellipses in Figure 70. Slight work hardening can also be observed for the $[\bar{1}8\bar{7}\bar{9}]_{Mg}$ loading direction, which could possibly indicate that the pyramidal laths and c-axis rods have interacted with the basal slip, but still to a low extent.

The mean yield stress determined by the 0.2% proof stress is 46.42MPa, leading to an average CRSS of 21.34MPa. This is 8.12MPa higher than for the Mg-6Sn binary alloy, probably due to the non-basal precipitates.

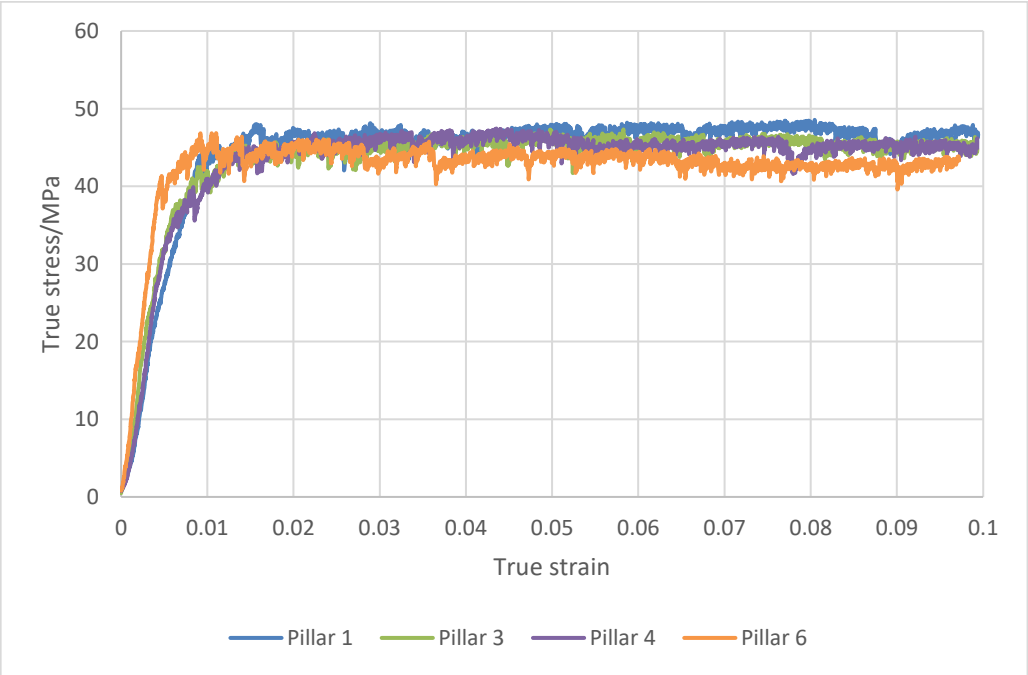


Figure 69 Stress-strain curves obtained from as-compressed pillars of the peak aged Mg-6Sn-3Al alloy with a loading direction of $[\bar{1}3\bar{2}\bar{2}]_{Mg}$

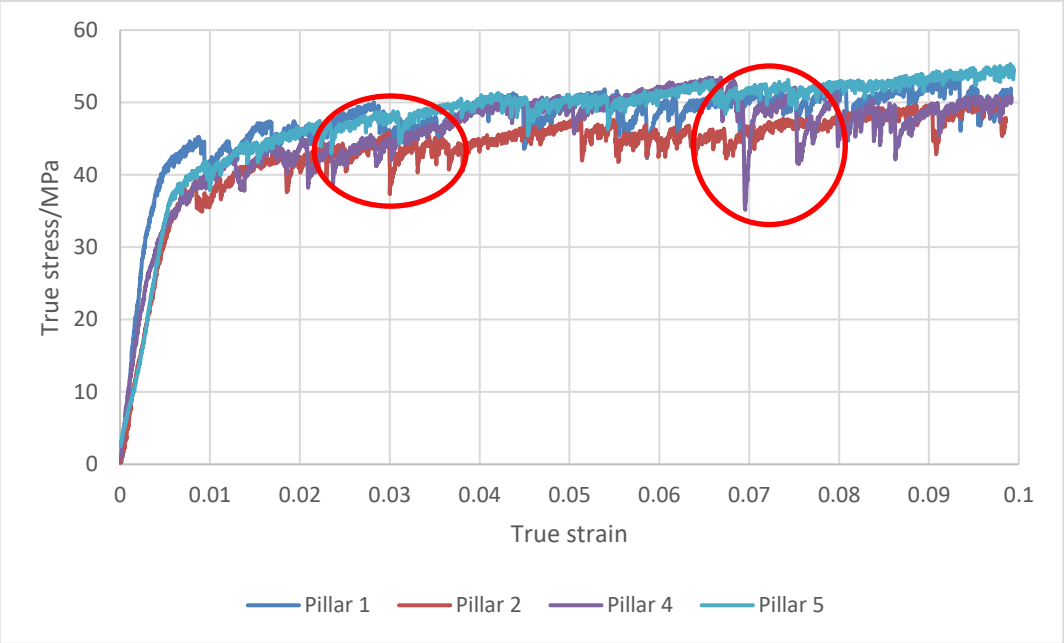


Figure 70 Stress-strain curves obtained from as-compressed pillars from peak aged Mg-6Sn-3Al alloy with a loading direction of $[\bar{1}8\bar{7}\bar{9}]_{Mg}$. Strain bursts have been marked with red ellipses.

6.4.2 Dislocation analysis for the Mg-6Sn-3Al pillars compressed along $[\bar{1}8\bar{7}\bar{9}]_{Mg}$

A TEM foil has been fabricated from a pillar compressed along $[\bar{1}8\bar{7}\bar{9}]_{Mg}$. The image of the pillar is shown below in Figure 71, with the dashed lines marking the TEM foil lift out. This direction ensures the slip direction is in the foil and is therefore providing a foil normal of near $\langle 10\bar{1}0\rangle_{Mg}$ or $\langle 11\bar{2}0\rangle_{Mg}$. For this specific TEM foil, the foil normal is $[1\bar{1}00]_{Mg}$.

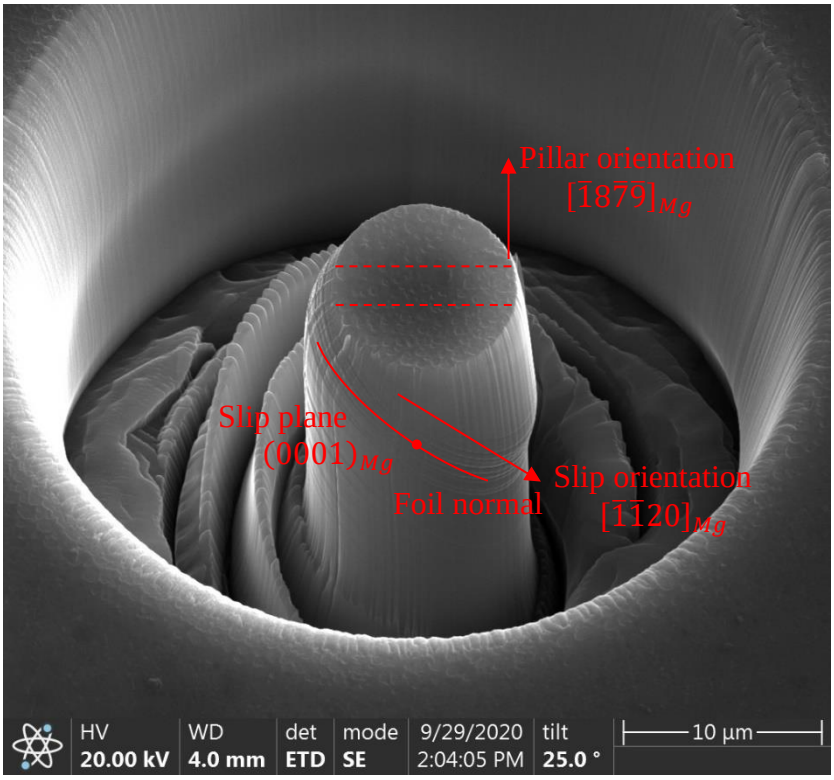


Figure 71 Pillar 1 with a $[\bar{1}8\bar{7}\bar{9}]_{Mg}$ loading direction, with the TEM foil lift out position marked by the red dashed lines

When imaged with a beam direction of $[1\bar{1}00]_{Mg}$, with $g = 0002$, as shown below in Figure 72, no dislocations can be observed with this imaging condition, which results in $g \cdot b = 0$. By changing the g vector to $g = 11\bar{2}0$, the dislocations became visible as shown in Figure 73. With the viewing direction of $[1\bar{1}00]_{Mg}$, all dislocations were edged-on, indicating their basal a dislocation identity. No other types of dislocations were found in the TEM samples, hence basal a slip is the only slip system activated. Despite the rod-like basal precipitates, precipitate shearing is also not observed on the pyramidal laths and c-axis rods.

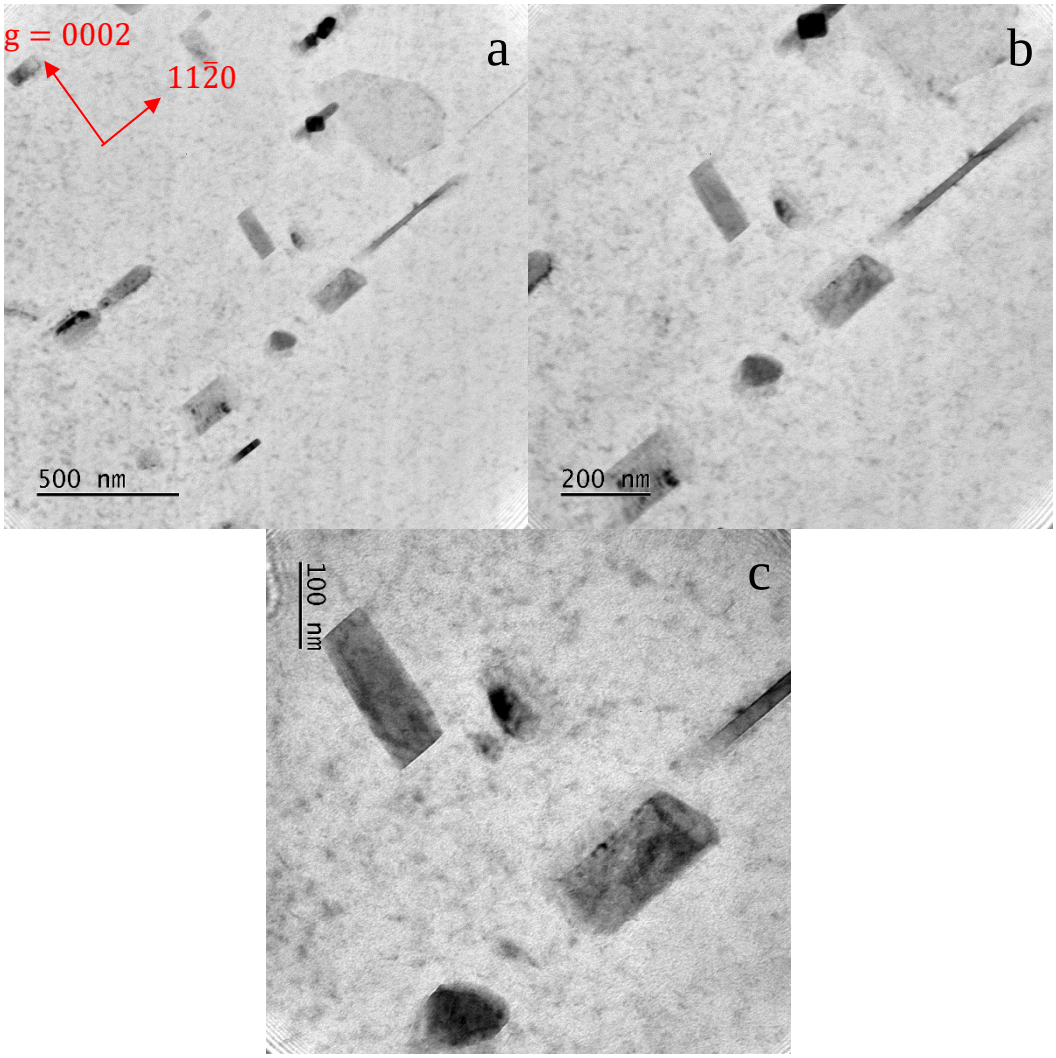


Figure 72 TEM images from a Mg-6Sn-3Al pillar compressed along $[\bar{1}8\bar{7}\bar{9}]_{Mg}$, viewed along $[1\bar{1}00]_{Mg}$ with g = 0002. (a) low magnification, (b) medium magnification, (c) high magnification

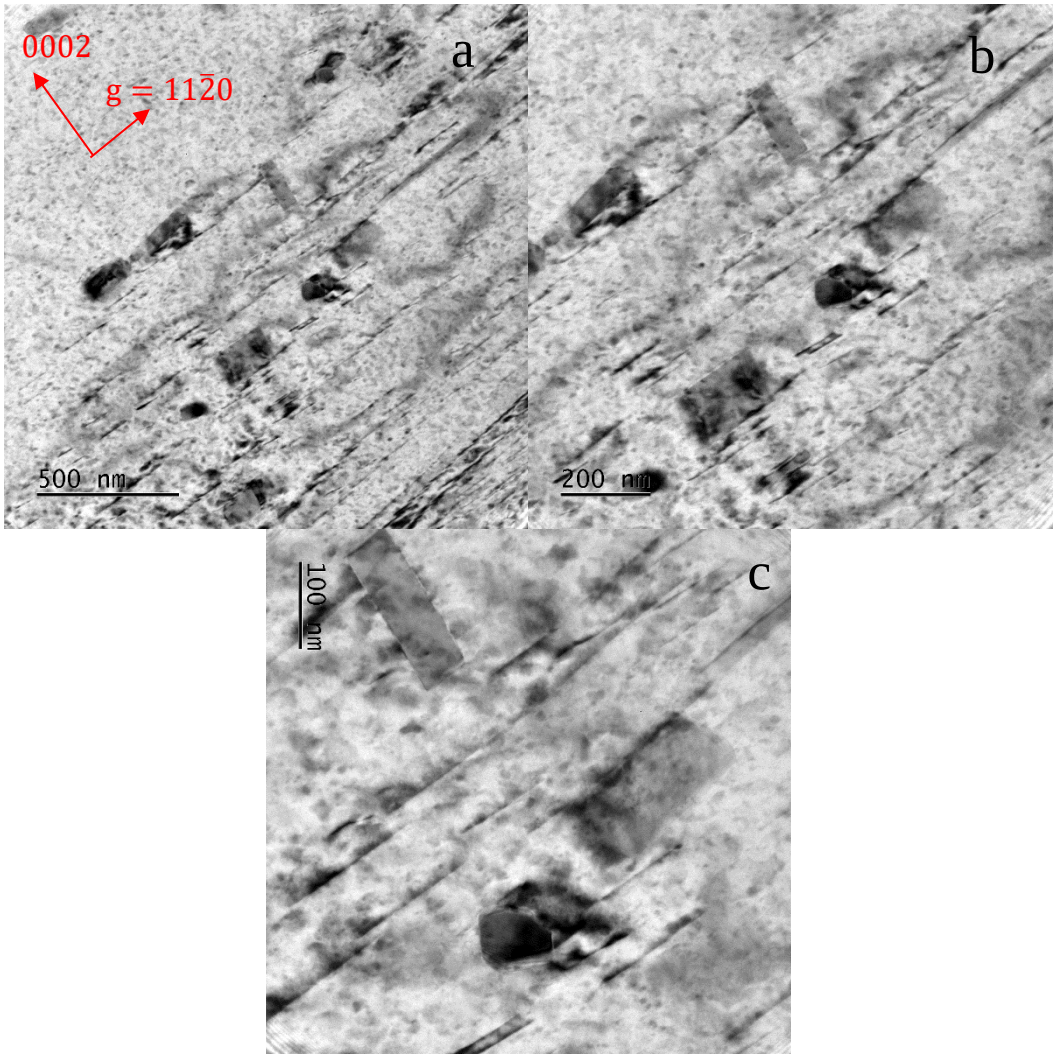


Figure 73 TEM images from a Mg-6Sn -3Al pillar compressed along $[\bar{1}8\bar{7}\bar{9}]_{Mg}$, viewed along $[1\bar{1}00]_{Mg}$ with g = 11$\bar{2}$0. (a) low magnification, (b) medium magnification, (c) high magnification. Dislocations have become visible.

6.5 Basal slip behaviour of the peak aged Mg-6Sn-3Zn alloy

6.5.1 Micro-pillar compression of the peak aged Mg-6Sn-3Zn alloy

An SEM image of an as-milled pillar of peak aged Mg-6Sn-3Zn binary alloy before compression is shown below in Figure 74, while the image of an as-compressed pillar

compressed along $[25\bar{7}6]_{Mg}$ is shown in Figure 75. Similar to the Mg-6Sn and the Mg-6Sn-3Al the slip traces can clearly be seen on the as-compressed pillars.

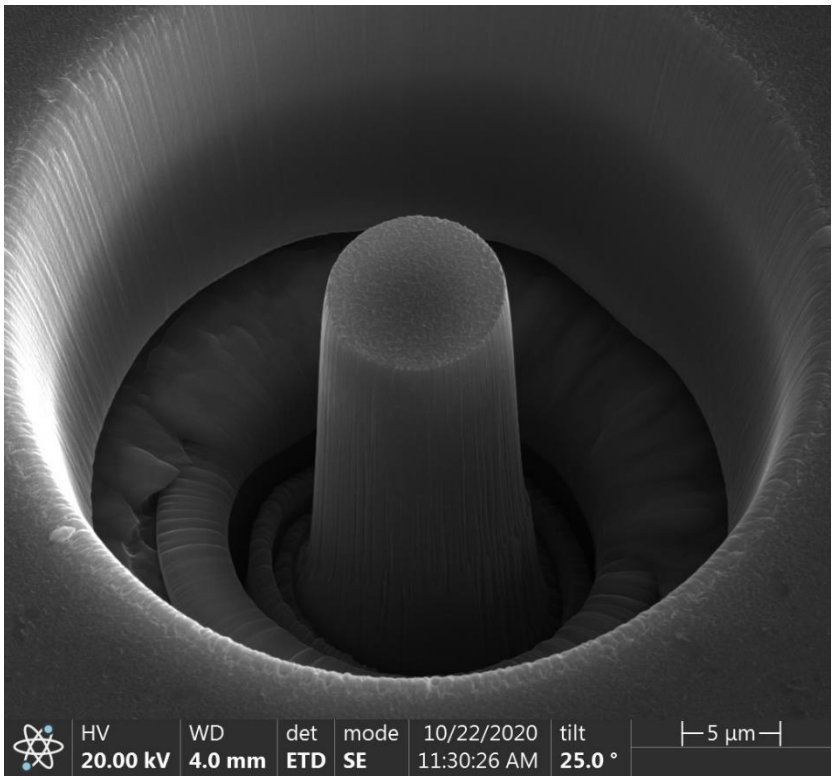


Figure 74 SEM image of an as-milled pillar from the peak-aged Mg-6Sn-3Zn alloy

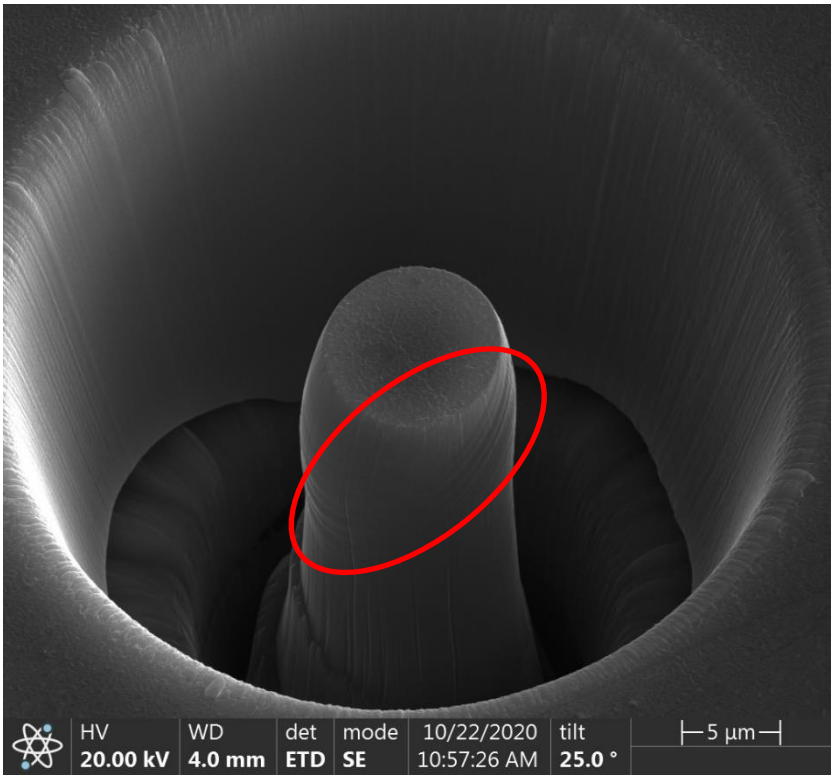


Figure 75 SEM image of an as-compressed pillar from the peak aged Mg-6Sn-3Zn alloy. The slip traces of the $\frac{1}{3}\langle 11\bar{2}0\rangle(0001)_{Mg}$ slip system can clearly be seen in the image and are marked with a red ellipse.

Stress-strain curves from the pillars compressed along $[\bar{1}8\bar{7}\bar{6}]_{Mg}$ and $[25\bar{7}6]_{Mg}$ are shown in Figure 76 and Figure 77 respectively. Large strain bursts are not observed for this alloy, although smaller strain bursts are distributed throughout the stress-strain curves. Differently from the Mg-6Sn and Mg-6Sn-3Al pillars, the Mg-6Sn-3Zn pillars exhibit strong work hardening, which could be an indication of strong dislocation-precipitate interaction during the compression process.

The mean yield stress determined by the 0.2% proof stress is 64.86MPa, leading to the as-calculated average CRSS being 29.92MPa. The Mg-6Sn-3Zn alloy thus exhibits the highest resistance to basal a slip of all three Mg-Sn alloys, probably because of the large number of prismatic Mg_2Sn and c-axis $MgZn_2$ precipitates.

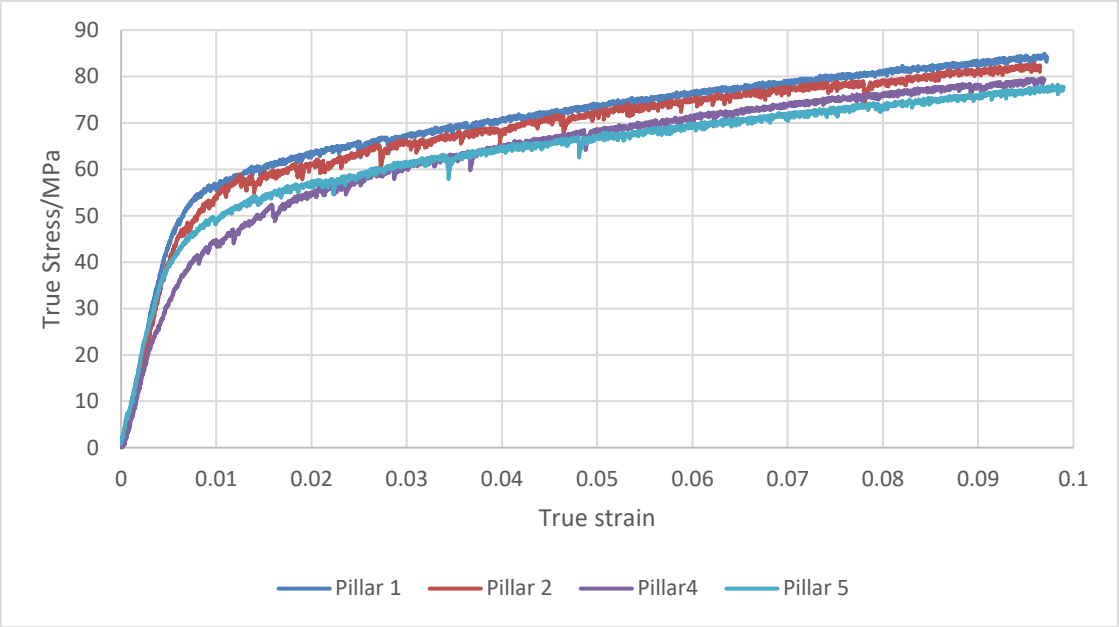


Figure 76 Stress-strain curves obtained from as-compressed pillars of peak aged Mg-6Sn-3Zn alloy with a loading direction of $[\bar{1}8\bar{7}\bar{6}]_{Mg}$

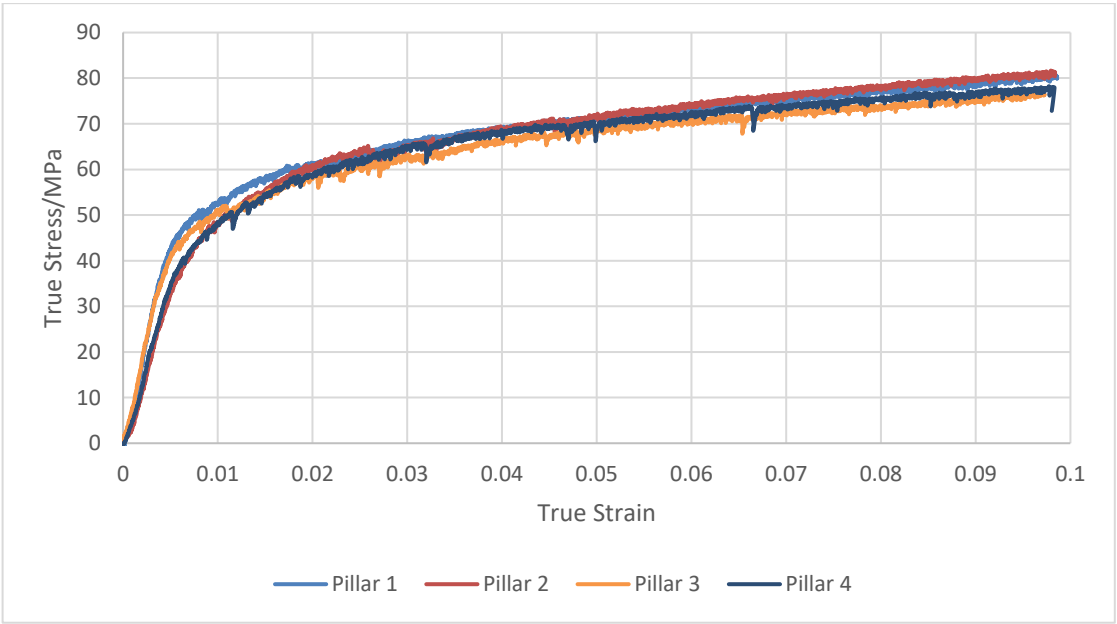


Figure 77 Stress-strain curves obtained from as-compressed pillars of peak aged Mg-6Sn-3Zn alloy with a loading direction of $[25\bar{7}6]_{Mg}$

6.5.2 Dislocation analysis of the Mg-6Sn-3Zn pillars compressed along $[25\bar{7}6]_{Mg}$

A TEM foil has been fabricated from a pillar compressed along $[25\bar{7}6]_{Mg}$. The image of the pillar is shown below in Figure 78, with the dashed line marking the TEM foil lift out region. For this specific sample, the TEM foil normal is $[1\bar{1}00]_{Mg}$.

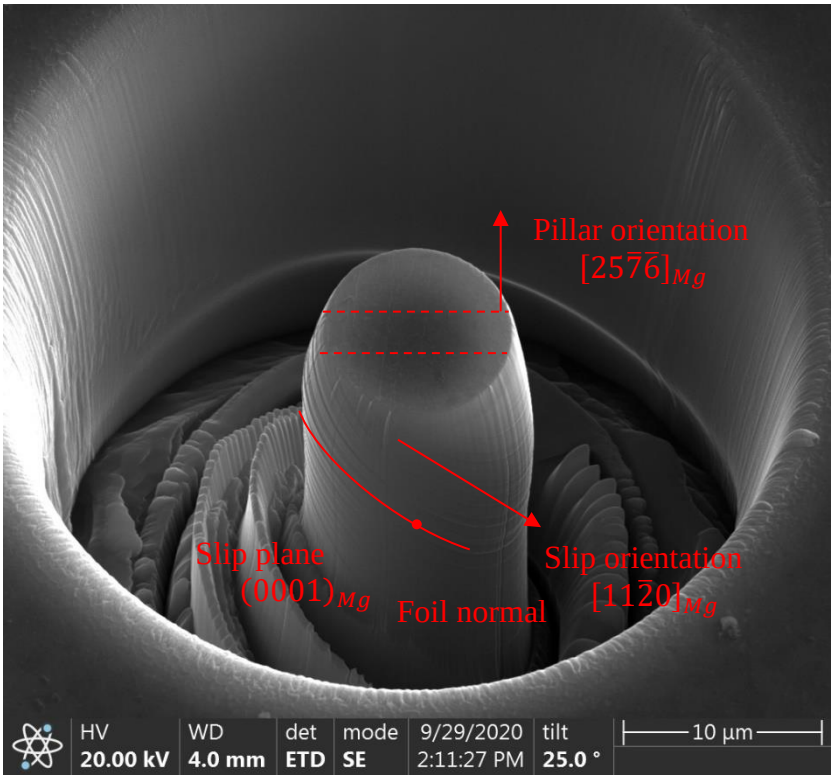


Figure 78 Pillar 2 with a $[\bar{1}8\bar{7}\bar{6}]_{Mg}$ loading direction, with the TEM foil lift out marked by the red dashed line

When imaged with a beam direction of $[1\bar{1}00]_{Mg}$, with $g = 0002$, as shown below in Figure 79, no dislocations can be observed with this imaging condition, so $g \cdot b = 0$. By changing the g vector to $g = 11\bar{2}0$, the dislocations became visible as shown in Figure 80. All dislocations were edged-on under this image condition. Therefore, these dislocations can also be confirmed being basal a dislocations. The magnification of the images is slightly lower than that for Mg-6Sn and Mg-6Sn-3Al to show the sheared precipitates in the as-compressed

sample. As can be clearly seen from the images, the rod like $MgZn_2$ precipitates with long axis along the $[0001]_{Mg}$ direction have been sheared. These precipitates tend to be straight and aligned along the $[0001]_{Mg}$ direction, as shown previously in Section 5.4.3. This indicates a different type of precipitate-dislocation interaction during the compression. In addition, no other types of dislocations were found in the TEM samples, indicating that basal a slip is the only slip system activated. Only the c-axis $MgZn_2$ rods shear; no precipitates shearing is observed for the basal and prismatic Mg_2Sn precipitates.

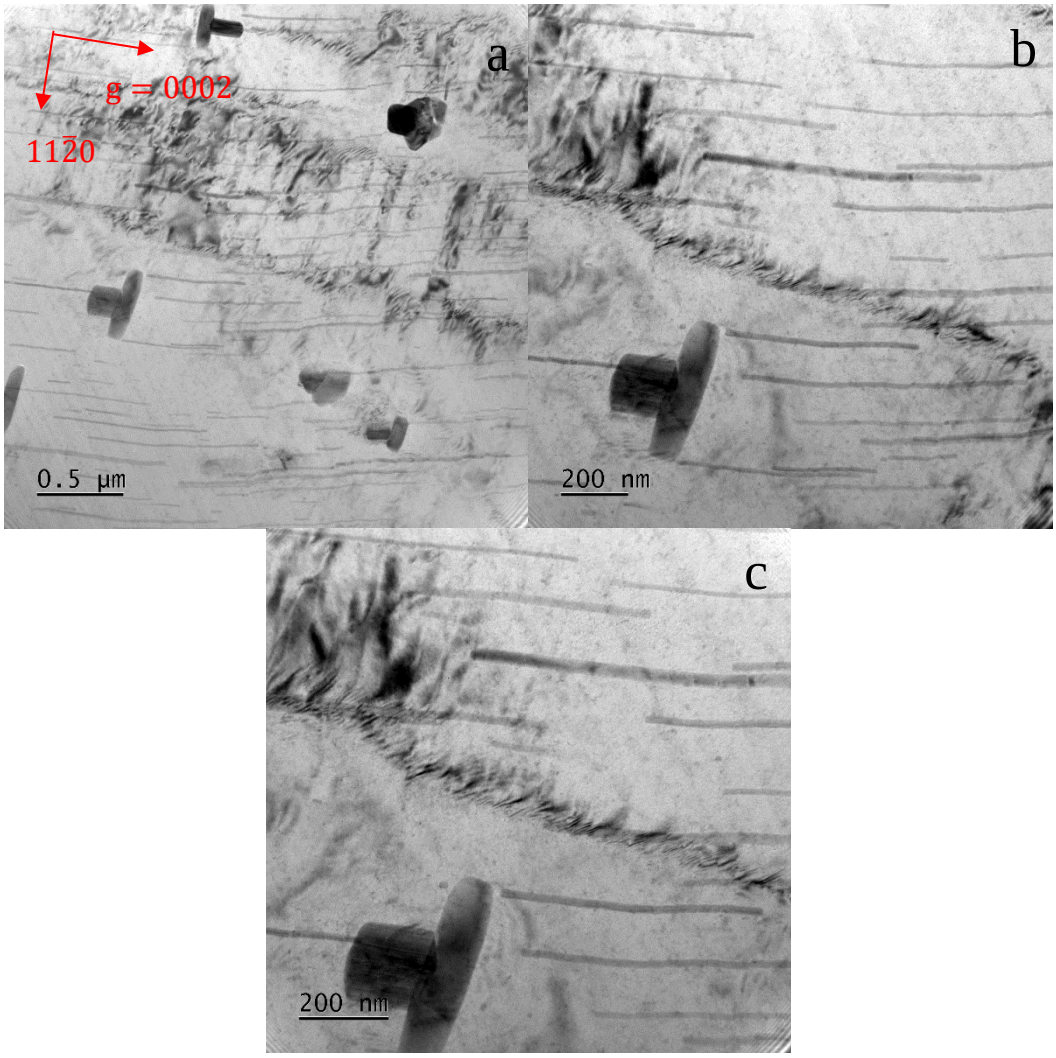


Figure 79 TEM images of a TEM foil from a Mg-6Sn-3Zn pillar compressed along $[25\bar{7}6]_{Mg}$, viewed along $[1\bar{1}00]_{Mg}$ with g = 0002. (a) low magnification, (b) medium magnification, (c) high magnification

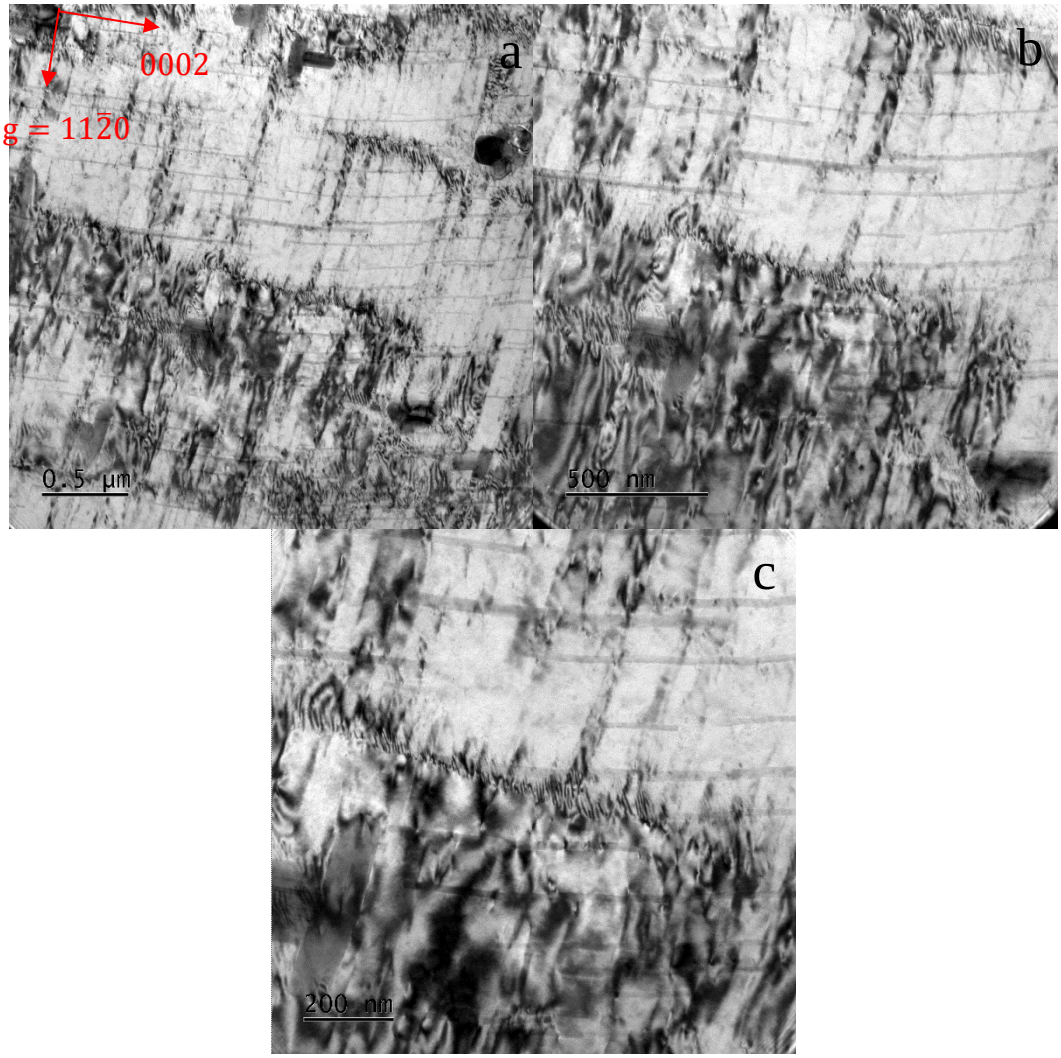


Figure 80 TEM images of a TEM foil from a Mg-6Sn-3Zn pillar compressed along $[25\bar{7}6]_{Mg}$, viewed along $[1\bar{1}00]_{Mg}$ with g = 11$\bar{2}$0. (a) low magnification, (b) medium magnification, (c) high magnification

To show the sheared $MgZn_2$ precipitates more clearly, TEM images were taken and shown below in Figure 81 with a g vector of g = 0002 showing no dislocations. Another image shown in Figure 82 has a g vector of g = 11$\bar{2}$0 making the dislocations visible. The dislocations are marked with the dashed line and can be clearly seen to have presumably sheared through the precipitates.

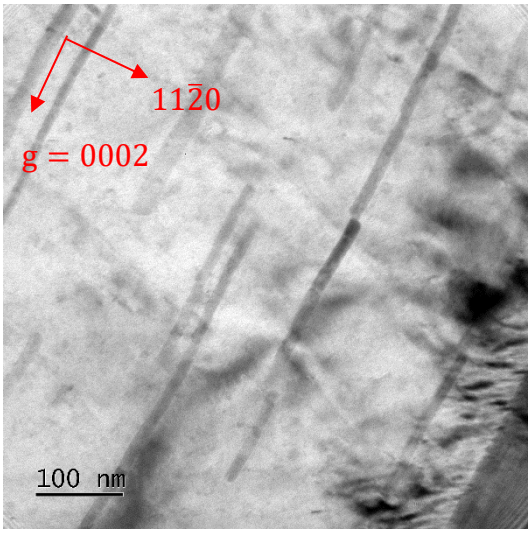


Figure 81 TEM images of sheared c-axis $MgZn_2$ precipitates viewed along $[1\bar{1}00]_{Mg}$ with $g = 0002$.

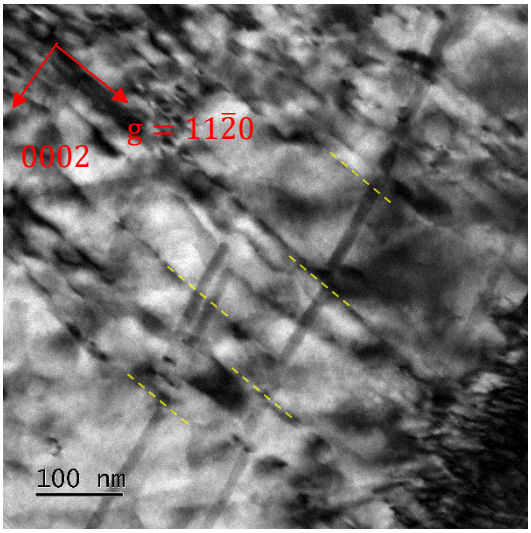


Figure 82 TEM images of sheared c-axis $MgZn_2$ precipitates viewed along $[1\bar{1}00]_{Mg}$ with $g = 11\bar{2}0$. Dislocations are visible and have passed through the precipitates as marked by the dashed lines.

6.6 Summary

As explained above, the three Mg-Sn alloys in this study display quite different deformation behaviour due to their different precipitate distributions. Having a basal precipitate dominated microstructure, the Mg-6Sn alloy exhibit the lowest resistance towards basal slip, while the Mg-6Sn-3Al alloy shows better performance under the same loading due to the presence of pyramidal and c-axis precipitates. The highest resistance towards basal slip is shown by the Mg-6Sn-3Zn alloy, not only due to prismatic Mg_2Sn and c-axis $MgZn_2$ wide rods but also very fine and homogeneously distributed c-axis $MgZn_2$ narrow rods.

For the Mg-6Sn and Mg-6Sn-3Al alloys, the main interaction mechanism between basal dislocations and precipitates is Orowan looping. However, on using a series of imaging conditions, Orowan loops were not observed in the alloy. This does not mean Orowan looping has not taken place. A simulation study by Vaid *et al.* suggests that Orowan loops may collapse into the matrix-precipitate boundary and therefore disappear [82]. This indicates that dislocations may eliminate on specific interphase boundaries. For the Mg-6Sn-3Zn alloys, the dislocation-precipitate interaction mechanism includes Orowan looping and shearing.

Currently, there is no existing research that have quantitatively analysed the basal slip behaviour in alloys with multiple precipitate types, especially in the Mg-Sn system. Luo *et al.* studied the effect of Al/Zn ratio in a Mg-3Sn (wt.%) system, but their experiment was based on macro-scale tensile testing and did not investigate any specific slip behaviour[83]. Wan *et al.* improved the number of prismatic laths by a twinning-detwinning approach in Mg-5Sn (wt.%), although the mechanical property measurements are still based on macro-scale testing. It would be useful to determine the exact contributions of the different precipitates in Mg-Sn alloys and this will be described in the next chapter.

7 Orowan strengthening in Mg-Sn alloys

7.1 Introduction

In Mg-Sn alloys, with a variety of precipitates of different morphology and orientation, their contribution to strength will also be different. Non-basal precipitates will have a better capability for blocking basal slip and therefore providing more strength. However, this cannot be confirmed by the above-mentioned pillar compression experiment, as the slip behaviour does not demonstrate the strengthening effect of different precipitates. In order to quantitatively analyse the effect of non-basal precipitates on basal slip, the well-established Orowan strengthening model is applied here. In this chapter, the strengthening effect of different types of precipitates will be calculated and discussed.

7.2 Derivation of suitable parameters for Orowan strengthening

7.2.1 Orowan equations for different precipitate types

As previously mentioned in Section 2.4.3, the general equation for Orowan strengthening is as follows:

$$\sigma_{Orowan} = \frac{Gb}{2\pi\sqrt{1-\nu}}\frac{1}{\lambda}\ln\left(\frac{d_p}{r_0}\right) \qquad \text{Equation 7-1}$$

It can clearly be seen from the equation that for a certain alloy system and slip system, the mean particle spacing λ and the mean particle diameter d_p are the only two factors that matter. The question then becomes the determination of λ and d_p.

A list of abbreviations and symbols used in these calculations appears below in Table 15.

Table 15 List of abbreviations and symbols used to analyse Orowan strengthening

G	Shear modulus of Magnesium, taken as 16GPa
b	Burger's vector of basal a dislocation, taken as 0.32nm
ν	Poisson's ratio of Magnesium, taken as 0.33
λ	Mean edge-to-edge particle spacing between precipitates
d_p	Mean effective particle diameter for a spherical precipitate. The intersection circle will have an average diameter of $d_p = \frac{\pi d_t}{4}$
d_t	Mean particle diameter measured from experiments
t_p	Mean effective particle thickness
t_t	Mean particle thickness measured from experiments
r_0	Cut-off radius of dislocations, normally taken equal to b
N_L	Linear precipitate density
N_A	Area precipitate density
f	Volume fraction of precipitates
S_p	Effective cross-section area of precipitates

Following Nie[66], suitable forms of λ and d_p based on the precipitate types that exist in Mg-Sn alloys will be presented. To start with, the mean particle spacing for spherical particles is:

$$\lambda = L_p - d_p \qquad \text{Equation 7-2}$$

where L_p is the mean centre-to-centre spacing between particles (but also referred to as σ by Underwood[84]). Here,

$$L_p = \frac{1}{N_L} \qquad \text{Equation 7-3}$$

where N_L is the linear precipitate density and equals the square root of the area particle density N_A, $N_A = {}^{f}/_{S_P}$, where S_p is the average planar cross-section area of the particles. In addition, this will need to be multiplied by the closest hexagonal close packing unit length 1.075, as it is assumed that the particles in Mg-Sn alloys are arranged in a triangular pattern[85]. Assuming A is the area that a particle occupies and equals to a_0^2, r_0 is the nearest neighbour distance, then

$$A = \frac{r_0^2\sqrt{3}}{2} = a_0^2 \qquad \text{Equation 7-4}$$

$$r_0 = \frac{a_0\sqrt{2}}{\sqrt[4]{3}} = 1.075\, a_0 \qquad \text{Equation 7-5}$$

Therefore:

$$\lambda = L_p - d_p = \frac{1.075}{\sqrt{N_A}} - \frac{\pi d_t}{4} = \left(\frac{0.779}{\sqrt{f}} - 0.785\right) d_t \qquad \text{Equation 7-6}$$

as in Table 10. An illustration of the particle arrangement and the relationship between λ, L_p and d_p is shown below in Figure 83.

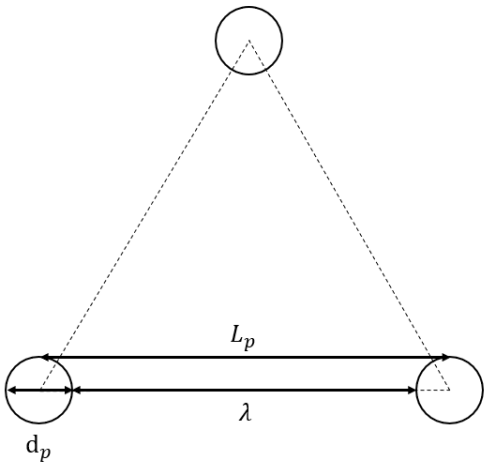


Figure 83 Illustration of spherical precipitates in a triangular array and the respective relationship between λ, L_p and d_p

Substituting the above λ into the Orowan equation then gives

$$\sigma_{Orowan} = \frac{Gb}{2\pi\sqrt{1-\nu}\left(\frac{0.779}{\sqrt{f}}-0.785\right)d_t}\ln\frac{0.785d_t}{b} \qquad \text{Equation 7-7}$$

This relationship can then be easily expanded to the circumstance of triangularly arranged prismatic plates and c-axis rods. For the prismatic plates, S_p is affected by not only d_p but also plate thickness t_p, as is illustrated below in Figure 84. Therefore, the mean particle spacing for prismatic plates will be

$$\lambda = L_p - \frac{d_p}{2} - \frac{\sqrt{3}t_p}{2} = 0.825\sqrt{\frac{d_t t_t}{f}} - 0.393d_t - 0.866t_t \text{Equation 7-8}$$

It's respective form of Orowan equation will then be

$$\sigma_{Orowan} = \frac{Gb}{2\pi\sqrt{1-\nu}\left(0.825\sqrt{\frac{d_t t_t}{f}}-0.393d_t-0.866t_t\right)}\ln\frac{0.886\sqrt{d_t t_t}}{b}\text{Equation 7-9}$$

For the spherical basal plates and c-axis rod precipitates, as the precipitates have a uniform circular cross-section on the basal plane, with an identical arrangement of precipitates to that in Figure 83, the mean particle spacing for these two types of precipitates will simply be

$$\lambda = L_p - d_p = \left(\frac{0.953}{\sqrt{f}} - 1\right) d_t \qquad \text{Equation 7-10}$$

Its respective form of the Orowan equation will then be

$$\sigma_{Orowan} = \frac{Gb}{2\pi\sqrt{1-\nu}\left(\frac{0.953}{\sqrt{f}}-1\right)d_t} \ln\frac{d_t}{b} \qquad \text{Equation 7-11}$$

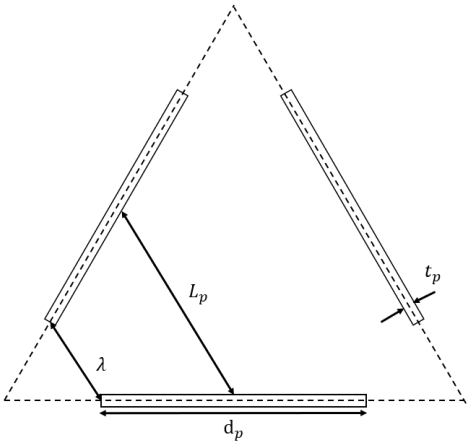


Figure 84 Illustration of prismatic plate precipitates in a triangular array and the relationship between λ, L_p, d_p and t_p

7.2.2 Fitting precipitate dimensions to Orowan equations

From the above derivation, it appears clear that if the Orowan equation is to be applied to calculate the strengthening effect of different precipitates, the key parameters which need to be determined will be d_t, t_t and f. The precipitates in the three Mg-Sn alloys studied in this work will now be discussed.

We first consider the lath-shaped and plate-shaped basal precipitates in the Mg-Sn alloys. As shown above, for simplicity of calculation, a basal lath or plate will be replaced by the equivalent circular basal plate with the same area, as illustrated in the figure below.

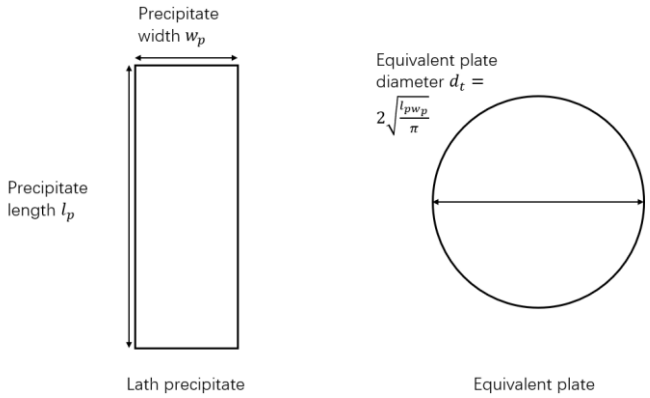


Figure 85 Illustration showing the relationship between a basal lath and an equivalent basal plate

The mean precipitate length l_p (note that l_p is different from L_p) and mean precipitate width w_p can be measured by TEM observations; the equivalent plate diameter $d_t = 2\sqrt{\frac{l_p w_p}{\pi}}$.

For the basal rods, prismatic and pyramidal laths, as they have a rectangular cross-section on the basal plane while $d_t \gg t_t$, the illustration in Figure 84 can then be directly applied. The mean precipitate length l_p (directly equivalent to d_t as the length is constant for a lath) and mean precipitate thickness t_t can be measured using TEM.

For the c-axis rod precipitates, the illustration in Figure 83 is directly applied, as these precipitates have a near-circular intercept with the basal plane. The mean cross-sectional diameter of the precipitates d_t can be measured by TEM.

Thus, all the precipitate dimensions required for the Orowan strengthening analysis can be acquired by TEM. The numerical frequencies of the different precipitates will also be counted. The dimensions measured for the various precipitates are listed in the table below:

Table 16 List of dimensions measured for Orowan strengthening calculations

Alloy	**Precipitate type**	**Dimension**
Mg-6Sn	Type 1 basal lath	Length, width, thickness
	Type 2 basal lath	Length, width, thickness
Mg-6Sn-3Al	Type 3 basal rod	Length, diameter
	Type 4 basal plate	Length, width, thickness
	Type 5 c-axis rod	Length, diameter
	Type 6 pyramidal lath	Length, width, thickness
Mg-6Sn-3Zn	Type 2 basal lath	Length, width, thickness
	Type 7 prismatic lath	Length, width, thickness
	$MgZn_2$ wide rod	Length, diameter
	$MgZn_2$ narrow rod	Length, diameter

The detailed statistics of these dimensions are listed below in a series of tables and figures. The sample size used for the statistics is 100 for common precipitates and 50 for uncommon precipitates.

For the precipitates in Mg-6Sn:

Table 17 Dimensions and numeric percentages measured for the precipitates in Mg-6Sn

Precipitate type	**Dimension**	**Average value/μm**	**Standard deviation**	**Numerical percentage**
Type 1 basal lath	Length	0.888	0.27	21.70%
	Width	0.076	0.02	
	Thickness	0.059	0.01	
Type 2 basal lath	Length	0.700	0.17	78.30%

	Width	0.140	0.01	
	Thickness	0.069	0.02	

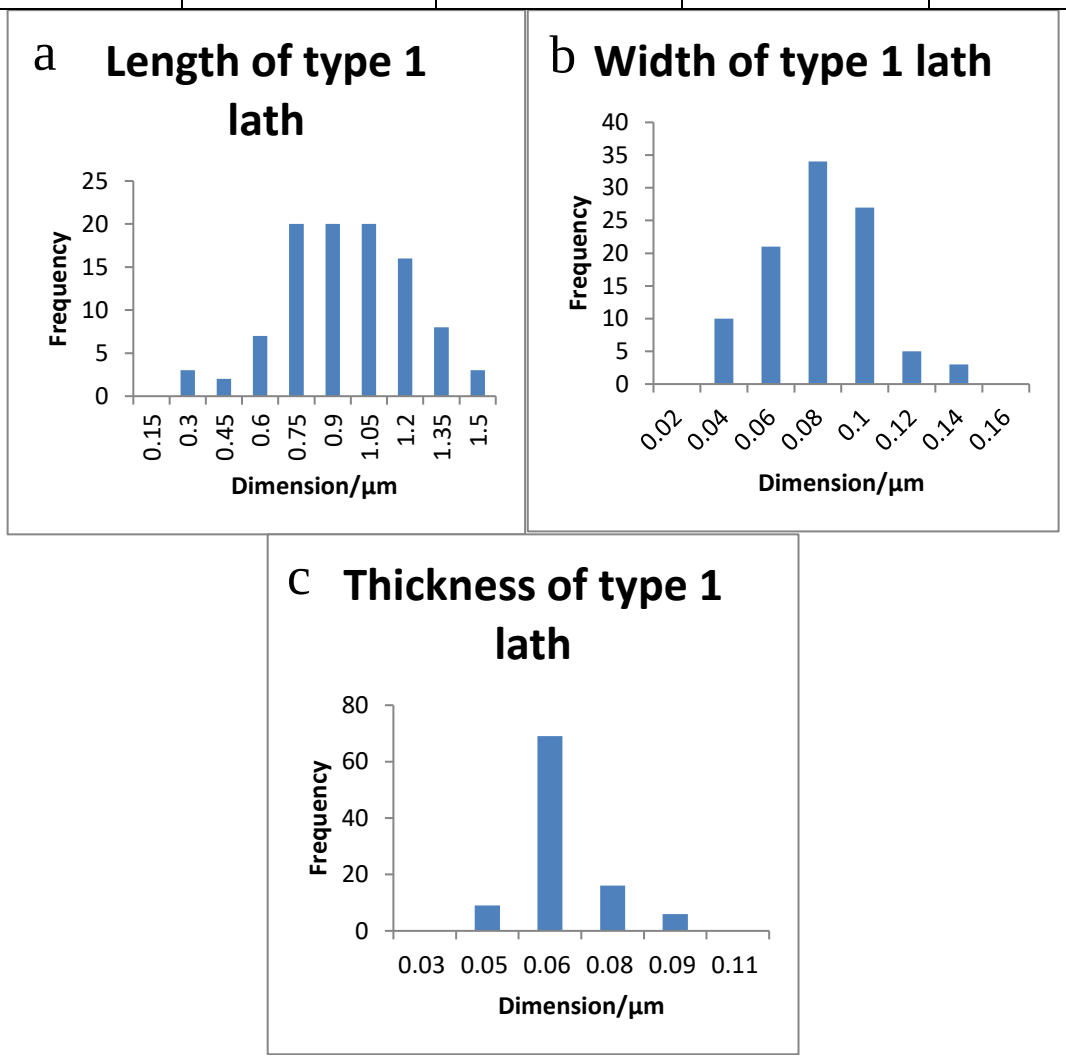


Figure 86 Dimensions of Type 1 basal laths shown as a histogram. (a) length, (b) width, (c) thickness

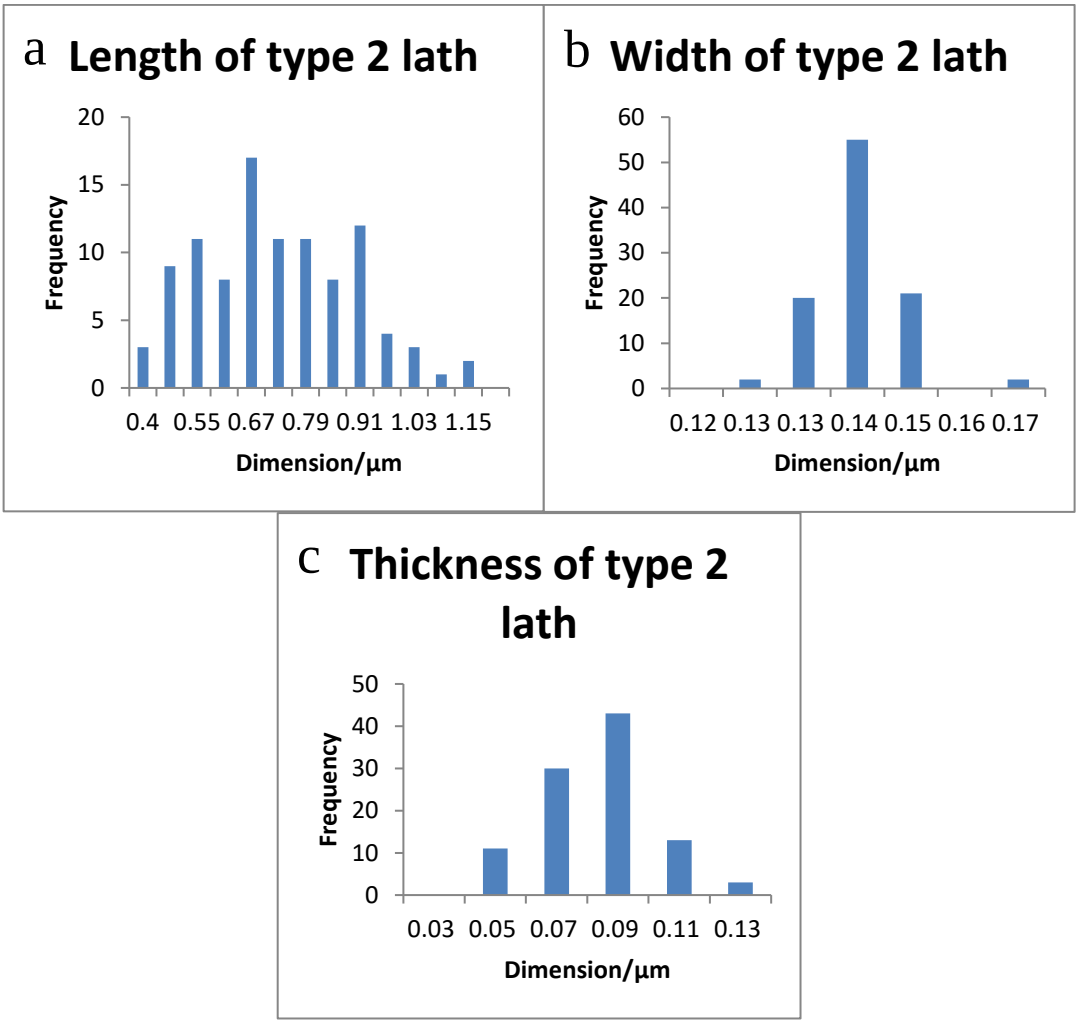


Figure 87 Dimensions of Type 2 basal laths shown as a histogram. (a) length, (b) width, (c) thickness

For the precipitates in Mg-6Sn-3Al:

Table 18 Dimensions and numerical percentages measured for the precipitates in Mg-6Sn-3Al

Precipitate type	**Dimension**	**Value/µm**	**Standard deviation**	**Numeric percentage**
Type 3 basal rod	Length	1.131	0.28	48.10%
	Diameter	0.039	0.01	
Type 4 basal plate	Length	0.188	0.05	37.80%

	Width	0.118	0.04	
	Thickness	0.071	0.02	
Type 5 c-axis rod	Length	0.245	0.08	6.50%
	Diameter	0.072	0.02	
Type 6 pyramidal lath	Length	1.241	0.20	7.60%
	Width	0.169	0.07	
	Thickness	0.041	0.01	

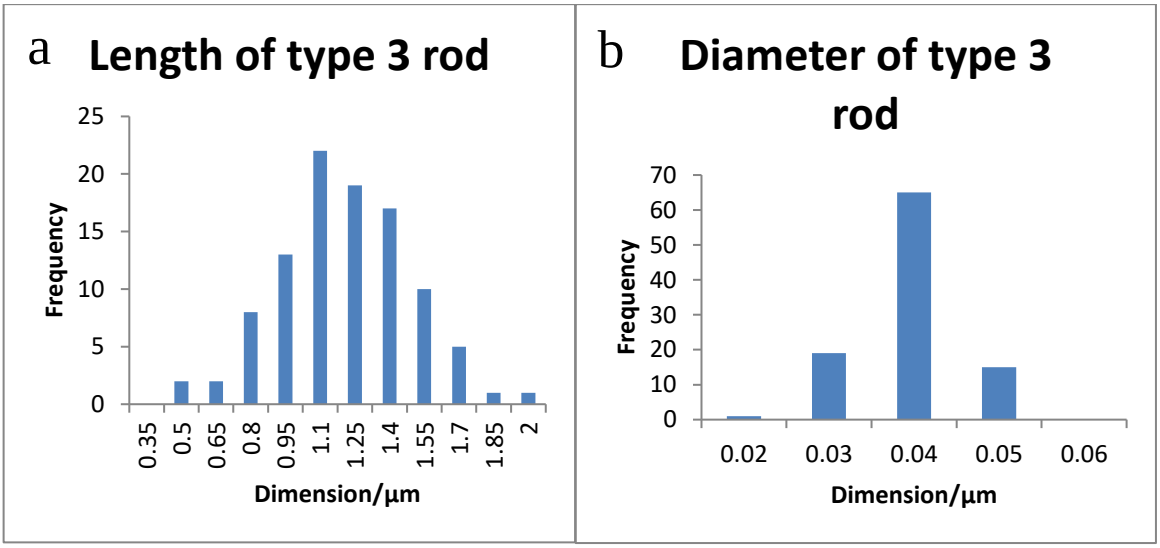


Figure 88 Dimensions of Type 3 basal rods shown as a histogram. (a) length, (b) diameter

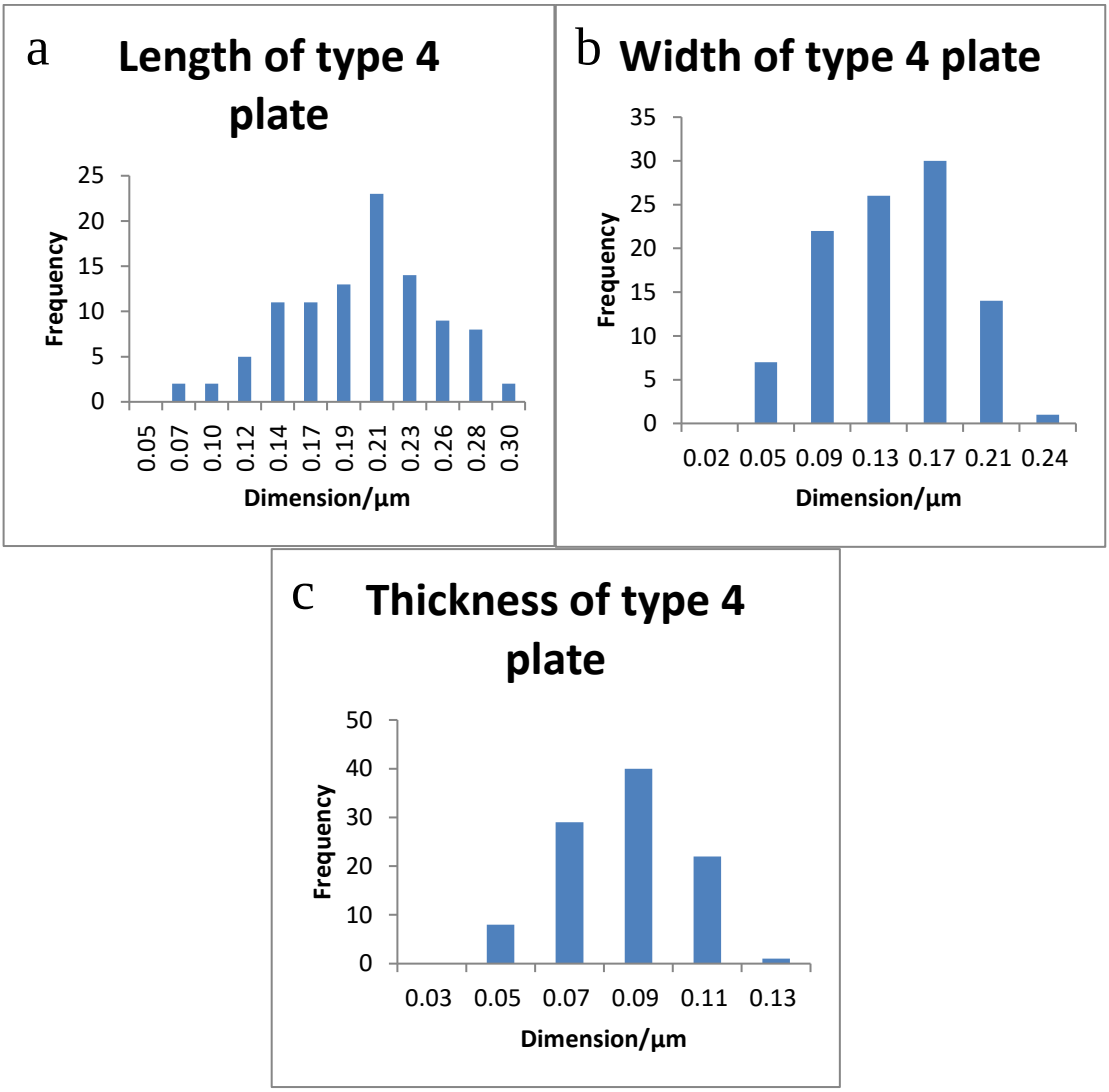


Figure 89 Dimensions of Type 4 basal plates shown as a histogram. (a) length, (b) width, (c) thickness

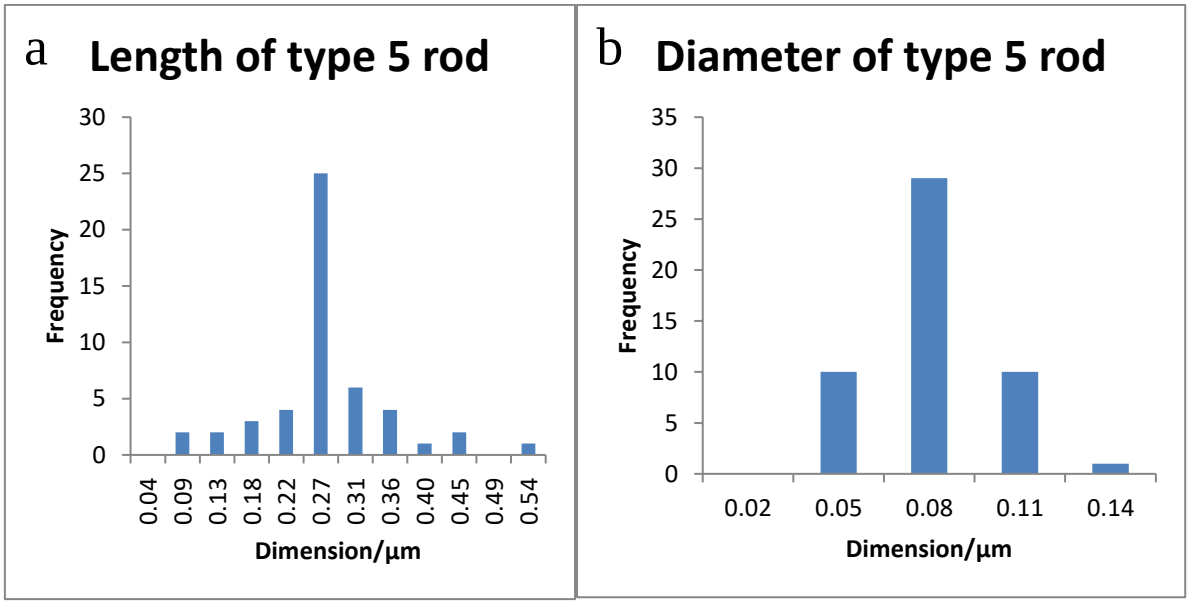


Figure 90 Dimensions of Type 5 c-axis rods shown as a histogram. (a) length, (b) diameter

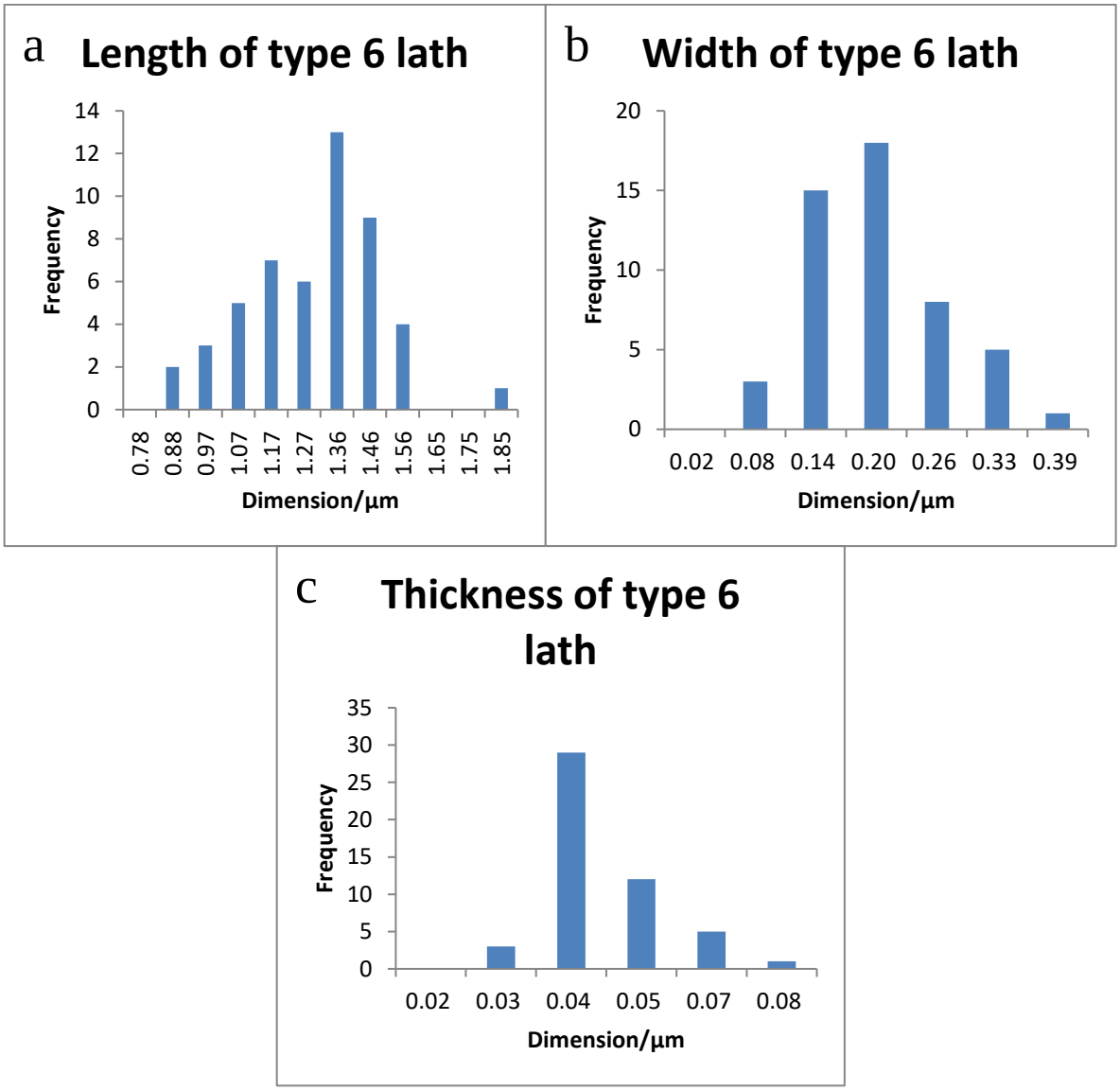


Figure 91 Dimensions of Type 6 pyramidal laths shown as a histogram. (a) length, (b) width, (c) thickness

For the precipitates in Mg-6Sn-3Zn:

Table 19 Dimensions and numeric percentages measured for the precipitates in Mg-6Sn-3Zn. Narrow $MgZn_2$ rods are excluded as they do not participate in Orowan looping

Precipitate type	**Dimension**	**Value/μm**	**Standard deviation**	**Numeric percentage**	**Numeric percentage without**

					$MgZn_2$ narrow rods
Type 2 lath	Length	0.391	0.08	10.50%	48.83%
	Width	0.136	0.03		
	Thickness	0.050	0.01		
Type 7 lath	Length	0.705	0.08	2.30%	10.70%
	Width	0.129	0.02		
	Thickness	0.079	0.02		
$MgZn_2$ wide rod	Length	0.322	0.12	8.70%	40.47%
	Diameter	0.070	0.02		
$MgZn_2$ narrow rod	Length	0.681	0.22	78.60%	
	Diameter	0.013	0.01		

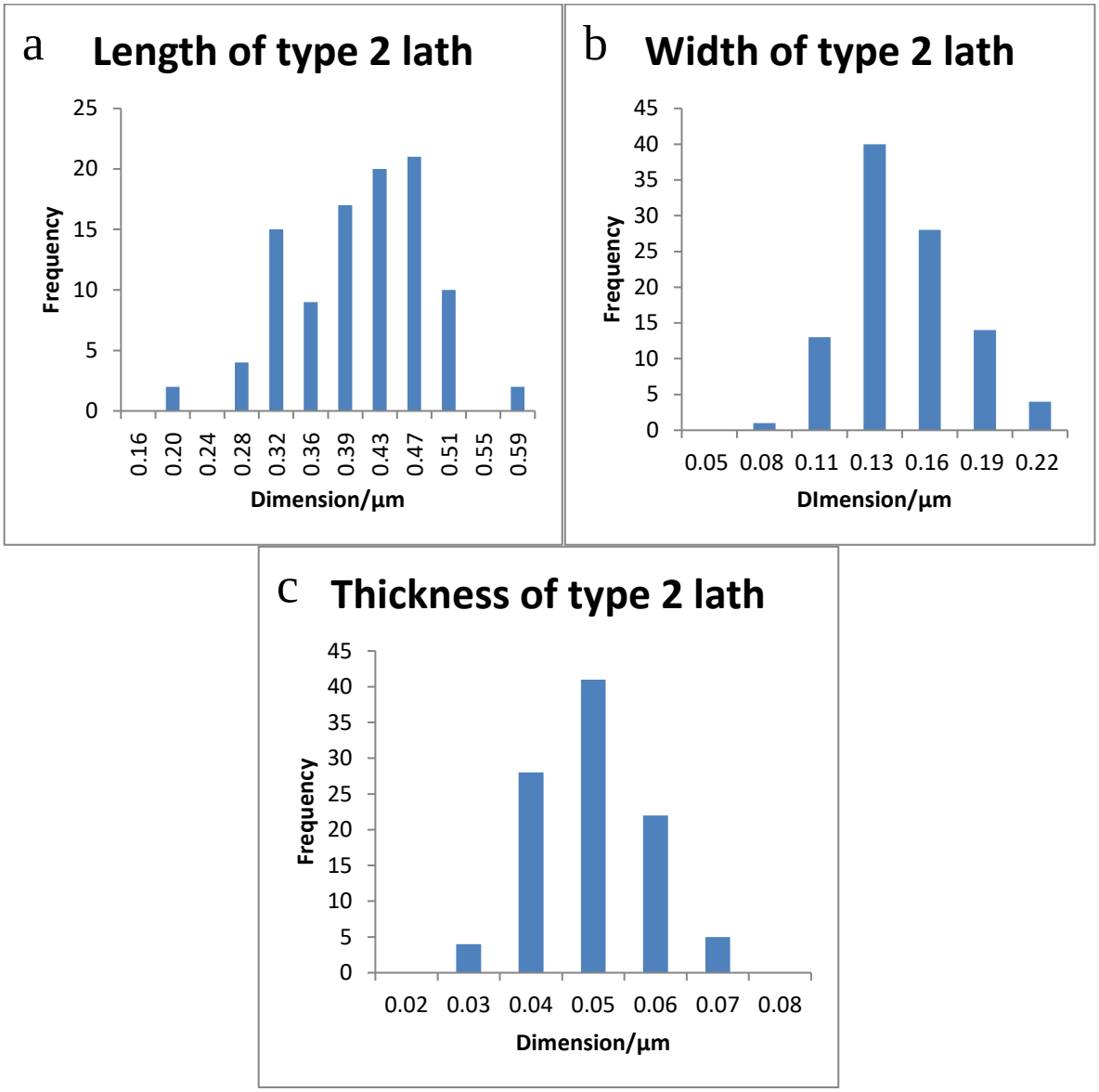


Figure 92 Dimensions of Type 2 basal laths (in Mg-6Sn-3Zn) shown as a histogram. (a) length, (b) width, (c) thickness

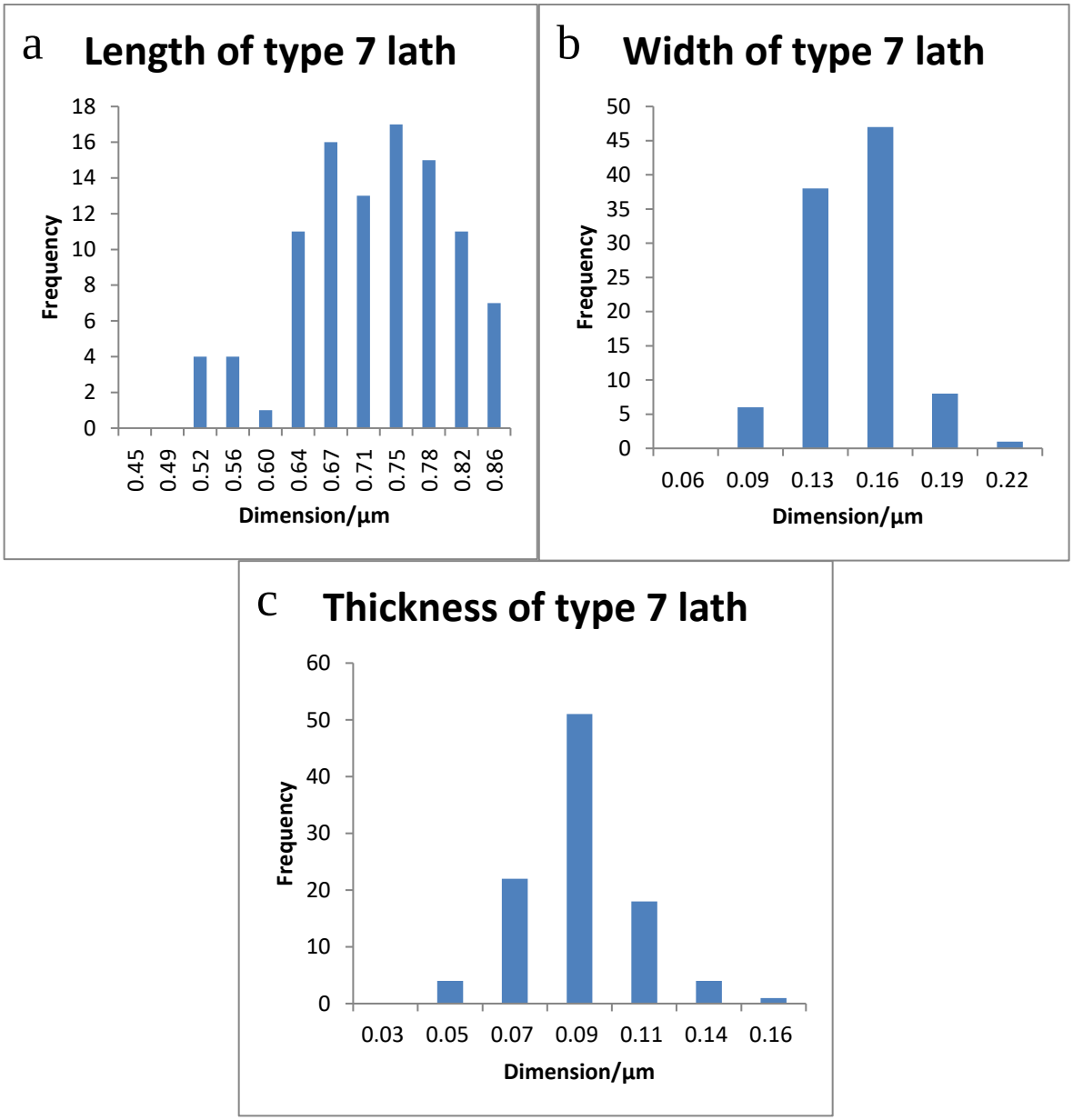


Figure 93 Dimensions of Type 7 prismatic laths shown as a histogram. (a) length, (b) width, (c) thickness

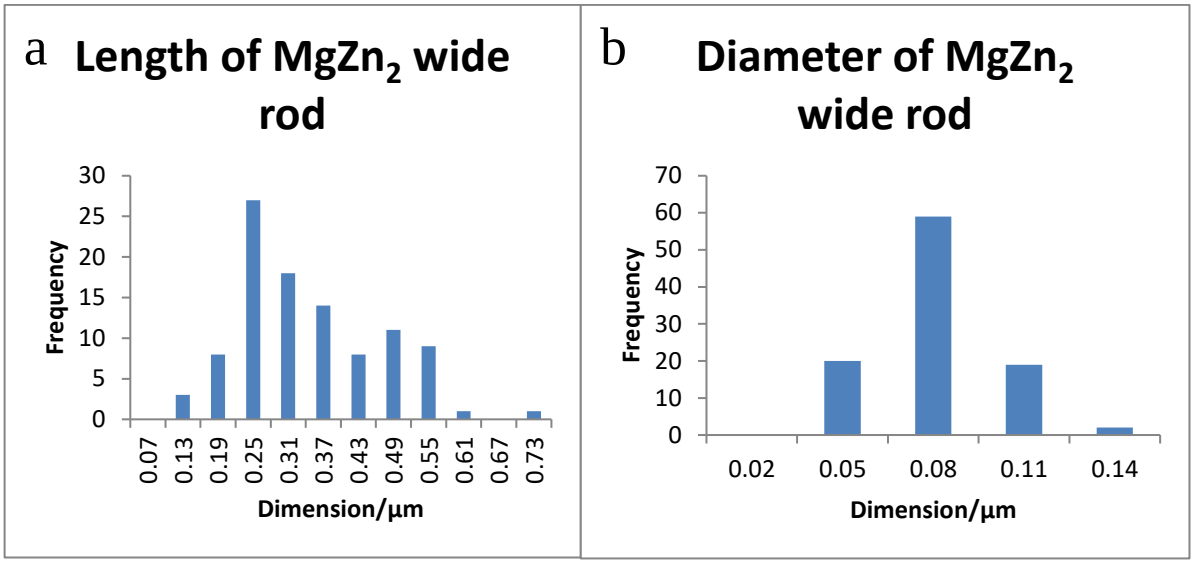


Figure 94 Dimensions of $MgZn_2$ c-axis wide rods shown as a histogram. (a) length, (b) diameter

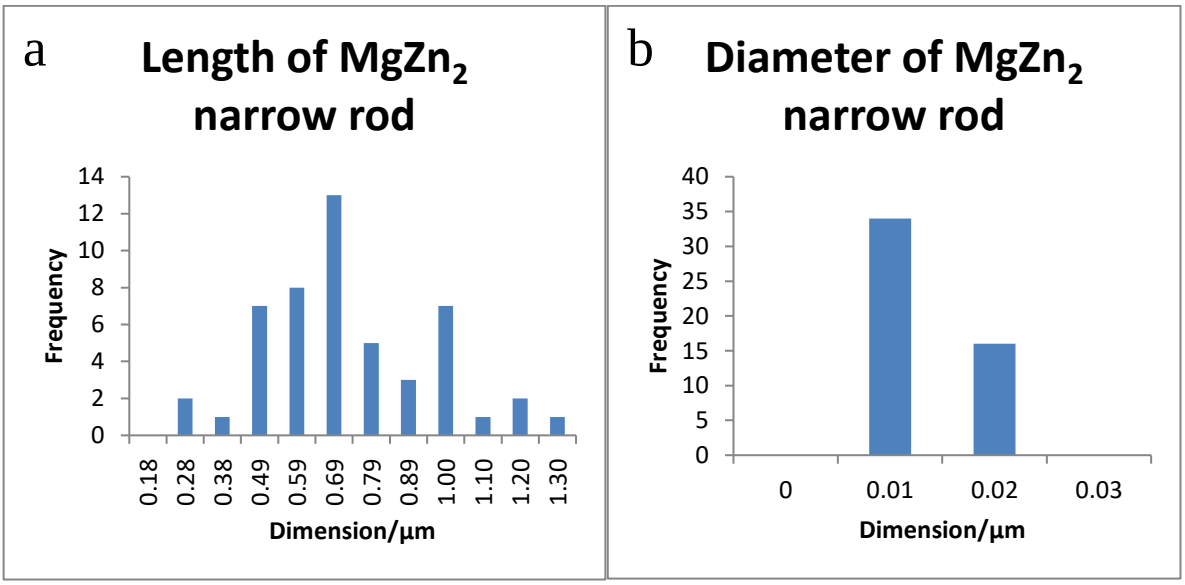


Figure 95 Dimensions of $MgZn_2$ c-axis narrow rods shown as a histogram. (a) length, (b) diameter

As can be seen from the histograms, the distribution of precipitate dimensions seems similar to normal. These statistics will then be applied to the analysis of Orowan strengthening. In addition, based on the dimensions and numerical ratios measured above, an

average volume of precipitates in different Mg-Sn alloys can then be calculated for further volume fraction measurements. The as-calculated average volumes for different alloys are listed in Table 20.

Table 20 Average precipitate volumes calculated using the measured precipitate dimensions and numerical ratios. $MgZn_2$ narrow rods are excluded as they do not participate in Orowan looping.

Alloy	**Average precipitate volume/μm^3**
Mg-6Sn	$6.33*10^{-3}$
Mg-6Sn-3Al	$2.03*10^{-3}$
Mg-6Sn-3Zn	$2.45*10^{-3}$ (excluding $MgZn_2$ narrow rods)

7.2.3 Determination of volume fraction

The volume fractions of different precipitates are estimated via the following approach. Based on the statistics of the precipitates, an average precipitate volume can be acquired. This average precipitate volume will then be multiplied by the precipitate number density measured from TEM to get the volume fraction. Convergent Beam Electron Diffraction (CBED) is applied here to estimate the TEM sample thickness.

The figure below shows an example of the determination of TEM sample thickness by CBED. 3 CBED patterns were taken across the sample to ensure the accuracy of the measurement. The thickness measurement results and the as-measured number densities (both volume and area) are shown below in Table 21.

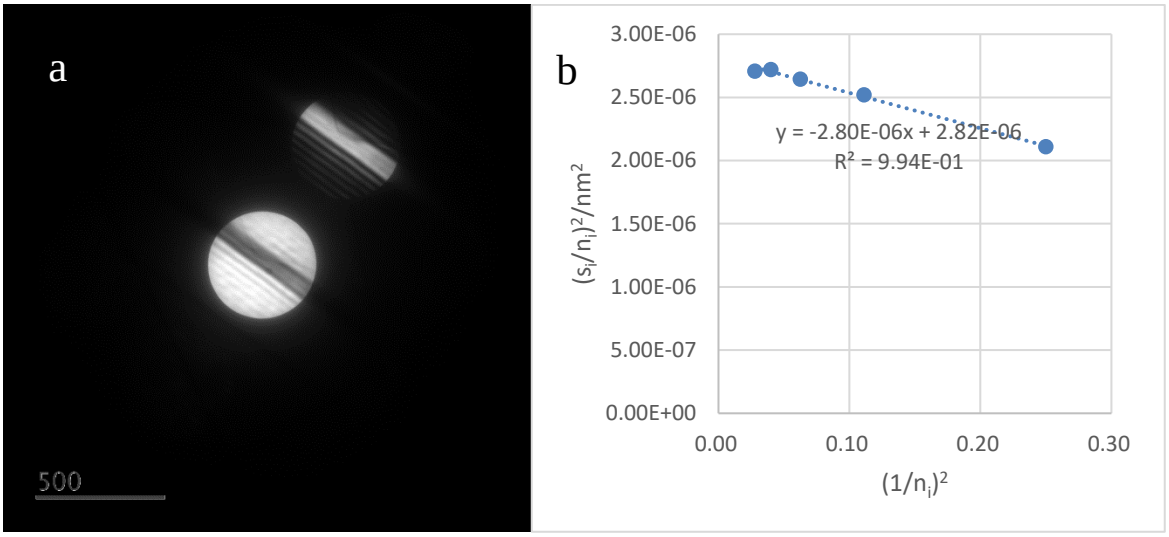


Figure 96 (a) A CBED pattern taken from the Mg-6Sn-3Zn sample to measure the sample thickness, (b) plot of s^2/n^2 over $1/n^2$. Interception on the y axis equals $1/t^2$

Table 21 Sample thickness, volume number density and area number density measured from different Mg-6Sn alloy samples

Sample	**Thickness**	**Volume number density**	**Area number density**
Mg-6Sn	448nm	14.14/μm^3	5.85/μm^2
Mg-6Sn-3Al	401nm	31.26/μm^3	9.92/μm^2
Mg-6Sn-3Zn	587nm	37.66/μm^3	11.22/μm^2

Therefore, based on the number densities and average precipitate volume measured above, the volume fractions for different alloys, as well as their respective different precipitate types are as listed in Table 22.

Table 22 Respective volume fraction of different precipitate types in Mg-Sn alloys

Alloy	**Precipitate type**	**Volume fraction**
Mg-6Sn		8.95%

	Type 1 basal lath	1.46%
	Type 2 basal lath	7.49%
Mg-6Sn-3Al		6.33%
	Type 3 basal rod	2.15%
	Type 4 basal plate	1.89%
	Type 5 c-axis rod	0.19%
	Type 6 pyramidal lath	2.10%
Mg-6Sn-3Zn		9.23%
	Type 2 basal lath	4.54%
	Type 7 prismatic lath	2.72%
	$MgZn_2$ wide rod	1.30%
	$MgZn_2$ narrow rod	0.67%

7.2.4 Calculation of Orowan strengthening

With the mean particle spacing and volume fraction determined for each alloy and precipitate type, the Orowan strengthening effect of the precipitates in Mg-Sn alloys can then be determined. Research on Mg alloys mentioned previously attempted to estimate the Orowan strengthening behaviour [67], [68], [70], [86]–[88].

These papers are based on alloys that have only one precipitate type and cannot be directly applied to the Mg-Sn system. Therefore, it is important to consider that Orowan looping effect takes place around all the types of precipitate in these Mg-Sn alloys. A simple approach is to use the respective volume fractions of the different types of precipitates to calculate their

respective contribution to the strength and then to sum these. In this case, the strengthening contribution of a certain precipitate type is

$$\sigma_i = \sigma(d_i, \lambda_i) = \frac{Gb}{2\pi\sqrt{1-\nu}} \frac{1}{\lambda_i} \ln\left(\frac{d_i}{r_0}\right) \qquad \text{Equation 7-12}$$

and hence the total contribution of all precipitate types will then simply be

$$\sigma_{Orowan} = \sum_{i=1}^{n} \sigma(d_i, \lambda_i) = \sum_{i=1}^{n} \frac{Gb}{2\pi\sqrt{1-\nu}} \frac{1}{\lambda_i} \ln\left(\frac{d_i}{r_0}\right) \quad \text{Equation 7-13}$$

However, one cannot calculate the strengthening caused by the different types of precipitates in one alloy and then sum them, as this does not reflect the actual interaction between the different precipitate types and is closer to treating different precipitate as different strengthening mechanisms. For a Mg-Sn alloy with multiple precipitate types, a model is proposed here.

Firstly, as a dislocation may interact with different precipitate types at a time, it is reasonable to use the total volume fraction of all precipitates in a specific Mg-Sn alloy, as this reflects the actual spacing between precipitates, regardless of their morphology.

It is then assumed that a certain type of precipitate, when considering its contribution in isolation, contributes to the Orowan strengthening behaviour such that

$$\sigma_i = \sigma(d_i) = \frac{Gb}{2\pi\sqrt{1-\nu}} \frac{1}{\lambda} \ln\left(\frac{d_i}{r_0}\right) \qquad \text{Equation 7-14}$$

With more than one type of precipitate present, the contribution of a specific precipitate type is then determined by its respective fraction in the alloy, where

$$\sigma_i = \sigma(d_i, f_i) = \frac{f_i}{f} \frac{Gb}{2\pi\sqrt{1-\nu}} \frac{1}{\lambda} \ln\left(\frac{d_i}{r_0}\right) \qquad \text{Equation 7-15}$$

Therefore, the total contribution of all precipitate types in a certain alloy will be

$$\sigma_{Orowan} = \sum_{i=1}^{n} \sigma(d_i, f_i) = \sum_{i=1}^{n} \frac{f_i}{f} \frac{Gb}{2\pi\sqrt{1-\nu}} \frac{1}{\lambda} \ln\left(\frac{d_i}{r_0}\right) \quad \text{Equation 7-16}$$

This approach determines the mean particle spacing in a proper manner, and then weights the contribution of different precipitates by their respective fraction. This provides an accurate determination of the Orowan strengthening effect in the Mg-Sn alloy system and can be applied to any similar alloy with multiple precipitate species.

This approach is still not perfect as some aspects were omitted for simplicity. For example, it is assumed that looping and shearing does not occur on a dislocation at the same time, however this is possible in the real case. When looping and shearing takes place simultaneously on a dislocation, the tension on the dislocation will be affected by both effects and thus resulting in a much more complex situation. The method proposed above can still be improved, however, for the scope of this particular study, all aspects within the author's power have been included. Therefore, this approach has been considered rational.

Based on the approach described above, the respective contributions of the different precipitate types to Orowan strengthening can then be calculated. Using the precipitate dimensions measured and listed in Table 16, the strength increments contributed by the respective precipitate types are as listed in Table 23.

Table 23 Orowan strengthening contribution of different precipitate types in Mg-Sn alloys

Alloy	**Precipitate type**	**Volume fraction/%**	**Strength contribution/MPa**
Mg-6Sn			
	Type 1	1.46%	0.59
	Type 2	7.49%	7.32
	Total	8.95%	7.91
	Experimental		13.22
Mg-6Sn-3Al			

	Type 3	2.15%	5.69
	Type 4	1.89%	3.79
	Type 5	0.19%	0.49
	Type 6	2.10%	5.65
	Total	6.33%	15.62
	Experimental		21.34
Mg-6Sn-3Zn			
	Type 2	4.54%	6.26
	Type 7	2.72%	4.24
	$MgZn_2$ rod	1.30%	2.75
	Total	8.56%	13.25
	Experimental		29.92

The Orowan strengthening contributions to the Mg-6Sn and Mg-6Sn-3Al alloys are around 75% of that of the CRSS measured from experiments. This is due to the strength of pure Mg and the strength from solid solution strengthening not being included in the calculation. For the Mg-6Sn-3Zn alloy, the as-calculated strengthening is around half that of the actual CRSS. Despite the strength contributions from pure Mg and solid solution strengthening, the strength from the shearing of the very fine $MgZn_2$ narrow rods is not included. In order to accurately estimate the total strength contribution of the Mg-Sn alloys, these effects need to be considered and quantified.

7.2.5 Total strengthening effect in Mg-Sn alloys

As previously mentioned, the base strength of pure Mg, the solid solution strengthening effect and the shearing strength of $MgZn_2$ narrow rods have to be included for an accurate estimate of the total strength.

For solid solution strengthening, a widely applied approach was described by Caceres and Rovera, mentioned previously in Section 2.4.2 [43], where the contribution of solid solution strengthening is

$$\sigma_{sss} = \mathrm{m}B_n c^n \quad \text{Equation 2-3}$$

where: m is the Taylor factor, B_n is the solid solution strengthening rate depending on the alloy system and c the solute atomic concentration in the matrix.

Previous reports have established different solid strengthening rates with respect to solute concentration for Sn, Al and Zn in Mg alloys. An early study by Akhtar and Teghtsoonian suggests that the values respectively for constants ½ and 2/3, are 24.3MPa and 40.0MPa for Sn, 21.2MPa and 39.5MPa for Al and 19.7MPa and 43.2MPa for Zn[89]. Caceres and Rovera used a Taylor factor of 5 for Al solute in Mg and acquired a 197MPa strengthening rate with constant 2/3 [43]. Shi *et al.* used a Taylor factor of 5.5 for Sn solute in Mg and acquired 286MPa for 2/3 and 192.5MPa for ½ [42].

However, these estimates are designed for a bulk sample and do not reflect the actual situation of a specific slip system. Currently, very few papers have attempted to determine the contribution to a specific slip system. Akhtar and Teghtsoonian evaluated the effects of a couple of solute elements on basal slip, including Zn, but the approach is less well defined than in recent research[18]. A much more recent study by Tehranchi *et al.* evaluated the effect from the aspect of solute-dislocation interaction energy and estimated a 3MPa increment from a 1.63% Al addition and a 1.6MPa increment from a 0.45% Zn addition [90]. Based on this evaluation,

the strengthening rate derived for basal slip would be 12MPa for Al addition and 10MPa for Zn addition. Hence for simplicity, as these values are around 1/4 of that of the bulk sample, the strengthening rates used in this study will be: 13MPa for Sn, 9.9MPa for Al and 10.8MPa for Zn. A constant of 2/3 will be applied to keep consistency with other existing studies. In addition, it is assumed that there is no cooperation between different alloying elements.

The matrix chemical compositions of the three peak aged Mg-Sn alloys have been measured by STEM-EDS and are shown in the figure below.

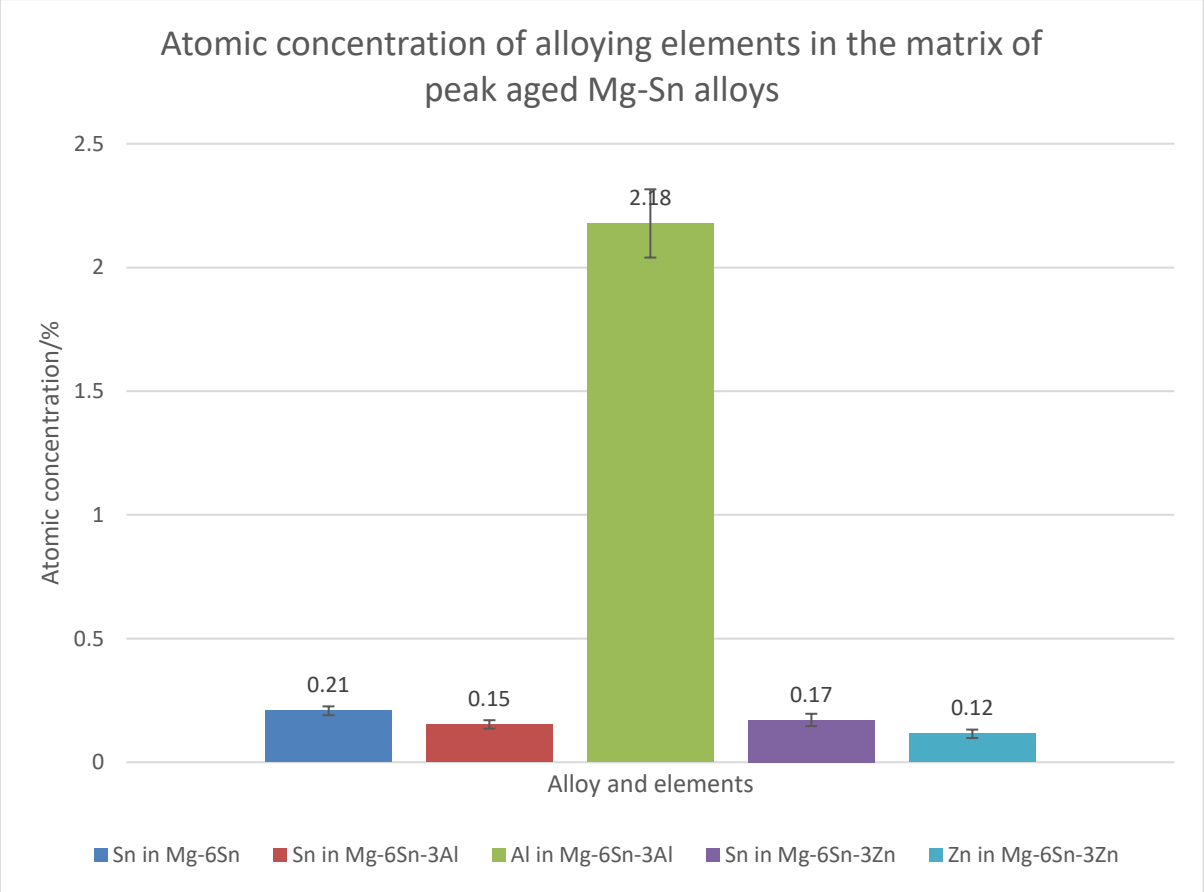


Figure 97 Atomic concentration of alloying elements in the matrix of peak aged Mg-Sn alloys measured by STEM-EDS

Based on these matrix compositions, the contributions of solid solution strengthening by the various solute elements in the three Mg-Sn alloys can then be calculated and are listed in the table below.

Table 24 Contribution to basal slip CRSS from solid solution strengthening in Mg-Sn alloys

Solid solution strengthening contribution	**Mg-6Sn/MPa**	**Mg-6Sn-3Al/MPa**	**Mg-6Sn-3Zn/MPa**
Sn	1.66	1.49	1.55
Al		2.77	
Zn			1.18
Total	1.66	4.26	2.73

For the shearing stress provided by the $MgZn_2$ narrow rods, the total strengthening effect is contributed by the energy required to produce an anti-phase boundary (APB), the energy required to produce the new interface after shearing, the coherency strain introduced in this process and the modulus effect. In addition, it is generally accepted that interface creation, coherency strain and the modulus effect do not contribute a large amount towards the shear strengthening by particles[91]–[94]. Therefore, for the shearing of $MgZn_2$ narrow rods, only the contribution from the creation of the APB is here considered, for simplicity. The APB energy of the $MgZn_2$ precipitate is currently not well known. From a few existing studies in the Mg-Y-Gd system, the APB energy of the β series precipitates ranges from 130mJ/m^2 to 250mJ/m^2 [95], [96]. Hence an APB energy of 200 mJ/m^2 will be applied here for a rough estimate. An equation by Schuh to calculate the contribution of APB towards shear strength is given below[97]:

$$\Delta\tau_{APB} = \frac{\pi}{2b}\gamma_{APB}f \qquad \text{Equation 7-17}$$

where b is the magnitude of the Burgers vector, γ_{APB} is the APB energy and f is the volume fraction of the $MgZn_2$ narrow rods. The contribution of the shearing of the $MgZn_2$ narrow rods can then be calculated as 6.57MPa.

Therefore, based on all the calculations above, a combined strength contribution to the basal slip in Mg-Sn alloys can be estimated and is listed in the table below. The base CRSS of basal slip in pure Mg used here is 2MPa according to existing literature [17], [18], [89], [98].

Table 25 Total strength of basal slip in Mg-Sn alloys contributed by different strengthening mechanisms

Strengthening mechanism	**Mg-6Sn/MPa**	**Mg-6Sn-3Al/MPa**	**Mg-6Sn-3Zn/MPa**
Base strength	2		
Solid solution strengthening	1.66	4.26	2.73
Orowan strengthening	7.91	15.62	13.25
Particle shearing strengthening			6.57
Total	11.57	21.88	24.55
Experimental	13.22	21.34	29.92

It can be seen from the results that for Mg-6Sn and Mg-6Sn-3Al, the as-estimated strength has an adequate agreement with the experimentally measured strength. For the Mg-6Sn-3Zn

alloy, the as-estimated strength is slightly lower than that of the actual strength. This could possibly be due to the work hardening effect and is discussed later (in Section 8.4).

7.3 Summary

To estimate the contribution of different strengthening behaviours in three Mg-Sn alloys, strengthening mechanisms including Orowan strengthening, particle shearing strengthening and solid solution strengthening towards the CRSS of basal slip in these alloys have been evaluated.

For the Orowan strengthening, an estimate based on the equation developed by Nie has been modified to fit the complex precipitate morphologies and precipitate types in Mg-Sn alloys. Contributing more than half of the CRSS towards basal slip, Orowan strengthening plays the most important role in strengthening the Mg-Sn alloys. A universal model has been proposed here to evaluate a complex precipitate strengthened alloy system like Mg-Sn. The results indicate that non-basal precipitates contribute more to unit strength than the basal precipitates. The as-estimated results provide an adequate prediction of the Orowan strengthening behaviour contributed by multiple precipitate types.

The gap between the strengthen contributed by Orowan strengthening is filled by solid solution strengthening. Despite the Mg-6Sn-3Zn which contains a shearing strengthening mechanism, the strength of other alloys agrees well with the experimentally measured CRSS. For the Mg-6Sn-3Zn alloy, the effect of $MgZn_2$ narrow rods shearing strengthening has been roughly estimated by the contribution of the formation of anti-phase boundaries during shearing. With all strengthening mechanisms included, there are still some gap between the estimated value and the experimentally measured value in the Mg-6Sn-3Zn alloy. This will be discussed later in Section 8.4.

8 Discussion

8.1 List of results

The results presented in Chapter 5, 6 and 7 are summarised as follows:

The chemistry, morphology, crystallography and dimension statistics of all precipitate types in the Mg-Sn alloys have been analysed. The precipitate types, along with their morphologies and orientation relationships, are listed in the table below.

Table 26 Precipitate types and their respective morphologies and ORs in the Mg-Sn alloys

Alloy	**Precipitate type**	**Morphology**	**OR**
Mg-6Sn			
	Type 1	Basal lath with long axis along $\langle 11\bar{2}0\rangle_{Mg}$	$(0001)_{Mg}$ $\parallel (110)_{Mg2Sn}, [11\bar{2}0]_{Mg}$ $\parallel [001]_{Mg2Sn}$
	Type 2	Basal lath with long axis along $\langle 10\bar{1}0\rangle_{Mg}$	$(0001)_{Mg}$ $\parallel (110)_{Mg2Sn}, [2\bar{1}\bar{1}0]_{Mg}$ $\parallel [1\bar{1}1]_{Mg2Sn}$
Mg-6Sn-3Al			
	Type 3	Basal rod with long axis along $\langle 11\bar{2}0\rangle_{Mg}$	$(0001)_{Mg}$ $\parallel (111)_{Mg2Sn}, [11\bar{2}0]_{Mg}$ $\parallel [1\bar{1}0]_{Mg2Sn}$
	Type 4	Basal plate	
	Type 5	C-axis rod	

	Type 6	Pyramidal lath with a habit plane of $(1\bar{1}01)_{Mg}$	No specific OR
Mg-6Sn-3Zn			
	Type 2	Basal lath with long axis along $\langle 10\bar{1}0\rangle_{Mg}$	$(0001)_{Mg}$ $\parallel (110)_{Mg2Sn}, [2\bar{1}\bar{1}0]_{Mg}$ $\parallel [1\bar{1}1]_{Mg2Sn}$
	Type 7	Prismatic lath with long axis along $\langle 11\bar{2}0\rangle_{Mg}$	$(0001)_{Mg}$ $\parallel (110)_{Mg2Sn}, [11\bar{2}0]_{Mg}$ $\parallel [001]_{Mg2Sn}$
	$MgZn_2$ wide rod	C-axis rod	$(0001)_{Mg}$ $\parallel (11\bar{2}0)_{MgZn2}, [11\bar{2}0]_{Mg}$ $\parallel [10\bar{1}0]_{MgZn2}$
	$MgZn_2$ narrow rod	C-axis rod	

Micro-pillar compression tests designed for basal slip have determined the CRSS values of basal slip in three Mg-Sn alloys. Basal a slip is the only slip system activated in all three Mg-Sn alloys.

With a modification to the Orowan strengthening equation, the theoretical CRSSs of basal slip in all three Mg-Sn alloys have been calculated and agree adequately with experimentally measured values.

8.2 Precipitation in Mg-Sn alloys

With the TEM results acquired in Chapter 5, the precipitation behaviour of the three Mg-Sn alloys is discussed here.

For the Mg-6Sn binary alloy, two types of basal precipitates were identified. After the initial report by Henes & Gerold[8] and van der Planken[56], only a few papers have reported on the basal precipitates in binary Mg-Sn alloys[7], [48]. The morphologies and orientation relationships in this study agree with the existing literature.

Four types of Mg_2Sn precipitates were identified in the Mg-6Sn-3Al ternary alloy. Excepting the Type 6 pyramidal laths, all other precipitate types have the same orientation relationship, which is $(0001)_{Mg} \parallel (111)_{Mg2Sn}, [11\bar{2}0]_{Mg} \parallel [1\bar{1}0]_{Mg2Sn}$, which agrees with existing studies[7]. As regards the pyramidal precipitates, although they have been reported by several studies[5], [7], [51], [54] and also in this work, no-one has identified a specific orientation relationship or habit plane. Therefore, predictions are made that the pyramidal Mg_2Sn laths may have a varied range of orientation relationships and habit planes.

The addition of 3 wt.% Zn in this study caused the formation of Type 2 basal and Type 7 prismatic Mg_2Sn precipitates, along with wide and narrow $MgZn_2$ c-axis rods. In some other Mg-Sn alloys with different Zn concentration, however, the effect of Zn is quite different. Chen *et al.* reported the segregation of Zn to the Mg-Mg_2Sn interphase boundary in a Mg-9.8Sn-1.2Zn (wt.%) alloy leading to pyramidal Mg_2Sn precipitates[57]. No independent precipitates of Zn exist in the alloy. With the same alloy composition, Sasaki *et al.* also reported the presence of pyramidal and prismatic Mg_2Sn precipitates and no independent precipitates of Zn[49]. In another study by Sasaki *et al.*, $MgZn_2$ c-axis rods appears in a Mg-9.3Sn-2.5Zn-0.2Mn (wt.%) alloy[59]. In a Mg-6Sn-3Zn alloy exactly identical to this study, Mendis *et al.* reported the presence of pyramidal Mg_2Sn precipitates while only very little $MgZn_2$ precipitates were found[5]. The results from existing studies and this study indicate that the effect of Zn in the Mg-Sn alloy system is very subtle and subject to change with factors including alloy composition and experimental conditions.

8.3 Precipitate shearing in Mg-6Sn-3Zn alloys

It is generally accepted that the boundary between Orowan looping and precipitate shearing is determined by a critical particle size: larger than the critical size and dislocation tend to form a loop around the particles, smaller than the critical size and the dislocations shear through the particles [99]. Currently, there are no experimental measurements of this critical size in Mg alloys. Hutchinson estimated the critical size by balancing the stress introduced by a bowed dislocation around the precipitate bent to a specific radius (normally taken as precipitate size) R. Hence, the equation mentioned previously in Section 2.4.3 can be acquired:

$$\frac{G_m b}{R} = \frac{G_p}{15} \qquad \text{Equation 2-4}$$

Based on this equation, the critical size of the $Mg_{17}Al_{12}$ precipitates between shearing and looping is estimated to be around 3nm [32]. For the Mg_2Sn precipitates in an Mg matrix, the critical size for particle shearing is 3.14nm. For the $MgZn_2$ precipitates in an Mg matrix, the critical size for particle shearing is 2.74nm. Therefore, it is expected that all the precipitates in the three Mg-Sn alloys investigated here will not be sheared during the motion of basal a dislocations as the precipitates are much larger than the critical value.

However, the actual experimental observations show exactly the opposite for the $MgZn_2$ precipitates. Most of the $MgZn_2$ narrow rods were sheared, as shown previously in Figure 81. The Mg_2Sn precipitates, on the other hand, are not sheared. By measuring the distance that the precipitates have sheared, it can be estimated that ~150 dislocations glide through each $MgZn_2$ precipitate after 10% compression. An example of such a distance measurement can be found below in Figure 98.

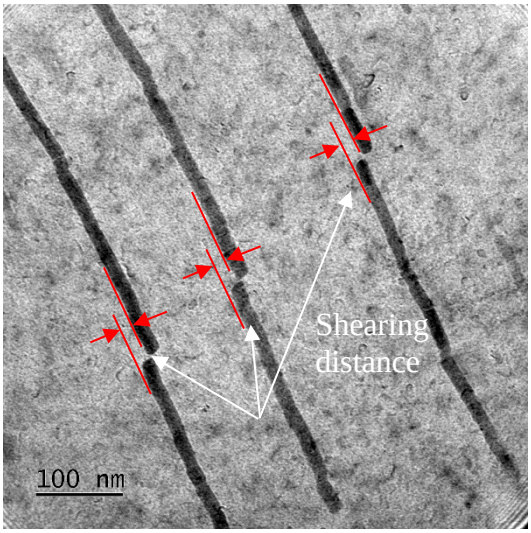


Figure 98 Image showing the measurement of shear distance; the number of dislocations which have passed through the precipitates can be calculated as the average shear distance divided by the magnitude of Burgers vector of the dislocations

Some recent studies also suggest that dislocations have sheared through precipitates that are obviously larger than the estimated critical size. Liao *et al.* predicted by computational modelling that the $Mg_{17}Al_{12}$ precipitates in AZ91 can be sheared by prismatic dislocations [100]. Cepeda-Jemenez reported shearing of precipitates in AZ91 and Mg-11Nd (wt.%) alloys after tensile strain [101]. Solomon *et al.* reported that β' precipitates in Mg-Y alloys can be sheared by both basal a slip and c + a slip, while β''' precipitates in Mg-Nd alloys can be sheared only by basal a slip [102].A pillar compression study by Wang and Stanford reported the same $MgZn_2$ shearing behaviour in a Mg-5Zn (wt.%) alloy and suggested that the shearing behaviour is probably due to good lattice parameter matching [103].

To explain the precipitate shearing, the overall precipitation procedure is reviewed here: at the beginning of precipitation, a structure which is rich in solute atoms, but maintaining the same crystal structure as the matrix will occur. These are called G.P. zones [14]. The G.P. zone then develops into a phase with a new crystal structure and will begin to grow larger.

During this process, the coherency of the precipitate-matrix interface will begin gradually to be destroyed. Due to the similarity of microstructures of matrix and precipitate in the early stages of precipitation, certain dislocations tend to shear through the particles. When the size of the new particle exceeds a critical value, the remaining coherency of the interface will not sustain dislocation shearing, which will therefore transfer to Orowan looping.

Hence, the essence of the transition from shearing to looping is in fact determined by the coherency of the interphase boundary. For the $MgZn_2$ precipitates in Mg-Sn alloys, the orientation relationship determined in this work is $[0001]_{Mg} \parallel [1\bar{2}10]_{MgZn2}$, $[10\bar{1}0]_{Mg} \parallel [0001]_{MgZn2}$, $[11\bar{2}0]_{Mg} \parallel [10\bar{1}0]_{MgZn2}$. On the $(1\bar{1}00)_{Mg} - (0001)_{MgZn2}$ interphase boundary, $[11\bar{2}0]_{Mg} \parallel [10\bar{1}0]_{MgZn2}$. Regarding the lattice parameter, there seems to be a large mismatch between the atomic distance of $[11\bar{2}0]_{Mg}$ (3.19Å) and $[10\bar{1}0]_{MgZn2}$ (9.09Å). An image illustrating the orientation relationship between the Mg matrix and $MgZn_2$ precipitates viewed along $[0001]_{Mg} \parallel [1\bar{2}10]_{MgZn2}$ has been constructed using Crystalmaker and is shown below in Figure 99, where the Mg matrix is marked with the red rectangle and the $MgZn_2$ precipitate is marked with the green rectangle. The interface is marked with the blue rectangle.

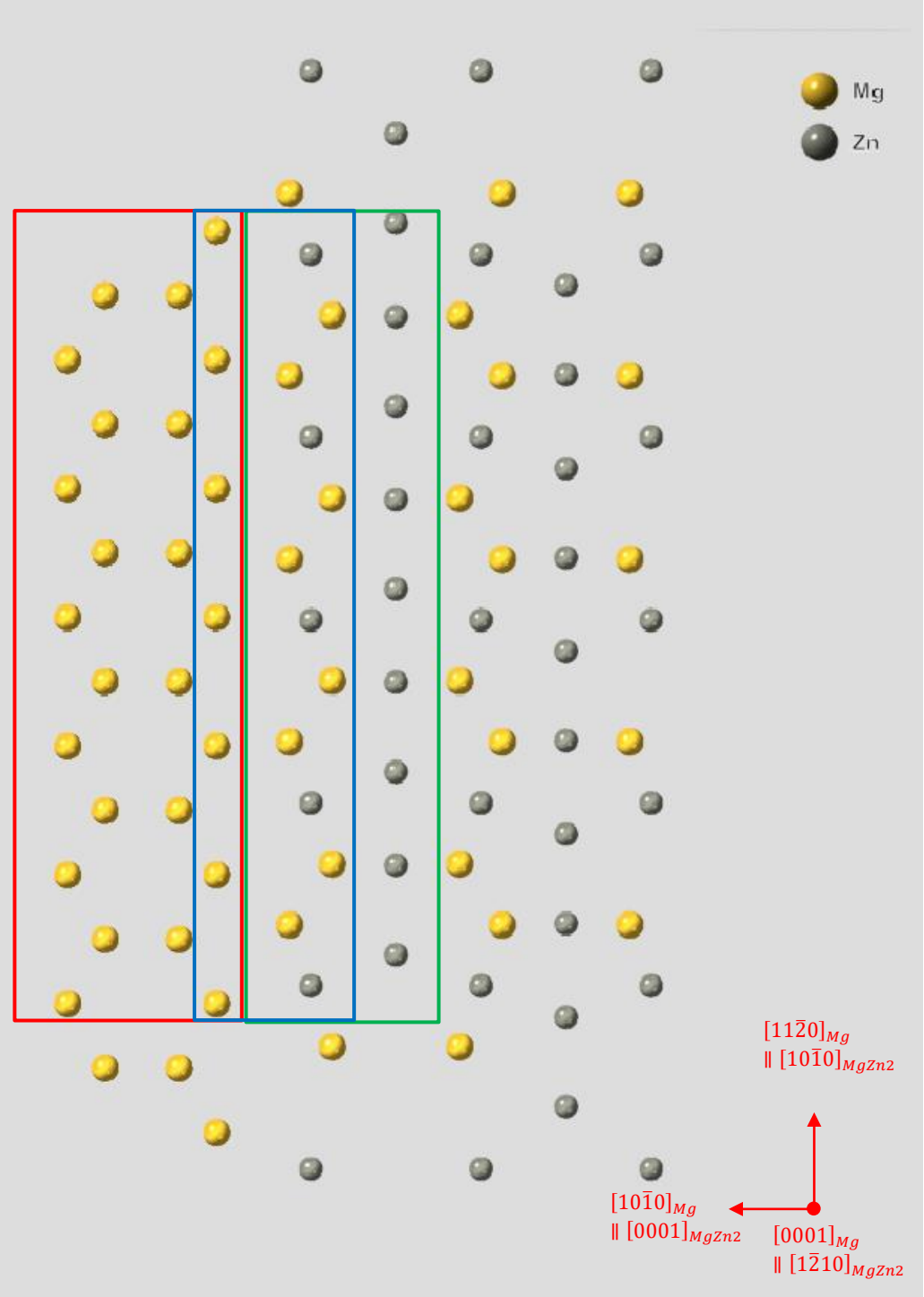


Figure 99 An illustration of the Mg-$MgZn_2$ interface constructed by Crystalmaker. Note the 2-D view of the crystal structure does not represent the actual chemical composition of the $MgZn_2$ precipitate as some atoms are covered by other atom layers

However, the exact crystal structure of $MgZn_2$ reveals that there are two Mg atoms near the $(0001)_{MgZn2}$ plane which are close enough to be on the interphase boundary. With these two Mg atoms, the atom spacing along $[10\bar{1}0]_{MgZn2}$ will then reduce to 3.03Å, resulting in a good registry between the two structures. In this case, as the magnitude of the Burgers vector in the Mg matrix will be similar to that in the $MgZn_2$, this will lead to a semi-coherent, or even a constrained coherent interphase boundary with only 5.3% mismatch with the Mg matrix. An illustration of the similarity of crystal structures and the Burgers vectors on the $[11\bar{2}0]_{Mg} \parallel [10\bar{1}0]_{MgZn2}$ direction is shown below in Figure 100.

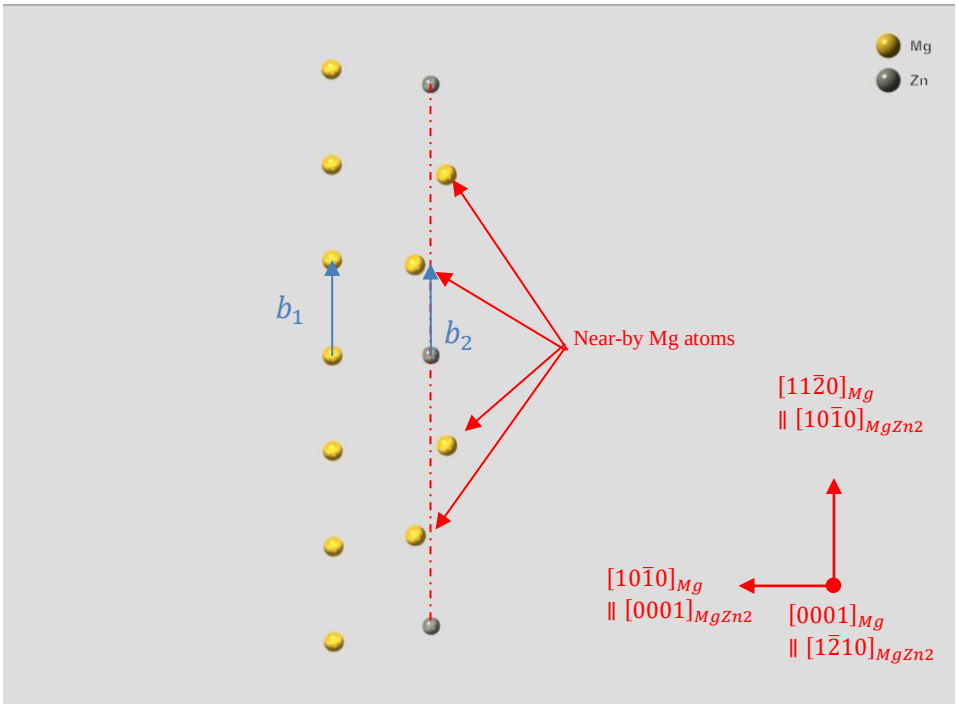


Figure 100 Schematic illustration showing the similarity of crystal structure between $[11\bar{2}0]_{Mg}$ and $[10\bar{1}0]_{MgZn2}$. With a suitable elastic strain, the interphase boundary could be semi-coherent or even coherent. The Burgers vectors in both phases are marked in the respective phase

In order to show the interface marked by the blue rectangle in Figure 99 (which is $(1\bar{1}00)_{Mg} - (0001)_{MgZn2}$) more clearly, another figure is constructed with its viewing

direction along $[1\bar{1}00]_{Mg} \parallel [0001]_{MgZn2}$, where the interface normal is exactly the page normal. The Mg atoms in the Mg matrix are coloured blue to enhance the contrast. With the Mg atoms near the $(0001)_{MgZn2}$ plane on the interface, ordered periodic near-coincident sites (marked with red circles) can be found throughout the interface, which indicates that the crystal structures of the two phases at the interface have high similarity.

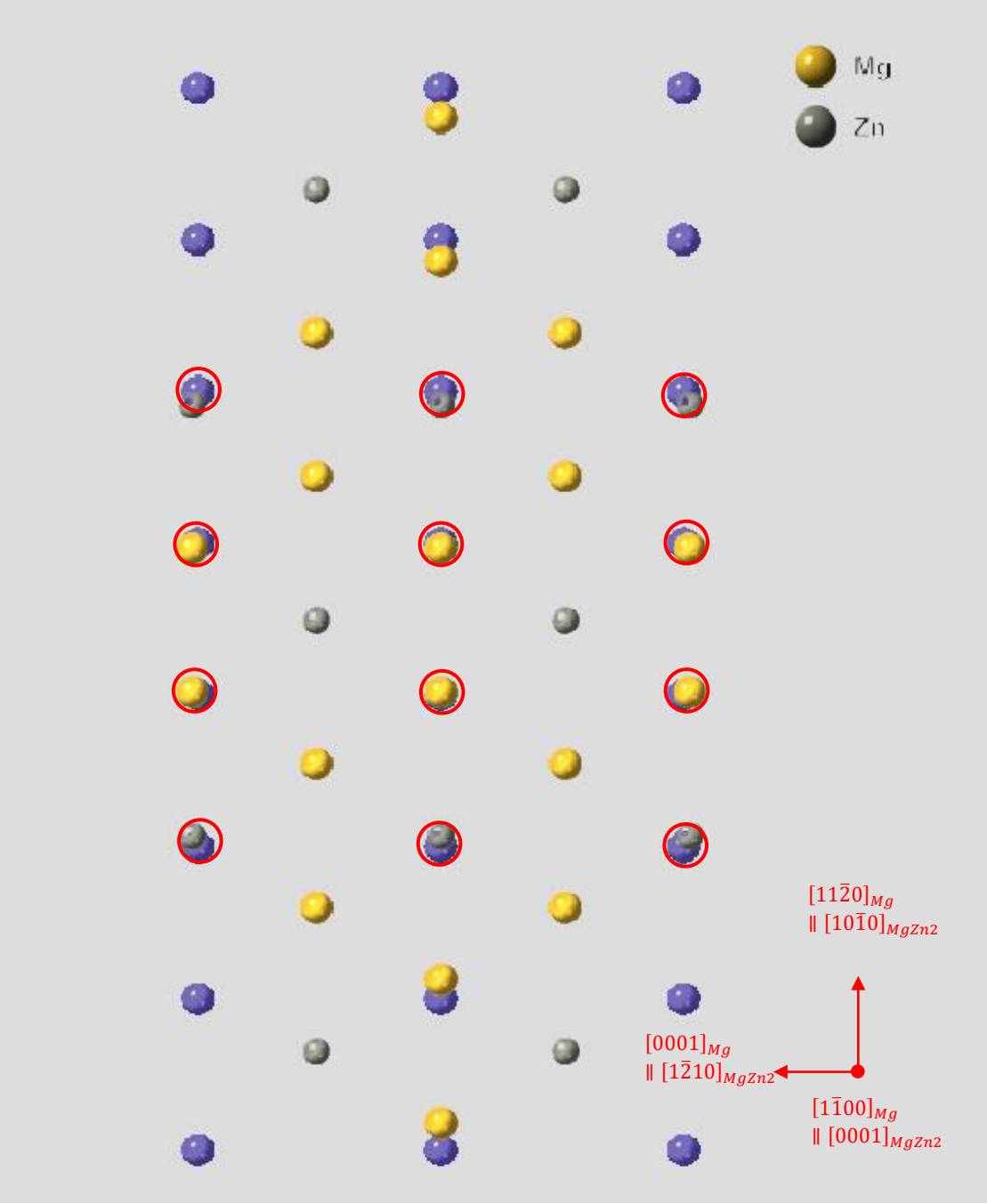


Figure 101 An illustration of the $(1\bar{1}00)_{Mg} - (0001)_{MgZn2}$ interface. The near-coincident sites are marked with red circles. The Mg atoms in the Mg matrix is coloured blue for better contrast.

In addition, it should be noted that $\frac{1}{3}\langle 11\bar{2}0\rangle_{Mg}$ (b_1 in Figure 100) is a perfect vector in Mg, but that the similar vector $\frac{1}{6}\langle 10\bar{1}0\rangle_{MgZn2}$ (b_2 in Figure 100) is not a perfect vector in

$MgZn_2$. The motion of a single Burgers vector in $MgZn_2$ will therefore create APB behind it, hence it might be expected that the dislocation travels in the $MgZn_2$ precipitate in groups of three so that crystal periodicity is maintained. A small residual dislocation will be left at the entry interface.

Therefore, with a semi-coherent or coherent interphase boundary, the Burgers vector of the basal a dislocations will remain nearly the same throughout the matrix and the $MgZn_2$ precipitate. On the other hand, with a similar shear modulus to that of $MgZn_2$ but a much higher mismatch across the interface, c-axis Mg_2Sn rods in the Mg-6Sn-3Al alloy were not sheared. This again supports that the coherency of the interphase boundary plays an important role in the transition from precipitate shearing to Orowan looping. Thus, basal dislocations will face less resistance travelling into the precipitate, which could be the reason for the $MgZn_2$ precipitates being sheared.

8.4 Explaining the work-hardening in the Mg-6Sn-3Zn alloy

It can be found for the Mg-6Sn-3Zn alloy that, even considering all the strengthening mechanisms, including solid solution strengthening, Orowan strengthening and precipitate shearing, the estimated strength is still lower than that actually measured: 29.92MPa. In addition, pillar compression tests have revealed an enormous work-hardening rate in the Mg-6Sn-3Zn alloy compared with Mg-6Sn and Mg-6Sn-3Al. A figure showing the work-hardening rate of all three Mg-Sn alloys is shown below in Figure 102.

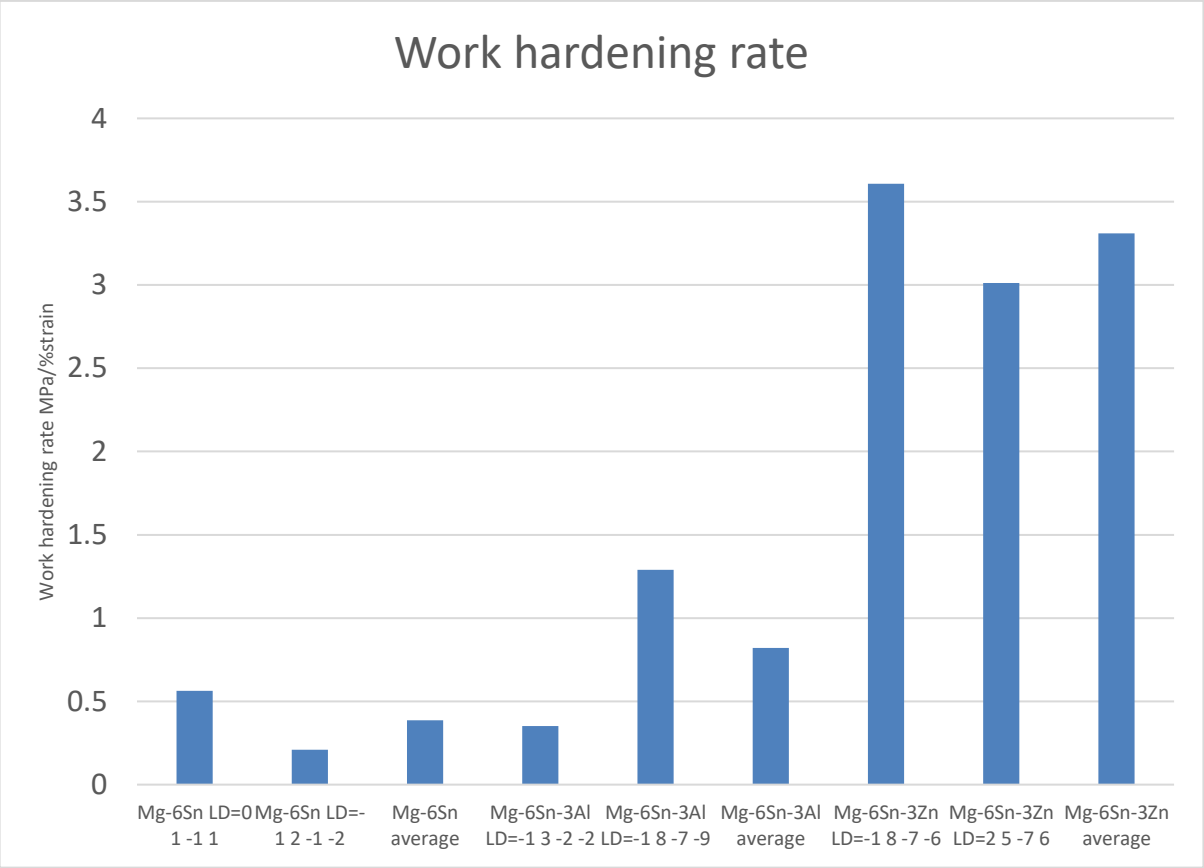


Figure 102 Work hardening rate of three Mg-Sn alloys

Work hardening is the increase in strength with strain of metal. It comes from blocking or cross slipping of dislocations, preventing further dislocation motion [91]. For a precipitate strengthened alloy, the work hardening will be related to its precipitates. Assuming precipitates do not exist in the alloy, dislocations will glide freely within the alloys in groups and eliminate on the sample surface, forming slip bands. With the existence of precipitates, the leading dislocations will be stopped at the precipitates, which serve as a barrier. Succeeding dislocations will then pile up behind the leading dislocations and result in work hardening [104].

It is inferred that the high work-hardening rate from the Mg-6Sn-3Zn alloy is contributed by both the Mg_2Sn and the $MgZn_2$ precipitates. For the Mg_2Sn precipitates, comparing the Mg-6Sn and Mg-6Sn-3Al alloys, as indicated by the figure, the presence of non-basal

precipitates (Type 5 and Type 6 in Mg-6Sn-3Al) has increased the work-hardening rate due to more basal a dislocations being blocked and piling up at the precipitate-matrix interface which therefore resists further dislocation motion and promotes buckling and cross slip. The non-basal Mg_2Sn laths (Type 7 prismatic laths) will exhibit the same behaviour as the non-basal precipitates in the Mg-6Sn-3Al alloy. This would contribute to the strengthening and work hardening.

The $MgZn_2$ precipitates which are sheared during the slip are believed to be another main contributor to work hardening in the Mg-6Sn-3Zn alloy, which is different from the situation in Mg-6Sn and Mg-6Sn-3Al. As suggested by Alizadeh and Llorca, basal a dislocations have to pile up at the $MgZn_2$ precipitate-matrix interface before they can shear through the precipitate[105]. First-principle simulations of the stacking fault energy indicates that a high stress is required to promote dislocation slip in these precipitates[106]. With multiple dislocations piling up prior to the dislocations penetrating the precipitates, stress is accumulated. This is also confirmed by Huang *et al.* for the shearable β_1 precipitates in Mg-RE alloys along with the simulation of Esteban-Manzanares *et al.* of the Mg-Al alloy system[107], [108]. The main reason for the enormous work hardening in the Mg-6Sn-3Zn alloy may lie in the finely distributed c-axis $MgZn_2$ narrow rods with a very high numeric ratio (taking over 78.60% of the entire precipitate population) and aspect ratio (~ 50:1). Therefore, fine and homogeneously distributed dislocation barriers will be present in the alloy. These barriers will then prevent further dislocation motion, cause buckling and cross slip and lead to a great contribution to work hardening.

Hence, the high strength and work hardening of the Mg-6Sn-3Zn alloys is provided by both the Orowan looping round the non-basal Mg_2Sn precipitates and the shearing of the $MgZn_2$ precipitates; the $MgZn_2$ precipitates are believed to be the main contributor.

8.5 Promoting non-basal precipitates in Mg-Sn alloys

Both existing research and the results presented in this work indicate that non-basal precipitates contribute greatly to the resistance to basal a slip in Mg-Sn alloys[5], [7], [58], [59], [80], [109]. Therefore, promoting non-basal precipitates would greatly enhance the performance of Mg-Sn alloys. Currently, most attempts at promoting non-basal precipitates are still based on "trial and error". Although some research has managed to design and then achieve non-basal precipitates in some Mg alloys from a crystallographic matching aspect, no success has been reported for the Mg_2Sn precipitates[110]. To design a proper non-basal precipitate strengthened Mg-Sn alloy, one must carefully consider both crystallographic and thermodynamic aspects, which is currently difficult to achieve. From the aspect of thermodynamics, interfacial energy, chemical free energy and elastic strain energy all contribute to the formation of precipitates[6], [48], [57], [58], [61]. However, these energies cannot be precisely quantified at the moment. Some crystallographic models have also been applied to the Mg-Sn alloys, but only to explain the reason for certain precipitate habit planes appearing, rather than predicting possible habit planes[60], [111]–[114]. For the Mg-Sn alloy system, predicting and designing precipitate habit planes is still difficult at the moment and would require intense research.

Despite the design and prediction of precipitate habit planes by crystallographic and thermodynamic analysis, there could be alternatives. For example, a novel twinning-ageing-detwinning (TAD) approach has been successfully applied to an AZ80 alloy, where the precipitation process takes place in $\{10\bar{1}2\}_{Mg}$ tension twins which are 86.3° away from the original orientation. [115]. The orientation of the precipitates will not change after detwinning, leading to an enormous number of non-basal precipitates. More recent research has applied this approach to the Mg-Sn alloy system, where a massive number of non-basal

precipitates were introduced into a Mg-5Sn (wt.%) alloy without using ternary elements[116]. This approach has provided an alternative to producing non-basal precipitate strengthened Mg-Sn alloys. Therefore, based on the existing research, it is hereby suggested that with the TAD approach, alloying elements such as Al and Zn that are designated to promote non-basal precipitates can now be replaced by elements which promote the number density of precipitates, e.g., Na, Ca and Ag, in order to produce Mg-Sn alloys strengthened by refined non-basal precipitates.

9 Conclusions and Future work

9.1 Conclusions

Three Mg-Sn alloys, Mg-6Sn, Mg-6Sn-3Al and Mg-6Sn-3Zn have been cast and aged to peak strength. The phases present in the alloys have been identified by both XRD and STEM-EDS. In the Mg-6Sn and Mg-6Sn-3Al alloys, the precipitates were identified as being Mg_2Sn, while in the Mg-6Sn-3Zn alloy the precipitates were identified as being Mg_2Sn and $MgZn_2$. In the different alloys, the precipitates exhibit different morphologies and crystallography. TEM analysis has confirmed 2 types of Mg_2Sn precipitates in the Mg-6Sn alloy, 4 types of Mg_2Sn precipitates in the Mg-6Sn-3Al alloy and 2 types of Mg_2Sn and 2 types of $MgZn_2$ precipitates in the Mg-6Sn-3Zn alloy.

The peak aged alloys have been fabricated into micro-pillars and compressed to a strain of 10% to analyse the effect of the different precipitate types on basal slip. The as-compressed pillars have been examined by TEM for post-mortem analysis to confirm the dislocations activated. For all three alloys, basal a slip is the only slip system activated. Dislocations loops were not observed in the samples, possibly due to the dislocation loops having collapsed into the interphase boundary between the precipitates and the matrix. Shearing of fine $MgZn_2$ narrow rods were also observed in the sample. The Mg-6Sn alloy containing only basal precipitates exhibits the lowest CRSS of 13.22MPa. The Mg-6Sn-3Al alloy exhibits a higher strength of 21.34MPa mainly due to the presence of pyramidal and c-axis precipitates. The Mg-6Sn-3Zn alloy exhibits the highest CRSS of 29.92MPa, not only due to prismatic and c-axis precipitates but also to shearing of the fine $MgZn_2$ narrow rods.

The three alloys were then analysed for their respective strengthening mechanisms for basal slip. Orowan strengthening is the most important strengthening mechanism for all three

alloys. As the microstructure of the Mg-Sn alloy system is usually dominated by a variety of precipitate types, the general form of the Orowan strengthening model does not estimate the cooperation between different precipitate types. A universally applicable model modifying the general Orowan strengthening equation has been proposed to estimate the contribution of Orowan strengthening by different precipitate types. In addition to the solid solution strengthening and the precipitate shearing strengthening, this model provides an adequate prediction of the Orowan strengthening effect contributed by multiple precipitate types.

9.2 Suggestions for future work

Based on the work presented and current research front, the following suggestions are made here for future work in this area:

As the precipitates in this study and some other existing studies ([48], [57], [58], [60], [109]) have all been examined by post-mortem TEM observations, in-situ TEM heating experiments could be useful to analyse the precipitation process and sequence of different precipitates. Existing studies have analysed the precipitation process of $Mg_{17}Al_{12}$ precipitates in AZ series alloys, as well as a series of other materials such as Ti, Ni and Al[117]–[120]. But this has not been applied to any of the Mg-Sn alloys.

Basal a dislocations in this study are also examined via post-mortem TEM observations. To analyse the exact interaction between dislocations and different precipitate types, in-situ TEM mechanical tests would be useful. In addition, the collapsing of dislocations to interphase boundaries is suspected and could be confirmed by in-situ observations.

The Mg-Sn alloy system is supposed to provide good mechanical properties even at elevated temperatures. Mechanical testing at different temperatures and creep tests could be performed to evaluate the exact performance of Mg-Sn alloys.

The proposed model of Orowan strengthening contributed by multiple precipitate types has only been evaluated for the alloys investigated in the present study. In order to confirm the validity of this model, evaluation of some other alloys or heat treatment conditions should be performed.

The early research by Henes and Gerold suggests that heat treatment parameters including double ageing have the potential to alter the morphologies of the Mg_2Sn precipitates [8]. However, most succeeding research focused on the effect of alloying elements on precipitate morphologies. From a thermodynamic and kinetics aspect, it would be of interest to evaluate the effect of different heat treatment parameters on the precipitation process.

The essence of the formation of different precipitate types is a result of the competition between chemical free energy, strain energy and interfacial energy. With modern simulation methods such as first-principles simulation and phase-field method, it would be of interest for researchers to figure out the reason for a certain precipitate type occurring under a specific condition.

10 References

[1] U.S. Energy Information Administration, “Petroleum & Other Liquids,” 2020. https://www.eia.gov/dnav/pet/hist/LeafHandler.ashx?n=PET&s=EMM_EPM0_PTE_NUS_DPG&f=W (accessed Mar. 23, 2017).

[2] M. K. Kulekci, “Magnesium and its alloys applications in automotive industry,” *Int. J. Adv. Manuf. Technol.*, vol. 39, no. 9, pp. 851–865, 2008, doi: 10.1007/s00170-007-1279-2.

[3] M. M. Avedesian and H. Baker, *ASM specialty handbook: magnesium and magnesium alloys*, vol. 274. ASM international Materials Park, OH, 1999.

[4] G. Nayyeri and R. Mahmudi, “Enhanced creep properties of a cast Mg-5Sn alloy subjected to aging-treatment,” *Mater. Sci. Eng. A*, vol. 527, no. 18–19, pp. 4613–4618, 2010, doi: 10.1016/j.msea.2010.04.015.

[5] C. L. Mendis, C. J. Bettles, M. A. Gibson, and C. R. Hutchinson, “An enhanced age hardening response in Mg-Sn based alloys containing Zn,” *Mater. Sci. Eng. A*, vol. 435–436, pp. 163–171, 2006, doi: 10.1016/j.msea.2006.07.090.

[6] X. Zhang, M. Wang, R. He, W. Li, and B. Y. Zong, “A phase field model to simulate competitive precipitation of Mg2Sn along the basal or pyramidal habit planes in Mg-2.2Sn-0.1Zn alloy,” *Comput. Mater. Sci.*, vol. 127, pp. 261–269, 2017, doi: 10.1016/j.commatsci.2016.10.019.

[7] F. R. Elsayed, T. T. Sasaki, C. L. Mendis, T. Ohkubo, and K. Hono, “Compositional optimization of Mg-Sn-Al alloys for higher age hardening response,” *Mater. Sci. Eng. A*, vol. 566, pp. 22–29, 2013, doi: 10.1016/j.msea.2012.12.041.

[8] S. Henes and V. Gerold, “Röntgenographische Untersuchungen der

Aussheidungsvorgänge in Magnesium-Blei- und Magnesium-Zinn-Legierungen," *Zeitschrift für Met.*, vol. 53, p. 743, 1962.

[9] E. F. Emley, *Principles of magnesium technology*,. Oxford; New York: Pergamon Press, 1966.

[10] R. S. Busk, "Magnesium and Its Alloys," in *Handbook of Materials Selection*, John Wiley & Sons, Inc., 2002, pp. 259–265. doi: 10.1002/9780470172551.ch8.

[11] M. O. Pekguleryuz, K. U. Kainer, A. Arslan Kaya, and A. A. Kaya, "2 – Physical metallurgy of magnesium," in *Fundamentals of Magnesium Alloy Metallurgy*, 2013, pp. 33–84. doi: 10.1533/9780857097293.33.

[12] M. Gupta and N. M. L. Sharon, "Introduction to Magnesium," in *Magnesium, Magnesium Alloys, and Magnesium Composites*, John Wiley & Sons, Inc., 2011, pp. 1–12. doi: 10.1002/9780470905098.ch1.

[13] R. Von Mises, "Mechanics of plastic deformation of crystals," *Appl. Math. Mech.*, vol. 592, p. 8, 1928.

[14] W. D. Callister and D. G. Rethwisch, *Materials science and engineering: an introduction*, vol. 7. Wiley New York, 2007.

[15] P. G. Partridge, "The crystallography and deformation modes of hexagonal close-packed metals," *Metall. Rev.*, vol. 12, no. 1, pp. 169–194, Jan. 1967, doi: 10.1179/mtlr.1967.12.1.169.

[16] F. Kang, Z. Li, J. T. Wang, P. Cheng, and H. Y. Wu, "The activation of c + a non-basal slip in Magnesium alloys," *J. Mater. Sci.*, vol. 47, no. 22, pp. 7854–7859, 2012, doi: 10.1007/s10853-012-6344-z.

[17] W. D. Robertson and R. E. Reed-Hill, "Additional modes of deformation twinning in magnesium," *Acta Metall.*, vol. 5, no. 12, pp. 717–727, 1957.

[18] A. Akhtar and E. Teghtsoonian, “Solid solution strengthening of magnesium single crystals-I alloying behaviour in basal slip,” *Acta Metall.*, vol. 17, no. 11, pp. 1339–1349, 1969, doi: 10.1016/0001-6160(69)90151-5.

[19] T. Obara, H. Yoshinga, and S. Morozumi, “{11$\bar{2}$2}〈1123〉 Slip system in magnesium,” *Acta Metall.*, vol. 21, no. 7, pp. 845–853, 1973, doi: 10.1016/0001-6160(73)90141-7.

[20] M. R. Barnett, “Twinning and the ductility of magnesium alloys: Part I: ‘Tension’ twins,” *Mater. Sci. Eng. A*, vol. 464, no. 1, pp. 1–7, 2007, doi: 10.1016/j.msea.2006.12.037.

[21] M. R. Barnett, “Twinning and the ductility of magnesium alloys: Part II. ‘Contraction’ twins,” *Mater. Sci. Eng. A*, vol. 464, no. 1, pp. 8–16, 2007, doi: 10.1016/j.msea.2007.02.109.

[22] S. You, Y. Huang, K. U. Kainer, and N. Hort, “Recent research and developments on wrought magnesium alloys,” *J. Magnes. Alloy.*, vol. 5, no. 3, pp. 239–253, 2017, doi: https://doi.org/10.1016/j.jma.2017.09.001.

[23] S. Celotto and T. J. Bastow, “Study of precipitation in aged binary Mg-Al and ternary Mg-Al-Zn alloys using 27Al NMR spectroscopy,” *Acta Mater.*, vol. 49, no. 1, pp. 41–51, 2001, doi: 10.1016/S1359-6454(00)00305-0.

[24] L. Wu, F. Pan, M. Yang, and R. Cheng, “An investigation of second phases in as-cast AZ31 magnesium alloys with different Sr contents,” *J. Mater. Sci.*, vol. 48, no. 16, pp. 5456–5469, 2013, doi: 10.1007/s10853-013-7339-0.

[25] K. N. Braszczyńska-Malik, “Discontinuous and continuous precipitation in magnesium-aluminium type alloys,” *J. Alloys Compd.*, vol. 477, no. 1–2, pp. 870–876, 2009, doi: 10.1016/j.jallcom.2008.11.008.

[26] S. Celotto, “TEM study of continuous precipitation in Mg-9 wt%Al-1 wt%Zn alloy,” *Acta Mater.*, vol. 48, no. 8, pp. 1775–1787, 2000, doi: 10.1016/S1359-6454(00)00004-5.

[27] A. Crawley and K. Milliken, “Precipitate morphology and orientation relationships in an aged Mg-9% Al-1% Zn-0.3% Mn alloy,” *Acta Metall.*, vol. 22, pp. 557–562, 1974.

[28] M. X. Zhang and P. M. Kelly, “Crystallography of Mg17Al12 precipitates in AZ91D alloy,” *Scr. Mater.*, vol. 48, no. 5, pp. 647–652, 2003, doi: 10.1016/S1359-6462(02)00555-9.

[29] J. Gjonnes and T. Ostmoe, “Precipitation and pre-precipitationin a Mg-Al alloy,” *Z Met.*, vol. 61, no. 8, pp. 604–606, 1970.

[30] D. Duly, “Application of the invariant line model for b.c.c./h.c.p. couples: A criterion based on surface variations,” *Acta Metall. Mater.*, vol. 41, no. 5, pp. 1559–1566, 1993, doi: 10.1016/0956-7151(93)90264-S.

[31] F. Findik, “Discontinuous (cellular) precipitation,” *J. Mater. Sci. Lett.*, vol. 17, no. 1, pp. 79–83, 1998, doi: 10.1023/A:1006510228181.

[32] C. R. Hutchinson, J. F. Nie, and S. Gorsse, “Modeling the precipitation processes and strengthening mechanisms in a Mg-Al-(Zn) AZ91 alloy,” *Metall. Mater. Trans. A*, vol. 36, no. 8, pp. 2093–2105, 2005, doi: 10.1007/s11661-005-0330-x.

[33] Y. H. Kang, X. X. Wang, N. Zhang, H. Yan, and R. S. Chen, “Effect of initial temper on the creep behavior of precipitation–hardened WE43 alloy,” *Mater. Sci. Eng. A*, vol. 689, no. December 2016, pp. 419–426, 2017, doi: 10.1016/j.msea.2017.02.081.

[34] C. C. Jain and C. H. Koo, “Creep and corrosion properties of the extruded magnesium alloy containing rare earth,” *Mater. Trans.*, vol. 48, no. 2, pp. 265–272, 2007, doi: 10.2320/matertrans.48.265.

[35] I. Anyanwu, S. Kamado, and Y. Kojima, “Creep properties of Mg-Gd-Y-Zr alloys,” *Mater. Trans.*, vol. 42, no. 7, p. 1212, 2001.

[36] J. Wang, L. Luo, Q. Huo, Y. Shi, Z. Xiao, Y. Ye, and X. Yang, “Creep behaviors of a highly concentrated Mg-18 wt% Gd binary alloy with and without artificial aging,” *J. Alloys Compd.*, vol. 774, pp. 1036–1045, 2019, doi: 10.1016/j.jallcom.2018.10.013.

[37] A. Srinivasan, K. K. Ajithkumar, J. Swaminathan, U. T. S. Pillai, and B. C. Pai, “Creep Behavior of AZ91 Magnesium Alloy,” *Procedia Eng.*, vol. 55, pp. 109–113, 2013, doi: 10.1016/j.proeng.2013.03.228.

[38] S. Fu and J. Wang, “Creep behaviour of T6 treated Mg-4Al-5.1Y-2.5LPC alloy,” *Chem. Eng. Trans.*, vol. 51, pp. 97–102, 2016, doi: 10.3303/CET1651017.

[39] S. Ong, W. Richards, A. Jain, G. Hautier, M. Kocher, S. Cholia, D. Gunter, V. Chevrier, K. Persson, and G. Ceder, “Python Materials Genomics (pymatgen): A robust, open-source python library for materials analysis,” *Comput. Mater. Sci.*, vol. 68, pp. 314–319, 2013, doi: https://doi.org/10.1016/j.commatsci.2012.10.028.

[40] P. Poddar, K. L. Sahoo, S. Mukherjee, and A. K. Ray, “Creep behaviour of Mg–8% Sn and Mg–8% Sn–3% Al–1% Si alloys,” *Mater. Sci. Eng. A*, vol. 545, pp. 103–110, 2012, doi: 10.1016/j.msea.2012.03.007.

[41] C. Cáceres, C. Davidson, J. Griffiths, and C. Newton, “Effects of solidification rate and ageing on the microstructure and mechanical properties of AZ91 alloy,” *Mater. Sci. Eng. A*, vol. 325, no. 1–2, pp. 344–355, 2002, doi: 10.1016/S0921-5093(01)01467-8.

[42] B. Q. Shi, R. S. Chen, and W. Ke, “Solid solution strengthening in polycrystals of Mg-Sn binary alloys,” *J. Alloys Compd.*, vol. 509, no. 7, pp. 3357–3362, 2011, doi: 10.1016/j.jallcom.2010.12.065.

[43] C. Cáceres and D. Rovera, “Solid solution strengthening in concentrated Mg–Al

alloys," *J. Light Met.*, vol. 1, no. 3, pp. 151–156, 2001, doi: 10.1016/S1471-5317(01)00008-6.

[44] E. Orowan, "Classification and nomenclature of internal stresses," *J. Inst. Met.*, vol. 73, no. 11, pp. 47–59, 1947.

[45] E. J. Mittemeijer, *Fundamentals of Materials Science: The Microstructure–Property Relationship Using Metals as Model Systems*. Springer Berlin Heidelberg, 2010. [Online]. Available: https://books.google.co.uk/books?id=i59NEBD-OvAC

[46] M. Gharghouri, G. C. Weatherly, J. D. Embury, and J. Root, "Study of the mechanical properties of Mg-7.7at.% Al by in-situ neutron diffraction," *Philos. Mag. A*, vol. 79, no. 7, pp. 1671–1695, 1999, doi: 10.1080/01418619908210386.

[47] A. S. M. International. and H. Committee., *ASM handbook. Volume 3, Volume 3,*. Materials Park, Ohio: ASM International, 1992.

[48] C. Q. Liu, H. W. Chen, H. Liu, X. J. Zhao, and J. F. Nie, "Metastable precipitate phases in Mg–9.8 wt%Sn alloy," *Acta Mater.*, vol. 144, pp. 590–600, 2018, doi: 10.1016/j.actamat.2017.10.023.

[49] T. T. Sasaki, K. Oh-ishi, T. Ohkubo, and K. Hono, "Enhanced age hardening response by the addition of Zn in Mg–Sn alloys," *Scr. Mater.*, vol. 55, no. 3, pp. 251–254, 2006, doi: 10.1016/j.scriptamat.2006.04.005.

[50] Y. Chen, L. Jin, W. Li, Y. Song, and L. Hao, "Microstructure and mechanical properties of as aged Mg–3Sn–1Al and Mg–3Sn–2Zn–1Al alloy," *Mater. Sci. Technol.*, vol. 31, no. 1, pp. 73–78, 2015, doi: 10.1179/1743284714Y.0000000607.

[51] F. R. Elsayed, T. T. Sasaki, C. L. Mendis, T. Ohkubo, and K. Hono, "Significant enhancement of the age-hardening response in Mg-10Sn-3Al-1Zn alloy by Na microalloying," *Scr. Mater.*, vol. 68, no. 10, pp. 797–800, 2013, doi:

10.1016/j.scriptamat.2013.01.032.

[52] M. Zhang, W. zheng Zhang, G. zhen Zhu, and K. Yu, “Crystallography of Mg2Sn precipitates in Mg-Sn-Mn-Si alloy,” *Trans. Nonferrous Met. Soc. China (English Ed.*, vol. 17, no. 6, pp. 1428–1432, 2007, doi: 10.1016/S1003-6326(07)60289-1.

[53] W. Li, X. Huang, and W. Huang, “Effects of Ca, Ag addition on the microstructure and age-hardening behavior of a Mg-7Sn (wt%) alloy,” *Mater. Sci. Eng. A*, vol. 692, pp. 75–80, 2017, doi: 10.1016/j.msea.2017.03.066.

[54] C. L. Mendis, C. J. Bettles, M. A. Gibson, S. Gorsse, and C. R. Hutchinson, “Refinement of precipitate distributions in an age-hardenable Mg-Sn alloy through microalloying,” *Philos. Mag. Lett.*, vol. 86, no. 7, pp. 443–456, 2006, doi: 10.1080/09500830600871186.

[55] X.-F. Huang and W.-Z. Zhang, “Improved age-hardening behavior of Mg–Sn–Mn alloy by addition of Ag and Zn,” *Mater. Sci. Eng. A*, vol. 552, pp. 211–221, 2012, doi: 10.1016/j.msea.2012.05.033.

[56] J. van der Planken, “Precipitation Hardening in Magnesium- Tin Alloys,” *J. Mater. Sci. Lett.*, vol. 4, pp. 927–929, 1969.

[57] C. Liu, H. Chen, and J.-F. Nie, “Interphase boundary segregation of Zn in Mg-Sn-Zn alloys,” *Scr. Mater.*, vol. 123, pp. 5–8, Oct. 2016, doi: 10.1016/j.scriptamat.2016.05.035.

[58] T. T. Sasaki, F. R. Elsayed, T. Nakata, T. Ohkubo, S. Kamado, and K. Hono, “Strong and ductile heat-treatable Mg-Sn-Zn-Al wrought alloys,” *Acta Mater.*, vol. 99, pp. 176–186, 2015, doi: 10.1016/j.actamat.2015.06.060.

[59] T. T. Sasaki, J. D. Ju, K. Hono, and K. S. Shin, “Heat-treatable Mg-Sn-Zn wrought alloy,” *Scr. Mater.*, vol. 61, no. 1, pp. 80–83, 2009, doi:

10.1016/j.scriptamat.2009.03.014.

[60] Z. Z. Shi and W. Z. Zhang, “Newly observed prismatic Mg2Sn laths in a Mg-Sn-Zn-Mn alloy,” *J. Mater. Sci.*, vol. 48, no. 21, pp. 7551–7556, 2013, doi: 10.1007/s10853-013-7570-8.

[61] H. Liu, Y. Gao, J. Z. Liu, Y. M. Zhu, Y. Wang, and J. F. Nie, “A simulation study of the shape of β precipitates in Mg-Y and Mg-Gd alloys,” *Acta Mater.*, vol. 61, no. 2, pp. 453–466, Jan. 2013, doi: 10.1016/j.actamat.2012.09.044.

[62] M. X. Zhang and P. M. Kelly, “Edge-to-edge matching model for predicting orientation relationships and habit planes - The improvements,” *Scr. Mater.*, vol. 52, no. 10, pp. 963–968, 2005, doi: 10.1016/j.scriptamat.2005.01.040.

[63] P. M. Kelly and M.-X. Zhang, “Edge-to-edge matching—The fundamentals,” *Metall. Mater. Trans. A*, vol. 37, no. 13, pp. 833–839, 2007, doi: 10.1007/bf02719727.

[64] W. Z. Zhang and G. C. Weatherly, “On the crystallography of precipitation,” *Prog. Mater. Sci.*, vol. 50, no. 2, pp. 181–292, 2005, doi: 10.1016/j.pmatsci.2004.04.002.

[65] Z. Z. Shi, F. Z. Dai, M. Zhang, X. F. Gu, and W. Z. Zhang, “Secondary coincidence site lattice model for truncated triangular β-Mg2Sn precipitates in a Mg-Sn-Based alloy,” *Metall. Mater. Trans. A Phys. Metall. Mater. Sci.*, vol. 44, no. 6, pp. 2478–2486, 2013, doi: 10.1007/s11661-013-1633-y.

[66] J. F. Nie, “Effects of precipitate shape and orientation on dispersion strengthening in magnesium alloys,” *Scr. Mater.*, vol. 48, no. 8, pp. 1009–1015, 2003, doi: 10.1016/S1359-6462(02)00497-9.

[67] Y. J. Wan, Y. Zeng, Y. C. Dou, D. C. Hu, X. Y. Qian, Q. Zeng, K. X. Sun, G. F. Quan, and I. Press, “Improved mechanical properties and strengthening mechanism with the altered precipitate orientation in magnesium alloys,” *J. Magnes. Alloy.*, 2021, doi:

10.1016/j.jma.2020.09.028.

[68] Z. Zhang and D. L. Chen, “Contribution of Orowan strengthening effect in particulate-reinforced metal matrix nanocomposites,” *Mater. Sci. Eng. A*, vol. 483–484, no. 1-2 C, pp. 148–152, 2008, doi: 10.1016/j.msea.2006.10.184.

[69] S. Si, “Micromechanical study of the role of precipitates on the plastic deformation of AZ91 magnesium alloy,” University of Birmingham, 2019.

[70] P. Y. Wang, J. G. Wang, C. Wang, J. S. Li, Z. M. Hua, H. Ju, M. X. Li, M. Zha, and H. Y. Wang, “Designing a new Mg-Zn-Ca-Y wrought alloy with high strength and ductility synergy,” *Materialia*, vol. 16, no. March, p. 101073, 2021, doi: 10.1016/j.mtla.2021.101073.

[71] R. Alizadeh, J. Wang, and J. LLorca, “Precipitate strengthening of pyramidal slip in Mg–Zn alloys,” *Mater. Sci. Eng. A*, vol. 804, no. January, p. 140697, 2021, doi: 10.1016/j.msea.2020.140697.

[72] J. Jain, P. Cizek, W. J. Poole, and M. R. Barnett, “Precipitate characteristics and their effect on the prismatic-slip- dominated deformation behaviour of an Mg-6 Zn alloy,” *Acta Mater.*, 2013, doi: 10.1016/j.actamat.2013.03.033.

[73] A. Roine, “Outokumpu HSC chemistry for windows,” *Chem. React. Equilib. Softw. with Extensive Ther-Mochemical Database*, 1994.

[74] B. C. Zhou, S. L. Shang, Y. Wang, and Z. K. Liu, “Data set for diffusion coefficients of alloying elements in dilute Mg alloys from first-principles,” *Data Br.*, vol. 5, pp. 900–912, 2015, doi: 10.1016/j.dib.2015.10.024.

[75] K. A. Persson, B. Waldwick, P. Lazic, and G. Ceder, “Prediction of solid-aqueous equilibria: Scheme to combine first-principles calculations of solids with experimental aqueous states,” *Phys. Rev. B*, vol. 85, no. 23, p. 235438, Jun. 2012, doi:

10.1103/PhysRevB.85.235438.

[76] A. Jain, G. Hautier, S. P. Ong, C. J. Moore, C. C. Fischer, K. A. Persson, and G. Ceder, "Formation enthalpies by mixing GGA and GGA $+$ U calculations," *Phys. Rev. B*, vol. 84, no. 4, p. 45115, Jul. 2011, doi: 10.1103/PhysRevB.84.045115.

[77] S. P. Ong, L. Wang, B. Kang, and G. Ceder, "Li−Fe−P−O2 Phase Diagram from First Principles Calculations," *Chem. Mater.*, vol. 20, no. 5, pp. 1798–1807, Mar. 2008, doi: 10.1021/cm702327g.

[78] T. T. Sasaki, K. Oh-ishi, T. Ohkubo, and K. Hono, "Effect of double aging and microalloying on the age hardening behavior of a Mg-Sn-Zn alloy," *Mater. Sci. Eng. A*, vol. 530, no. 1, pp. 1–8, 2011, doi: 10.1016/j.msea.2010.05.010.

[79] S. Henes and V. Gerold, "Rontgenographische Untersuchungen der Ausscheidungvorgange in Magnesium-Blei- und Magnesium-Zinn-Legierungen," *Zeitschrift für Met.*, vol. 53, p. 703, 1962.

[80] H. Pan, G. Qin, M. Xu, H. Fu, Y. Ren, F. Pan, Z. Gao, C. Zhao, Q. Yang, J. She, and B. Song, "Enhancing mechanical properties of Mg-Sn alloys by combining addition of Ca and Zn," *Mater. Des.*, vol. 83, pp. 736–744, 2015, doi: 10.1016/j.matdes.2015.06.032.

[81] E. Schmid, W. Boas, and F. I. G. Rawlins, "Kristallplastizität," *J. Phys. Chem.*, vol. 39, no. 9, p. 1248, Sep. 1935, doi: 10.1021/j150369a013.

[82] A. Vaid, J. Guénolé, A. Prakash, S. Korte-Kerzel, and E. Bitzek, "Atomistic simulations of basal dislocations in Mg interacting with Mg17Al12 precipitates," *Materialia*, vol. 7, no. May, p. 100355, 2019, doi: 10.1016/j.mtla.2019.100355.

[83] Y. Luo, L. Ran, X. Pang, and F. Pan, "Effects of Zn / Al mass ratio on microstructure evolution and mechanical properties of Mg – Sn based alloys," *Mater. Sci. Eng. A*, vol. 815, no. January, p. 141307, 2021, doi: 10.1016/j.msea.2021.141307.

[84] E. E. Underwood, “Quantitative Stereology for Microstructural Analysis,” *Microstruct. Anal.*, vol. V, pp. 35–66, 1973, doi: 10.1007/978-1-4615-8693-7_3.

[85] A. Hjorth Larsen *et al.*, “The atomic simulation environment—a Python library for working with atoms,” *J. Phys. Condens. Matter*, vol. 29, no. 27, p. 273002, 2017, doi: 10.1088/1361-648x/aa680e.

[86] Z. T. Li, X. G. Qiao, C. Xu, X. Q. Liu, S. Kamado, and M. Y. Zheng, “Enhanced strength by precipitate modification in wrought Mg–Al–Ca alloy with trace Mn addition,” *J. Alloys Compd.*, vol. 836, pp. 1–9, 2020, doi: 10.1016/j.jallcom.2020.154689.

[87] Z. Yu, X. Xu, A. Mansoor, B. Du, K. Shi, K. Liu, S. Li, and W. Du, “Precipitate characteristics and their effects on the mechanical properties of as-extruded Mg-Gd-Li-Y-Zn alloy,” *J. Mater. Sci. Technol.*, vol. 88, pp. 21–35, 2021, doi: 10.1016/j.jmst.2021.01.070.

[88] R. Alizadeh, J. Wang, and J. Llorca, “Precipitate strengthening of pyramidal slip in Mg–Zn alloys,” *Mater. Sci. Eng. A*, vol. 804, no. January, p. 140697, 2021, doi: 10.1016/j.msea.2020.140697.

[89] A. Akhtar and E. Teghtsoonian, “Substitutional solution hardening of magnesium single crystals,” *Philos. Mag.*, vol. 25, no. 4, pp. 897–916, 1972, doi: 10.1080/14786437208229311.

[90] A. Tehranchi, B. Yin, and W. A. Curtin, “Solute strengthening of basal slip in Mg alloys,” *Acta Mater.*, vol. 151, pp. 56–66, 2018, doi: 10.1016/j.actamat.2018.02.056.

[91] L. M. Brown, “Strengthening Mechanisms in Crystal Plasticity, by Ali Argon,” *Contemp. Phys.*, vol. 54, no. 6, pp. 306–307, Nov. 2013, doi: 10.1080/00107514.2013.857723.

[92] B. Reppich, “Particle strengthening,” *Mater. Sci. Technol.*, vol. 6, pp. 311–357, 1993.

[93] V. Gerold, “Precipitation hardening,” *Dislocations in solids*, no. 4, 1979.

[94] A. . Ardell, “Precipitation hardening,” *Metall. Mater. Trans. A*, vol. 16, pp. 2131–2165, 1985, doi: 10.1016/j.scriptamat.2020.03.034.

[95] Y. Guo, B. Liu, W. Xie, Q. Luo, and Q. Li, “Anti-phase boundary energy of β series precipitates in Mg-Y-Nd system,” *Scr. Mater.*, vol. 193, pp. 127–131, 2021, doi: 10.1016/j.scriptamat.2020.11.004.

[96] J. J. Bhattacharyya, F. Wang, N. Stanford, and S. R. Agnew, “Slip mode dependency of dislocation shearing and looping of precipitates in Mg alloy WE43,” *Acta Mater.*, vol. 146, pp. 55–62, 2018, doi: 10.1016/j.actamat.2017.12.043.

[97] Chris Schuh, “3.40J Physical Metallurgy.” Massachusetts Institute of Technology: MIT OpenCourseWare, 2009.

[98] H. Conrad and W. D. Robertson, “Effect of temperature on the flow stress and strain-hardening coefficient of magnesium single crystals,” *JOM*, vol. 9, no. 4, pp. 503–512, 1957, doi: 10.1007/BF03397908.

[99] C. P. Blankenship, E. Hornbogen, and E. A. Starke, “Predicting slip behavior in alloys containing shearable and strong particles,” *Mater. Sci. Eng. A*, vol. 169, no. 1–2, pp. 33–41, 1993, doi: 10.1016/0921-5093(93)90596-7.

[100] M. Liao, B. Li, and M. F. Horstemeyer, “Interaction between prismatic slip and a Mg17Al12 precipitate in magnesium,” *Comput. Mater. Sci.*, vol. 79, pp. 534–539, 2013, doi: 10.1016/j.commatsci.2013.07.016.

[101] C. M. Cepeda-Jiménez, M. Castillo-Rodríguez, and M. T. Pérez-Prado, “Origin of the low precipitation hardening in magnesium alloys,” *Acta Mater.*, vol. 165, pp. 164–176, 2019, doi: 10.1016/j.actamat.2018.11.044.

[102] E. L. S. Solomon and E. A. Marquis, “Deformation behavior of β′ and β‴ precipitates in Mg-RE alloys,” *Mater. Lett.*, vol. 216, pp. 67–69, 2018, doi: 10.1016/j.matlet.2017.12.149.

[103] J. Wang and N. Stanford, “Investigation of precipitate hardening of slip and twinning in Mg5%Zn by micropillar compression,” *Acta Mater.*, 2015, doi: 10.1016/j.actamat.2015.08.012.

[104] D. Hull and D. J. Bacon, “Chapter 9 - Dislocation Arrays and Crystal Boundaries,” D. Hull and D. J. B. T.-I. to D. (Fifth E. Bacon, Eds. Oxford: Butterworth-Heinemann, 2011, pp. 171–204. doi: https://doi.org/10.1016/B978-0-08-096672-4.00009-8.

[105] R. Alizadeh and J. Llorca, “Interactions between basal dislocations and β1′ precipitates in Mg–4Zn alloy: Mechanisms and strengthening,” *Acta Mater.*, vol. 186, pp. 475–486, 2020, doi: 10.1016/j.actamat.2020.01.028.

[106] W. Xiao, X. Zhang, W. T. Geng, and G. Lu, “Atomistic study of plastic deformation in Mg-Al alloys,” *Mater. Sci. Eng. A*, vol. 586, pp. 245–252, 2013, doi: 10.1016/j.msea.2013.07.093.

[107] Z. Huang, C. Yang, L. Qi, J. E. Allison, and A. Misra, “Dislocation pile-ups at β1 precipitate interfaces in Mg-rare earth (RE) alloys,” *Mater. Sci. Eng. A*, vol. 742, no. September 2018, pp. 278–286, 2019, doi: 10.1016/j.msea.2018.10.104.

[108] G. Esteban-Manzanares, A. Ma, I. Papadimitriou, E. Martínez, and J. Llorca, “Basal dislocation/precipitate interactions in Mg-Al alloys: an atomistic investigation,” *Model. Simul. Mater. Sci. Eng.*, vol. 27, no. 7, 2019, doi: 10.1088/1361-651X/ab2de0.

[109] S. Harosh, L. Miller, G. Levi, and M. Bamberger, “Microstructure and properties of Mg-5.6%Sn-4.4%Zn-2.1%Al alloy,” *J. Mater. Sci.*, vol. 42, no. 24, pp. 9983–9989, 2007, doi: 10.1007/s10853-007-2059-y.

[110] Z. Z. Shi, “Control on microstructure of Mg-Sn-based alloys and research on the precipitate crystallography in several Mg alloys,” Tsinghua University, 2011.

[111] X. Huang, H. Li, W. Cai, and W. Huang, “On the crystallographic features of Mn precipitates in a Mg-Sn-Mn alloy,” *J. Alloys Compd.*, vol. 633, pp. 54–58, 2015, doi: 10.1016/j.jallcom.2015.02.026.

[112] X. Huang and W. Huang, “Irrational crystallography of the ⟨1 1 2¯ 0⟩ Mg Mg 2 Sn precipitates in an aged Mg-Sn-Mn alloy,” *Mater. Charact.*, vol. 151, no. March, pp. 260–266, 2019, doi: 10.1016/j.matchar.2019.03.017.

[113] M. Zhang, W. Zhang, and F. Ye, “Interpretation of Precipitation Crystallography of Mg17A12l in a Mg-Al alloy in terms of Singular Interfacial Structure,” *Metall. Mater. Trans. A*, vol. 36, no. July, pp. 20–22, 2005.

[114] Z. Z. Shi, “The crystallography of lath-shaped Mg2Sn precipitates in a Mg-Sn-Zn-Mn alloy,” *J. Alloys Compd.*, vol. 559, pp. 158–161, 2013, doi: 10.1016/j.jallcom.2013.01.109.

[115] F. Liu, R. Xin, C. Wang, B. Song, and Q. Liu, “Regulating precipitate orientation in Mg-Al alloys by coupling twinning, aging and detwinning processes,” *Scr. Mater.*, vol. 158, pp. 131–135, 2019, doi: 10.1016/j.scriptamat.2018.08.049.

[116] Y. J. Wan, Y. Zeng, Q. Zeng, B. Song, X. F. Huang, X. Y. Qian, and B. Jiang, “Simultaneously improved strength and toughness of a Mg–Sn alloy through abundant prismatic lath-shaped precipitates,” *Mater. Sci. Eng. A*, vol. 811, no. 111, p. 141087, 2021, doi: 10.1016/j.msea.2021.141087.

[117] Q. Yu, J. Kacher, C. Gammer, R. Traylor, A. Samanta, Z. Yang, and A. M. Minor, “In situ TEM observation of FCC Ti formation at elevated temperatures,” *Scr. Mater.*, vol. 140, pp. 9–12, 2017, doi: 10.1016/j.scriptamat.2017.06.033.

[118] S. Y. Liu, Q. P. Cao, X. Mu, D. Wang, X. D. Wang, Y. Tang, D. X. Zhang, C. Kübel, and J. Z. Jiang, “In-situ TEM study of oxygen-modulated crystallization pathway in Ni-Zr metallic glass,” *J. Alloys Compd.*, vol. 800, pp. 254–260, 2019, doi: 10.1016/j.jallcom.2019.06.020.

[119] Y. Liu, D. Zhao, X. Nie, H. Tao, J. Wang, and J. Gui, “In situ transmission electron microscopy observations of precipitation and a new orientation relationship between γ-Mg 17Al 12 and magnesium-based matrix in an Mg-Al-Zn-Sn alloy,” *Philos. Mag. Lett.*, vol. 92, no. 12, pp. 668–674, 2012, doi: 10.1080/09500839.2012.715247.

[120] N. Bayat, T. Carlberg, and M. Cieslar, “In-situ study of phase transformations during homogenization of 6060 and 6063 Al alloys,” *J. Phys. Chem. Solids*, vol. 130, no. July 2018, pp. 165–171, 2019, doi: 10.1016/j.jpcs.2018.11.013.